Efficient, stable perovskite solar cells enabled by electrode interface engineering and nanoscale phase stabilization

Erin M. Sanehira

A dissertation

submitted in partial fulfillment of the

requirements for the degree of

Doctor of Philosophy

University of Washington

2017

Reading Committee:

Lih Y. Lin, Chair

Joseph M. Luther

Christine K. Luscombe

Program Authorized to Offer Degree:

Electrical Engineering

University of Washington

Abstract

Efficient, stable perovskite solar cells enabled by electrode interface engineering and nanoscale phase stabilization

Erin M. Sanehira

Chair of the Supervisory Committee:
Professor Lih Y. Lin
Electrical Engineering

Semiconducting metal halide perovskites have emerged as a promising solution-processable, photovoltaic material with research cell power conversion efficiencies now exceeding 22% under simulated sunlight. The prototypical composition of this "ABX_3" semiconductor is $CH_3NH_3PbI_3$, in which organic methylammonium cations charge stabilize lead iodide octahedra. Research is underway on mixed component systems with A-site cation combinations of methylammonium, formamidinium, cesium, and rubidium; B-site cations of Pb^{2+} and Sn^{2+}; and iodide, bromide and chloride anions. Although perovskite solar cells with low-cost fabrication methods have demonstrated impressive power conversion efficiencies, device durability remains a key concern of the technology. In this dissertation, the effect of the anode electrode material on the device lifetime is characterized under constant operating conditions. It is demonstrated that MoO_x/Al

electrodes are more stable than commonly used Au or Ag electrodes. Interestingly, the enhanced stability of MoO_x/Al electrodes is due to the formation of an oxide at the MoO_x/Al interface, which likely prevents ion migration between the device layers, as opposed to encapsulation from environmental agents. I also demonstrate a more stable photoactive layer comprised of $CsPbI_3$ quantum dots (QDs). $CsPbI_3$ is the lowest bandgap, all-inorganic lead halide perovskite, and has shown remarkable chemical and thermal stability up to 400 °C. However, bulk and thin film $CsPbI_3$ transitions to the undesired orthorhombic phase when cooled to room temperature. $CsPbI_3$ QDs have unique surface properties which alter the phase transitions and successfully maintain the photoactive cubic phase at room temperature and even well below. In addition to reporting the first demonstration of an all-inorganic $CsPbX_3$ nanocrystal solar cell, I also detail new QD surface treatments that improve the short circuit current density of the devices by doubling the QD film mobility. These advancements led to an NREL-certified QD solar cell efficiency of 13.43% that is currently the record efficiency reported for a QD solar cell of any material system. In this dissertation, I assess operational stability of thin film organic-inorganic perovskite solar cells, fabricate more durable electrodes, develop novel $CsPbI_3$ QD photovoltaic devices and discover new surface modifications to improve charge transport in efficient perovskite QD solar cells.

TABLE OF CONTENTS

LIST OF FIGURES

LIST OF TABLES

ACKNOWLEDGEMENTS

There are countless people who have been integral to my Ph.D. journey – a journey that started six years ago at the University of Washington. From day one, Professor Lih Lin has supported, encouraged and mentored me. Professor Lin, thank you for your guidance, especially in providing me with the freedom and encouragement to pursue various fellowships and research opportunities and aiding me through funding challenges. I am so grateful for your support, especially when my decisions added greater stress, complexity and tedious paperwork to our lives. I would also like to thank the Photonics Group members who I have had the pleasure of working with over the years – thank you Albus (Jingda) Wu, Peifeng Jing, Ethan Keeler, Chen Zou, Chang-Ching Tu, Matthew Strathman, Cameron Simmons, Yu Jin, Yunbo Liu and Conner Ballew for making my time in the Photonics Group an enjoyable one. I would also like to thank Professor Christine Luscombe for co-advising me and welcoming me into her laboratory. Thanks to her mentorship and the patience and guidance of her group members, I learned the fundamentals of solution-processed organic photovoltaics and had a second home at the University of Washington. I'm also extremely appreciative of Professor Arka Majumdar and Professor Qiuming Yu for serving on my Ph.D. supervisory committee and for showing genuine interest and curiosity in my research.

None of the research in this dissertation would have been possible without Dr. Joseph Luther and the help of many scientists, post-docs and graduate students at the National Renewable Energy Laboratory. Joey, thank you for first allowing me into your lab that first summer in 2014, and then allowing me to extend my "summer visit" from three months to three years. Over the past three years, I have learned so much from your mentorship, ranging from how to make perovskite solar

cells to how to be better and more productive researcher. I cannot thank you enough for first this opportunity and for your guidance and support along the way. I'd like to thank Ashley Marshall for her patience, support and friendship; whether I needed someone to teach me how to use the evaporator, some help interpreting technical data, or someone to discuss my latest podcast obsession with, I could always count on Ashley. I thank Jeff Christians for answering so many of my perovskite and research related questions, and for giving me confidence in my results at times when I might have otherwise been a little too critical. I thank Abhishek Swarnkar for bringing such energy to the laboratory and for his fantastic work that led to our *Science* paper! I thank Joe Berry for his technical insight, for sharing his professional advice and personal experience and for helping me land an exciting career opportunity. I'd also like to thank Benjia (Dak) Dou, Philip Schulz, Lance Wheeler, Nick Anderson, Greg Pach, Ryan Crisp, Boris Chernomordik, Dave Moore, Bertrand Tremolet de Villers, Matt Reese, Sue Ferrere, Kai Zhu and Matt Beard for their help in making this research possible and for making my time at NREL enjoyable.

Finally, I would like to thank all of my friends and family for their support throughout this Ph.D. journey. A special thanks goes to my parents for their love and for raising me to believe that I am capable of anything I set my mind to. I thank my grandparents for being my number one fans. And I thank my partner, Ben, for his patience and generosity – for the personal sacrifices he has made to allow me to follow my dreams, for tolerating my grumpiness during stressful times, and for filling my life with joy and wonderful memories.

DEDICATION

For my grandmother, Jean Sanehira,

my parents, Rene and Gary Sanehira,

& my partner, Benjamin Hopkins

And in loving memory of

my grandfather, Roy Segami,

my grandfather, Kazumi Sanehira,

& my grandmother, Tsugie Segami,

Chapter 1. AN INTRODUCTION TO PEROVSKITE AND QUANTUM DOT SOLAR CELLS

1.1 MOTIVATION

The effects of climate change have become ever more apparent; global land and ocean surface temperatures are rising, oceans are acidifying, and ice sheets and glaciers are melting at alarming rates [1]. According to the Intergovernmental Panel on Climate Change, the unprecedented[1] levels of carbon dioxide, methane and nitrous oxide, along with the effects of other anthropogenic drivers, are "*extremely likely*[2] to have been the dominant cause of the observed warming since the mid-20th century." Mitigation of climate change requires a transition away from conventional fossil fuel based energy sources, which produce majority of anthropogenic greenhouse gas emissions. Renewable, greenhouse gas emissions free alternative energy sources have been gaining traction in recent years and account for approximately 62% of the added global electricity generating capacity in 2016. However, the overall electricity generation from non-hydro renewable energy sources is only 7.9% of global electricity generation [2].

Solar energy is currently the most abundant alternative to conventional fossil fuels for electricity generation. The vast majority of commercially-available solar panels today are based on silicon wafer technology, which leverages the manufacturing expertise and infrastructure developed by the microelectronics industry. Research into next-generation photovoltaic (PV) technologies must combine approaches to both increase efficiency and reduce cost. Thin film alternatives such as CdTe and Cu(In,Ga)Se_2 (CIGS) have made significant strides toward cost

[1] Current atmospheric concentrations of carbon dioxide, methane and nitrous oxide are unprecedented in at least the last 800,000 years [1].
[2] This corresponds to a 95-100% likelihood based on the synthesis of evidence and agreement.

reduction, but still represent a small fraction of the PV market. In an effort to reduce costs further, researchers have sought to develop lightweight, solution-processable PVs, which could benefit from reducing costs of raw materials, manufacturing, transport and installation. Additionally, solution-based processing enables high throughput deposition methods such as roll-to-roll printing to keep up with the rising demand for emissions-free electricity. Historically, solution-processable solar cells have suffered from relatively low power conversion efficiencies (PCEs) compared to existing PV technologies. However, recent advances in organic-inorganic perovskite solar cells have shifted this paradigm by achieving >22% research cell efficiencies from solution-based active layers.

1.2 PHOTOVOLTAIC DEVICES

1.2.1 *Basic operating principles*

In PV technology, semiconductors directly convert light into electricity by absorbing incoming photons with enough energy to excite electrons from the filled valence band into the empty conduction band. Photo-excited electrons and holes in the conduction band are then separated and collected at two opposite contacts in the device to produce current. Additionally the photoexcited hole and electron populations in the valence and conduction bands, respectively, produce a voltage in the device, which can be used to do work. In conventional p-n junction solar cells, the electrons and holes are separated by an internal electric field; however, charge selective contacts may also be employed to accomplish the same goal.

An ideal solar cell can be modeled as a current source in parallel with a diode as shown in **Figure 1.1(a)** where we assume zero series resistance ($R_S = 0$) and infinite shunt resistant ($R_{SH} = \infty$). The current source represents the photocurrent generated by the solar cell, which is related to

the external quantum efficiency (EQE) of the device and the incident light spectrum, b_s, by the following equation [3]

$$I_{SC} = qA \int b_s(E)\, EQE(E)\, dE \tag{1.1}$$

where q is the electronic charge, A is the active area of the device, and E is the energy of the incident photon. $EQE(E)$ is the probability that the solar cell produces an electron when a photon with energy E is incident upon it. The incident light spectrum, $b_s(E)$, refers to the photon flux density of photons with energy E. For the characterization of solar cells, we use a standardized AM 1.5G solar spectrum shown in **Figure 1.2(a)**. This photocurrent is also referred to as the short-circuit current (I_{SC}) because under short-circuit conditions in the ideal case, the diode current is zero, which makes the circuit current equal to the photocurrent. Because the short-circuit current is proportional to the area of the device, the short-circuit current density (J_{SC}) is often a more useful metric when comparing devices with different active areas.

In dark conditions, J_{SC} = 0, the current density-voltage characteristics is termed the dark current density and follows the diode equation

$$J_{dark}(V) = J_0\left(e^{qV/k_BT} - 1\right) \tag{1.2}$$

where J_0 is a constant called the diode saturation current density, q is the electronic charge, k_B is the Boltzmann constant and T is the temperature in kelvin. Using this model, the solar cell current density under illumination is the superposition of the J_{SC} and J_{dark}, taking into account the opposite current directions in the circuit, as shown in the following equation.

$$J_{light}(V) = J_{SC} - J_{dark}(V) = J_{SC} - J_0\left(e^{qV/k_BT} - 1\right) \tag{1.3}$$

It should be noted that this uses the sign convention that a positive current flows *out of* the positive voltage terminal when a solar cell produces power, which is common in PV literature.

This is in contrast to electrical engineering conventions where a positive current flows *into* the positive voltage terminal of a device and denotes power dissipated by that device.

In **Figure 1.1(b),** representative *J-V* characteristics for a solar cell under light and dark conditions are illustrated, where the rectifying behavior is due to the asymmetry of the charge collection in the device. Several key parameters are extracted from the *J-V* characteristic. The open-circuit voltage (V_{OC}) is determined as the voltage when the current approaches zero (i.e. open-circuit conditions) and the J_{SC} is determined as the current when the applied voltage approaches zero (i.e. short-circuit current conditions). In addition to the V_{OC} and J_{SC}, which are shown in **Figure 1.1(b)**, the power density, *P*, can be calculated at each point where

$$P = JV \tag{1.4}$$

The maximum power density along the *J-V* characteristic is determined and the ratio of that maximum power density relative to the incident illumination power density is the power conversion efficiency (PCE). The maximum power density is achieved at the max power point (MPP), which is referred to by the corresponding max power point voltage (V_M) and max power point current density (J_M). Given the MPP, we can also calculate the fill factor (*FF*) which is defined as

$$FF = \frac{J_M V_M}{J_{SC} V_{OC}} \tag{1.5}$$

The *FF* can provide a metric on some of the non-idealities in the solar cell. For example, if we now imagine some parasitic non-zero R_S and some non-infinite R_{SH} in the equivalent circuit in **Figure 1.1(a)**, this would reduce the PCE and reduce the "squareness" of the *J-V* characteristic relative to the J_{SC} and V_{OC} values. We can also extract R_S and R_{SH} values from the *J-V* characteristic, but in practice *FF* is more commonly reported.

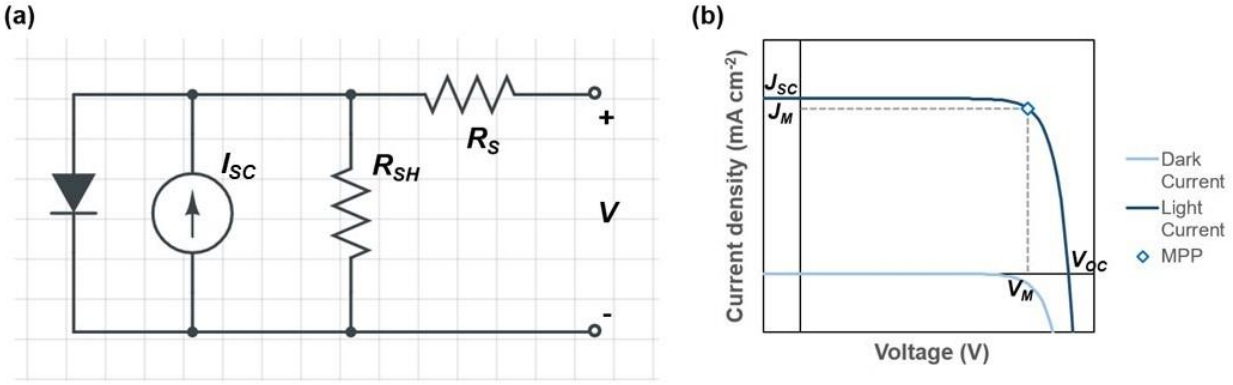

Figure 1.1. Electrical characteristics of a solar cell. **(a)** Equivalent circuit of a solar cell consisting of a diode, the photocurrent source (I_{SC}), shunt resistance (R_{SH}) and series resistance (R_S). **(b)** current-voltage characteristics (J-V) of a solar cell in light (dark blue) and dark (light blue) conditions. The open circuit voltage (Voc), short-circuit current density (J_{SC}), max power point (MPP), max power voltage (V_M) and max power current density (J_M) are denoted on the plot.

1.2.2 *Maximizing power conversion efficiency*

To determine a theoretical maximum PCE of a solar cell, Shockley and Queisser calculated a detailed balance limit [4] where they identified intrinsic loss mechanisms for a solar cell and determined the maximum PCE for a given semiconductor bandgap. In this analysis, they assumed a solar cell consists of a single junction that observes diode I-V characteristics and the incident solar spectrum was a blackbody with temperature of 6000 K. The intrinsic loss mechanisms they identified included: (1) any photons absorbed with energy higher than the bandgap will thermalize down to the bandgap energy, (2) photons with energy less than the bandgap cannot be absorbed and (3) spontaneous emission is required to achieve thermodynamic equilibrium, which produces a maximum open-circuit voltage less than the bandgap energy. These loss mechanisms are illustrated and labeled in **Figure 1.2(b)**. The original analysis performed by Shockley and Queisser was published in 1961, and although the analysis has since been updated to account for an AM 1.5G solar spectrum (**Figure 1.2(a)**) [5], [6] and for multijunction devices [7], [8], the underlying detailed balance limit analysis is still used today. In fact the maximum PCE limit calculated using

a detailed balance limit is often referred to as the Shockley-Queisser (S-Q) limit. Based on this theoretical framework, the maximum PCE for a single junction solar cell is 33.7% for a semiconductor material with a bandgap of 1.34 eV [6].

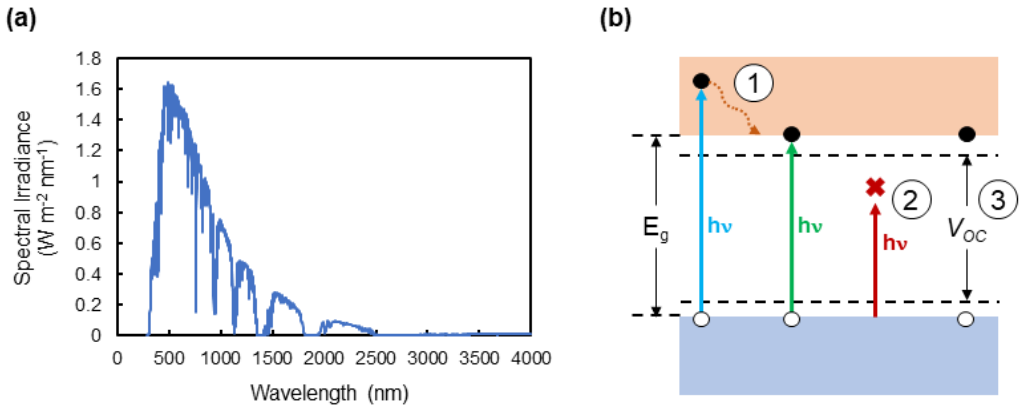

Figure 1.2. Solar spectrum and S-Q limit losses. **(a)** The standard AM 1.5G solar spectrum used to characterize solar cells. **(b)** Absorption of photons with energy greater than the bandgap energy results in the generation of electron-hole pairs. Carriers with energy greater than the bandgap thermalize down to the band edges. Photons with energy less than the bandgap energy are not absorbed. The *Voc* of the solar cell is less than the bandgap energy due to spontaneous emission.

In practice, solar cell efficiencies fall short of the theoretical maximum efficiencies calculated from the detailed balance limit due to additional loss mechanisms such as non-radiative carrier recombination and insufficient light absorption. Strategies to improve PCE are material dependent and may focus on different aspects of the absorber quality or the device architecture. This was highlighted in a recent analysis by Polman *et al*. [6] that reviewed different classes of photovoltaic materials and compared the highest performing devices to its S-Q limit. In-depth analysis comparing the measured J_{SC}, *Voc* and *FF* to the calculated S-Q limit values provided insight regarding the light management versus the carrier management within the solar cell. For example, CdTe and perovskite solar cells have similar power conversion efficiencies, but CdTe has achieved over 95% of the maximum short-circuit current possible. Thus, the light management and charge

collection in CdTe cells has been maximized and further improvements must be focused on improving the V_{OC} and *FF* by reducing recombination at the grain boundaries and interfaces. In contrast, higher V_{OC} values as seen in GaAs and GaInP solar cells reflect its high crystalline quality. For perovskite solar cells, which is the PV system studied in this dissertation, the analysis by Polman *et al*. [6] indicates the champion devices observe a relatively high V_{OC} relative to the maximum S-Q limit, which demonstrates the inherent potential of this semiconductor system, but they suffer from low J_{SC}, which they attribute to parasitic absorption losses, and low *FF*, which they attribute to shunting from pinholes in the active layer and resistive losses from the selective charger carrier interlayers in the device stack.

There are also strategies to exceed the S-Q maximum efficiency limit by circumventing at least one of the initial assumptions used in the detailed balance limit analysis, such as (i) using more than one semiconductor junction in a multijunction cell [7], [8], (ii) extracting multiple electron-hole pairs from a single photon [9], or (iii) preventing the thermalization of hot carriers [10]. Tandem and multijunction cells use multiple semiconductor materials to reduce thermalization loss by absorbing higher energy photons with a higher bandgap material while still absorbing lower energy photons with a lower bandgap material. As seen in the NREL Best Research Cell Efficiency (**Figure 1.3**), the highest record efficiencies are achieved by multijunction solar cells, which are based on expensive III-V materials. However, solution-processable, high efficiency perovskite PV materials present a promising path to lower cost multijunction solar cells. Several key challenges include developing high quality materials in a wide range of different bandgap energies and developing interlayers between the junctions with efficient charge transfer, optical transparency, and chemical compatibility within the device stack.

1.2.3 *Impact of durability on cost competitiveness*

The durability of a solar panel is critical to its cost competitiveness compared to other energy technologies. One metric used to compare the cost of different energy sources is the levelized cost of energy (LCOE), which estimates the total cost to generate the electricity over the total amount of energy generated over the lifetime of the photovoltaic system. Although LCOE requires many assumptions and can only yield a crude estimate, it is likely a metric used by investors and developers seeking to build new power plants. According to the U.S. Energy Information Administration, the LCOE for a solar PV plant entering in 2020 is $125.30 per MWh, whereas the LCOE for a conventional coal plant is $95 per MWh. To become cost competitive with conventional coal, the cost of the solar PV plant must be reduced to 75.8% of its current cost, while maintaining the amount of energy generated over the lifetime of the plant. Solution-processed photovoltaics are projected to dramatically reduce the cost of a PV module compared to conventional silicon, but they must also generate the same amount of energy over its lifetime; thus highlighting the need for both durability and efficiency. Lifetime is particularly important to absorb the initial soft costs of installation, procurement, engineering, and construction, as well as other hardware costs, including inverters, racks, etc. Typical LCOE estimates use solar panel lifetimes of 20-40 years [11], which is an important benchmark for emerging PV technologies. It is also important to note that the PV module itself can be as little as one-third of the total cost of a residential system [12]. Thus, even if the PV module cost were virtually free, it would still need to generate sufficient energy generated over its lifetime to account for the soft costs, which therefore requires robust PV materials.

1.3 PEROVSKITE SOLAR CELLS

1.3.1 *The rapid rise of perovskite solar cells*

In 2009, Miyasaka *et al*. published the seminal organic-inorganic lead halide perovskite solar cell paper [13], where they reported that methylammonium lead triiodide ($CH_3NH_3PbI_3$, herein referred to as $MAPbI_3$) and methylammonium lead tribromide ($CH_3NH_3PbBr_3$, herein referred to as $MAPbBr_3$) could be used as a visible-light sensitizer in a photoelectrochemical cell. They achieved a maximum PCE of 3.81% from the $MAPbI_3$ sensitizer and a high open-circuit voltage of 0.96 V from the $MAPbBr_3$ sensitizer. Two years later Nam-Gyu Park *et al*. fabricated a 6.5% efficient $MAPbI_3$ quantum dot (QD) sensitized solar cell by increasing the precursor solution concentration and by using a different electrolyte solution; however, this device still suffered from poor stability with the PCE dropping to 20% of its initial value after 10 min of constant illumination [14]. In 2012, two important discoveries emerged; first, a solid-state hole transport layer could replace the liquid electrolyte and therefore, solve the more immediate stability issues [15], [16] and second, the perovskite material does not merely sensitize the TiO_2, but is a semiconductor capable of efficient charge transport [16]. These advances led to devices up to 10.9% efficient, which spurred immense interest in the PV research community. The first certified record research cell efficiency was claimed by EPFL in 2013 at 14.1%. A mere three years later, the current certified record efficiency rose to 22.1%, which was achieved by the Korea Research Institute of Chemical Technology and Ulsan National Institute of Science and Technology. As seen in the National Renewable Energy Laboratory (NREL) Best Research-Cell Efficiency chart in **Figure 1.3**, this current perovskite solar cell record rivals that of other commercialized thin film technologies and even some silicon wafer based materials.

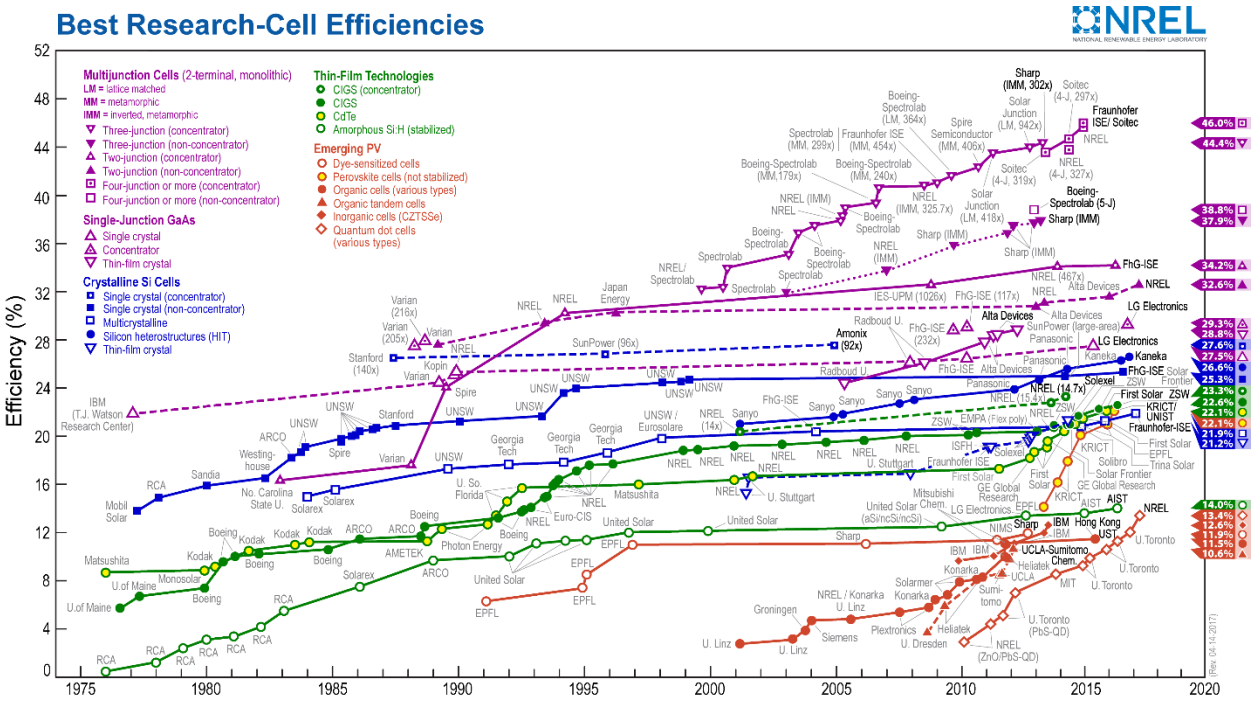

Figure 1.3. NREL best research cell efficiency chart [17]. Perovskite solar cells are shown in red-outlined, yellow-filled circles and have achieved a record power conversion efficiency of 22.1% as of April 20, 2016.

The term perovskite refers to the ABX_3 crystal structure, which was originally associated with $CaTiO_3$. In lead halide perovskite materials, the A-site cations of primary interest are methylammonium (MA^+), formamidinium (FA^+), and cesium (Cs^+). The B-site cation is Pb^{2+}, however other metals in the +2 oxidation state, such as Sn^{2+} or Ge^{2+}, can also be substituted for lead. The X_3 anion is the halide site where I^-, Br^-, and Cl^- or mixtures of these halides have been demonstrated in PV applications. A schematic of the perovskite crystal structure is shown in **Figure 1.4**. Although initial studies on metal halide perovskite focused on $MAPbI_3$, research in alloying and replacing different constituent ions yielded wide variety of different chemical compositions compatible with the perovskite crystal structure. These various perovskite materials demonstrated a wide range of tunable bandgap energies and enhanced photovoltaic performance and stability [18]–[23].

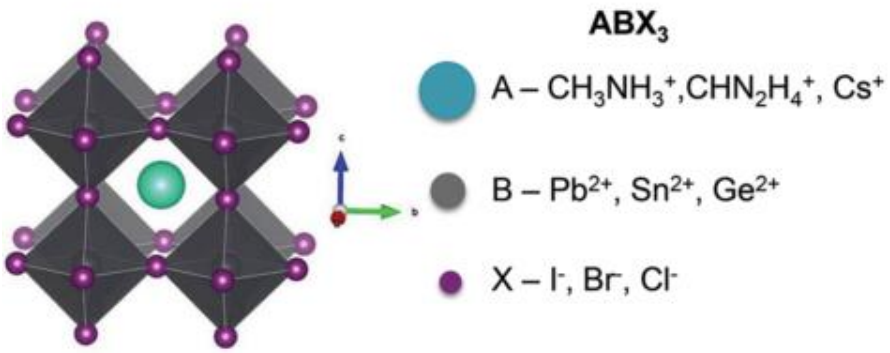

Figure 1.4. Perovskite crystal structure [24]. The ABX_3 perovskite crystal structure is shown with different cation and anion possibilities, which shows the combinatorial space of different metal halide materials relevant for photovoltaic applications. Reprinted with permission from Leijtens T. *et al*. (2015). Adv. Energy Mater., 5: 1500963. Copyright 2015 WILEY-VCH Verlag GmbH & Co. KGaA, Weinheim.

Metal halide perovskite materials, and $MAPbI_3$ in particular, have several qualities attractive for PV applications. From a fabrication stand point, it is solution-processable and the crystal formation energy of $MAPbI_3$ is relatively low [25], which means that thin films readily crystallize at low temperatures. Solution-processability and a low thermal processing can enable the use of low-cost, high-throughput roll-to-roll deposition methods. Metal halide perovskite materials also have relatively high absorption coefficients, which means that thinner films are required for sufficient light absorption. **Figure 1.5(a)** shows that $MAPbI_3$ has a sharp absorption onset and a high absorption coefficient similar to GaAs [26]. In addition to the desirable optical properties, $MAPbI_3$ also has a high defect tolerance, which is particularly important for low-temperature, solution-processed materials because these deposition methods yield polycrystalline films with grain boundaries and large surface areas. Density-functional theory calculations of formation energies and the transition energy levels of the different possible defects, indicate that the defects that create deep levels such as anti-site substitutions of I_{Pb}, I_{MA}, and Pb_I as well as interstitial Pb (Pb_i) have very high formation energies. In contrast, other defects such as vacancies (V_{MA}, V_{Pb},

V_I), MA and I interstitials (MA_i and I_i, respectively), cation substitutions (MA_{Pb}, Pb_{MA}) and the MA_I anti-site substitution yield shallow energy levels, which is illustrated in **Figure 1.5(b)** [27]. These are just a few of the many desirable properties that make metal halide perovskite solar cells a promising candidate for PV applications.

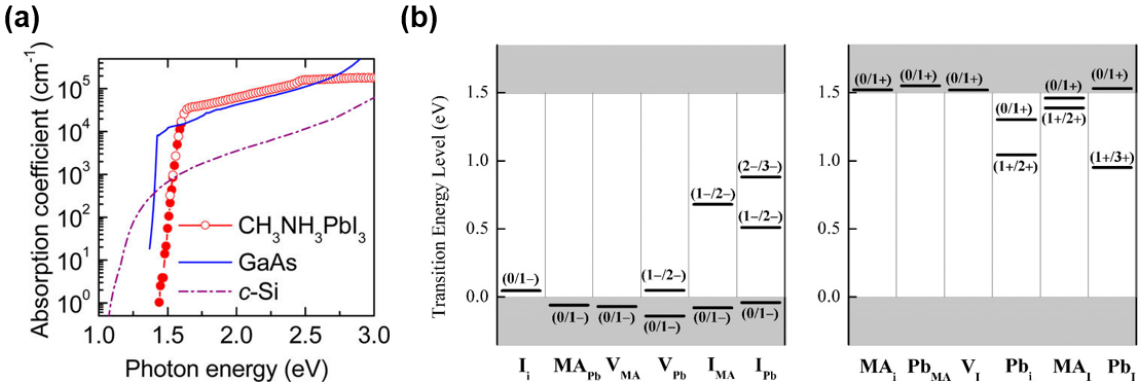

Figure 1.5. High absorption and defect tolerance of $MAPbI_3$ perovskite. **(a)** Absorption coefficients of $MAPbI_3$, GaAs and crystalline Si. Reprinted with permission from S. De Wolf *et al*. (2014) *J. Phys. Chem. Lett.*, 5 (6), 1035–1039. Copyright 2014 American Chemical Society. [26] **(b)** Simulated transition energy levels of different types of defects in $MAPbI_3$ perovskite. The deep level defects shown here (*i.e.* I_{MA}, I_{Pb}, Pb_I, and Pb_i) have high formation energies, whereas the defects with lower formation energies result in shallower energy levels. Reprinted from Yin *et al.* (2014) *Appl. Phys. Lett.*, 104, 063903. with the permission of AIP Publishing. [27]

1.3.2 *Challenges with stability and strategies toward improvement*

Despite the impressive PCEs exhibited by solution-processed perovskite solar cells, there are major concerns regarding their stability. Seok *et al.* provided some of the first degradation data of completed $MAPb(I_{1-x}, Br_x)_3$ solar cells, which showed that a single day in humid conditions reduced >10% efficient $MAPbI_3$ solar cells down to less than 6% efficient, and that these cells continued to decline to less than 4% PCE even when moved to lower humidity conditions after that initial exposure [18]. This indicates that the mere exposure to high humidity conditions can have a lasting impact on the degradation. In a particularly severe case, Yang *et al*. reported

perovskite solar cells with a maximum efficiency as high as 19.3% degraded to less than 20% of its initial efficiency after 24 h in ambient. A similar storage test in N_2 revealed that these solar cells degraded to less than 50% of its initial efficiency after 48 h in an inert environment [28]. Although the degree of degradation varies significantly depending on device architecture and storage conditions, these early reports highlight the concern and need for further research in stability perovskite solar cells.

In the following sections, I will first discuss the stability issues of methylammonium lead halide perovskite materials and devices, which is the perovskite active layer used in Chapter 2 of this dissertation. Next, I will address the growing work in using alternative A-site cations, in particular focusing on the inorganic cation Cs^+, and the phase stability issues facing these materials, which forms the basis of the work presented in Chapters 3 and 4.

1.3.3 *Stability studies on methylammonium-based perovskite solar cells*

Recently, stability studies have been conducted on $MAPbI_3$ films and devices and provided insight on the role of light, heat, and ambient environmental conditions [28]–[35]. Several reviews regarding stability have recently been published [24], [36], [37]. Here I will address some of degradation pathways that have been proposed and strategies to overcome these issues.

Ambient moisture has long been reported to degrade perovskite solar cells and films. Optically dark brown perovskite films exposed to ambient humidity decompose into yellow PbI_2 films [30], [33], [38]. One proposed pathway by Niu *et al*. is summarized in the following equations:

$$CH_3NH_3PbI_3 \leftrightarrow PbI_2\ (s) + CH_3NH_3I(aq) \quad (1.6)$$

$$CH_3NH_3I(aq) \leftrightarrow CH_3NH_2\ (aq) + HI\ (aq) \quad (1.7)$$

$$4HI\ (aq) + O_2(g) \leftrightarrow 2I_2(s) + 2H_2O\ (l) \quad (1.8)$$

$$2HI\ (aq) \leftrightarrow 2H_2(g) + 2I_2\ (s) \quad (1.9)$$

In these proposed mechanisms, however, oxygen and light facilitate decomposition to PbI_2. In Eqn. (1.8) oxygen is required for the redox reaction to occur, and in Eqn. (1.9) UV irradiation is required for the photochemical reaction to take place [37]. In addition to decomposition of the perovskite into PbI_2, moisture can also lead to a hydrated perovskite presumably in the absence of sufficient oxygen or UV illumination [34], [39]. The hydrated perovskite is a reversible effect, but nonetheless is undesirable during device operation due to a significant decrease in absorption across the visible spectrum.

One of the primary strategies employed to prevent decomposition of $MAPbI_3$ solar cells from degrading in ambient humidity is to prevent the ingress of moisture. Some common approaches include encapsulation techniques [40], [41], incorporating buffer layers [29], [42], [43], or introducing more robust or hydrophobic hole-transporting layers and electrodes [44]–[46]. Alternatively, some groups have altered the perovskite chemistry or deposition method to harden the perovskite active layer itself from the ill effects of moisture [18], [32], [33], [47], [48]. Although the results of these studies are promising, it is difficult to compare one result to another due to a lack of standardization. In some cases, the stability is determined through a shelf-life study in unspecified laboratory ambient conditions, whereas other stability studies report constant operating lifetimes. Since illumination plays a critical role in the decomposition of $MAPbI_3$, as evidenced by Eqn. (1.9), more rigorous, constant operation lifetimes are necessary to assess a meaningful perovskite solar cell lifetime. Standardized stability testing protocols are discussed and implemented on $MAPbI_3$ perovskite solar cells in Chapter 2.

In addition to moisture, the roles of oxygen [35], [49], illumination [32], [50], [51], and heat [31], [32] in the degradation of $MAPbI_3$ have also been studied. Although one may engineer a barrier to prevent oxygen exposure, this may not be a viable solution if spiro-OMeTAD is used as

the hole-transporting layer because spiro-OMeTAD requires some level of oxygen doping to achieve the maximum conductivity [52], [53]. Some illumination, such as high energy UV light, could be filtered to improve solar cell lifetime, but that also prevents those high energy photons from contributing to the photocurrent and potentially adds cost and complexity to the device design. Heat, however, is the most troubling cause of degradation because designing a cost-effective cooling system is highly impractical. Boyen *et al*. revealed that thermally annealing a $MAPbI_3$ film in an inert environment at 85 °C for 24 h can significantly reduce the conductivity of the film, as seen in **Figure 1.6** [31]. Over the life cycle of a solar panel, this could be extremely problematic in warm climates and does not meet solar industry standards. Therefore, it is likely that replacing the MA^+ cation will need to be replaced with a thermally stable alternative.

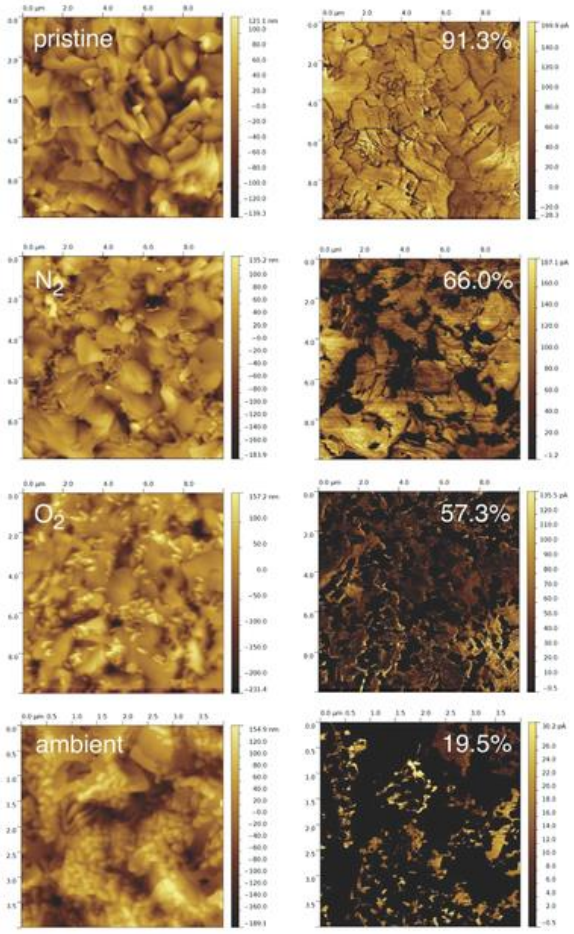

Figure 1.6. AFM and conductive AFM images of pristine and annealed films [31]. AFM images (left column) and conductive AFM images (right column) of pristine films (top row) and films thermally annealed at 85 °C for 24 h in an inert environment (second row), in an O2-containing environment (third row), and ambient environment (bottom row). A significant decrease in conductivity is observed in all three cases, with greater losses observed as O_2 and H_2O are introduced to the environment. Reprinted with permission from B. Conings *et al*. (2015). *Adv. Energy Mater.*, 5, 1500477. Copyright 2015 WILEY-VCH Verlag GmbH & Co. KGaA, Weinheim. [31]

1.3.4 *Stability of inorganic perovskite chemistries*

Due to the decomposition of $MAPbI_3$ at 85 °C and the volatility of MA^+ alternative A-site cations, such as FA^+ and Cs^+, are of great interest. However, these alternatives experience phase stability issues because of the relative sizes of the ions. The Goldschmidt tolerance factor (*t*) can provide

general guideline to the resulting crystal structure [54], and can be calculated using the following formula:

$$t = \frac{r_A + r_X}{\sqrt{2}(r_B + r_X)} \tag{1.10}$$

where r_A is the ionic radius of the A-site cation, r_B is the ionic radius of the B-site cation, and r_X is the ionic radius of the halide anion. For metal halide perovskites, if the tolerance factor, t, is between 0.8 and 1, the crystal will likely exhibit the have a cubic perovskite structure. A tolerance factor below 0.8 will typically result in an orthorhombic phase and tolerance factors greater than 1 typically yield hexagonal structures. As seen in **Figure 1.7**, the tolerance factor for $MAPbI_3$ is ideal for the cubic perovskite phase, whereas the tolerance factors for $CsPbI_3$ and $FAPbI_3$ are near the edge of the desired range for the cubic perovskite phase.

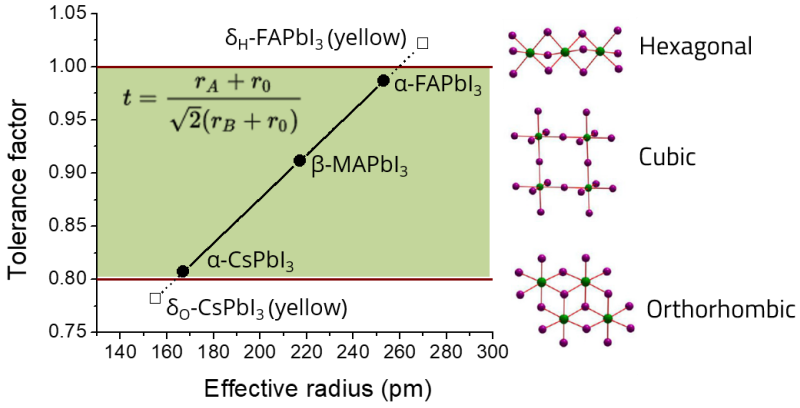

Figure 1.7. Tolerance factor $APbI_3$ perovskite as a function of A-site cation radius [20]. The ionic radii of Cs and FA place the tolerance factors for $CsPbI_3$ and $FAPbI_3$ outside of the range typical for cubic perovskite structures. A with permission from Z. Li *et al*. (2016). *Chem. Mater*., 28 (1), 284-292. Copyright 2016 American Chemical Society.

In this dissertation, I focused on the all-inorganic $CsPbI_3$ perovskite because it is compositionally stable up to its melting point, which is in excess of 400 °C [55]. However, at room temperature $CsPbI_3$ prefers the orthorhombic phase, which has a significantly larger bandgap than

the cubic perovskite phase. To stabilize the cubic phase, researchers have successfully alloyed the halide site with I and Br to achieve phase stable cesium lead halide perovskite solar cells [56]–[58]. Although the addition of Br improves the phase stability, it also increases the bandgap from an already large ~1.73 eV for the pure iodide composition to 1.9 eV for $CsPbI_2Br$ [57], [58]. The first demonstration of a $CsPbI_3$ perovskite solar cell, published by Eperon *et al.* [59], found that adding HI to the precursor solution reduced the phase transition temperature of the cubic perovskite phase from 335 °C without the additive down to 100 °C with the additive. Scanning electron microscrope (SEM) images of the films made with and without HI as an additive reveal smaller grain sizes in the film when HI was added as seen in **Figure 1.8**. The lower phase transition temperature and improved ambient stability of the smaller grain film is consistent with the air-stable, cubic phase $CsPbI_3$ nanocrystals reported by Kovalenko *et al*. [60] Thus, smaller grains or nano-sized crystals stabilize the desired cubic perovskite phase in $CsPbI_3$. In Chapter 3, I demonstrate that $CsPbI_3$ quantum dots (QDs) can successfully maintain the cubic perovskite phase, which can then be used to fabricate efficient solar cells.

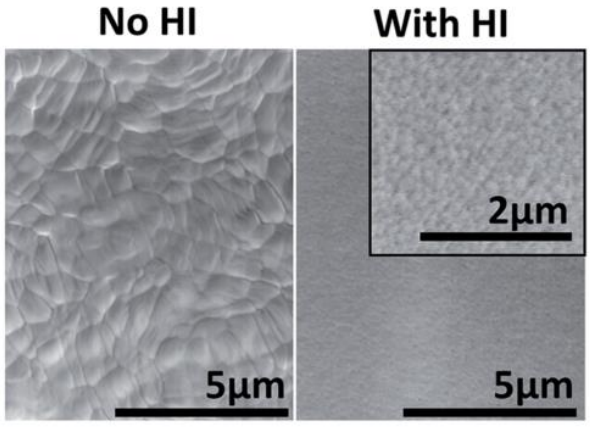

Figure 1.8. SEM images of $CsPbI_3$ films fabricated with and without HI additive. The films made with HI in the precursor solution have smaller domain sizes compared to the film made without HI as an additive. Adapted from Ref [59] with permission of The Royal Society of Chemistry.

1.4 QUANTUM DOT SOLAR CELLS

1.4.1 *Quantum confinement*

QDs are semiconductors with physical dimensions comparable to or smaller than the Bohr radius of an exciton in that particular material. A Bohr radius is a *natural length scale* specific to the particle of interest (in this case, excitons) in a specific material. The Bohr radius can be calculated for different particles, including electrons, holes and excitons, and is defined as

$$a_B = \varepsilon \frac{m}{m^*} a_0 \tag{1.11}$$

where ε is the dielectric constant of the material, m^* is the mass of the particle of interest, m is the rest mass of the electron, and a_0 is the Bohr radius of the hydrogen atom [61]. When the semiconductor dimensions are smaller than the Bohr radius of a particle, it restricts that particle to the physical size of the QD, which has implications on the density of available electronic states and the energy levels of those states.

The confinement energy of a zero-dimensional QD is approximated by the solution to Schrodinger's equation for the particle-in-a-box model. This solution results in discrete of the energy levels and a $1/L^2$ dependence of the confinement energy, where L is a length scale of the box. To improve the theoretical model, we can apply several approximations (see Refs. [61], [62] for further details), to arrive at the following equation for the electron-hole pair energies in a QD [62]:

$$E_{g,QD} \cong E_{g,bulk} + \frac{\hbar^2 \pi^2}{2R^2}\left(\frac{1}{m_e} + \frac{1}{m_h}\right) - \frac{1.8e^2}{\varepsilon R} \tag{1.12}$$

where R is the radius of the QD, m_e is the electron effective mass, m_h is the hole effective mass and e is the charge of an electron. The second term includes the confinement energy derived by the particle-in-a-box analysis applied to both the hole and electrons. The third term in Eqn. 1.12

represents an energy correction to account for the Coulombic attraction between the electron and hole within the QD. From Eqn. 1.12, it is apparent that reducing the size of the QD increases the bandgap energy. Bandgap tunability is useful for photovoltaics as the S-Q analysis demonstrates the impact of bandgap on maximum PCE. Additionally, the QD band structure and the localization of carriers can lead to unique photophysics, such as multiple exciton generation (MEG) in which more than one exciton is generated from a single photon. MEG has been theorized [10] as a path for solar cells to exceed the S-Q detailed balance limit, and the phenomenon has been demonstrated to produce over 100% external quantum efficiency in solar cells [63] and photoelectrochemical cells [64].

1.4.2 *Quantum dot solar cells*

In addition to the unique photophysical properties of QDs imparted by quantum confinement, colloidal QDs can also be solution-processed like thin film metal halide perovskites, which enables the use of low-temperature, high throughput deposition methods. The surface chemistry of QDs are highly tunable, which enables tunability in electronic band positions and doping [65]–[67], enhancement of optoelectronic properties [68], [69], and enhanced stability [70], [71]. Lead chalcogenide QDs are the most widely studied QDs for PV applications due to their low bandgap, which is desirable for MEG, and their robust synthetic methods. In Chapters 3 and 4, I focus on $CsPbI_3$ perovskite QDs, but many of the techniques used to fabricate our $CsPbI_3$ QD devices are based on the existing knowledge and expertise built on lead chalcogenide quantum dot solar cells (QDSC).

The first step in making a colloidal QDSC is to synthesize the QDs. Conventional QDs are synthesized though a hot-injection method [61], but heat-up syntheses [72] and even room-temperature syntheses [73] can also yield high quality nanocrystals. In order to maintain colloidal

stability and passivate surface states, QDs are stabilized with ligands. Typically these ligands contain long, insulating alkyl chains. Although these ligands provide desirable colloidal stability, they are problematic in forming conductive optoelectronic films. Replacement of these insulating ligands, often termed "ligand exchange," is critical to improving charge transport, but can also passivate defect states, and improve band alignment through tuning of the electronic band positions to induce drift transport. Thus, many of the advances in QDSCs are enabled through ligand exchange schemes [67], [68], [71], [74]–[76]. The specific details of how electronically coupled lead chalcogenide QD arrays are fabricated and efficient QDSCS are produced was reported in a recent protocols paper [77].

1.5 SCOPE OF THIS WORK

This dissertation consists of 5 chapters. In this first chapter, I aimed to motivate why lead halide perovskite materials are of great interest to the PV research community and provide background on solar cells, perovskite solar cells and QDs. In the second chapter, the operational stability of $MAPbI_3$ thin film solar cells is characterized and improved through careful optimization of the electrode configuration. In Chapter 3, the thermally unstable organic cation in $MAPbI_3$ is replaced with Cs to fabricate an all-inorganic $CsPbI_3$ QD solar cell. In Chapter 4, I developed a surface modification using A-site cation halide salt treatments to improve the $CsPbI_3$ QD film mobility and achieve the QDSC record efficiency. In Chapter 5, I summarize this dissertation work and propose future work based on the results demonstrated here.

Chapter 2. ENHANCING PEROVSKITE SOLAR CELL STABILITY WITH ELECTRODE INTERFACE ENGINEERING

Adapted with permission with from:
Sanehira, E. M.; Tremolet de Villers, B. J.; Schulz, P.; Reese, M. O.; Ferrere, S.; Zhu, K.; Lin, L. Y.; Berry, J. J.; Luther, J. M. Influence of Electrode Interfaces on the Stability of Perovskite Solar Cells: Reduced Degradation using MoO_x/Al for Hole Collection. *ACS Energy Lett.*, **2016**, *1* (1), pp 38-45.

2.1 ABSTRACT

We investigate and characterize the stability of the power output from methylammonium lead iodide perovskite photovoltaic devices produced with various hole-collecting anode configurations consisting of Au, Ag, MoO_x/Au, MoO_x/Ag, and MoO_x/Al. The unencapsulated devices were operated under constant illumination and constant load conditions in laboratory ambient with periodic current-voltage testing. Although the initial efficiencies of devices were comparable across these configurations, the stability of these devices varied significantly due to subtle differences in the electrode structure. Specifically, we find that devices with MoO_x/Al electrodes are more stable than devices with more conventional, and more costly, Au and Ag electrodes. We demonstrate that a thin MoO_x layer inhibits decomposition of the perovskite films under illumination in ambient laboratory conditions, but that greater improvements in device stability are achieved specifically with MoO_x/Al electrodes. We investigated the role of the MoO_x interlayer in the MoO_x/Al electrodes by exploring the effect of relative humidity and the MoO_x interlayer thickness on the perovskite solar cell stability.

2.2 INTRODUCTION

Organic-inorganic metal halide perovskite materials have garnered significant interest in the photovoltaic community with record certified power conversion efficiencies (PCEs) as high as 22.1% in recent years [78]. These perovskite materials, such as $CH_3NH_3PbI_3$ ($MAPbI_3$), have low crystal formation energies [25] and are amenable to solution processing while also possessing favorable optoelectronic properties such as high optical absorption [26], high ambipolar mobilities [79], and unique tolerance to structural defects [80], [27]. Although a plethora of work has been and continues to be conducted on film deposition techniques [81]–[84], surface passivation [85]–[87], and device architectures [16], [28] to improve PCEs, device stability still remains a primary concern [37], [88]. Durability is critical for commercialization because a minimum lifetime is necessary to offset and exceed the initial monetary investment in not only the photovoltaic devices themselves, but also costs associated with the balance of system (e.g. installation). Furthermore, stability is of great environmental concern due to the potential for moisture to decompose an exposed $MAPbI_3$ solar panel and leach lead into the environment [89]. Given a solubility of 760 mg/L for PbI_2 in water at 25 °C [90], robust solar cell design must be implemented to prevent the release of lead pollutants, especially on rooftops and near water sources.

Previous studies on the stability of $MAPbI_3$ have shown that light, heat, and ambient environment can degrade perovskite films [29]–[31] and crystals [29]. Shelf-life studies of perovskite solar cells have demonstrated the instability of perovskite films in ambient [28], [29], [33], while studies in more controlled environments suggest that moisture [30] is the main culprit of perovskite degradation in dark conditions. Beyond shelf-life studies, constant operation of perovskite solar cells encapsulated with epoxy resin and coverslip glass has yielded relatively high lifetimes of hundreds of hours [50], [81]. Although the extended lifetimes of these encapsulated

devices are promising, encapsulant materials inevitably allow some moisture ingress over time [91]. Hardening a device structure to the effects of the environment is by far preferable than relying on packaging – which can be costly and may fail – for protection. Adding further complexity, illumination contributes additional photoinduced degradation pathways depending on the environmental conditions and electron-transporting layer. In inert environments, Leijtens *et al.* showed that ultraviolet light leads to the formation of deep electron traps in TiO_2 [50], whereas Aristidou *et al.* demonstrated that adding dry air to illumination triggers decomposition by reactive oxide species [35]. In the former study, stability increases by replacing mesoporous TiO_2 with an Al_2O_3 scaffold, but in contrast, the latter study indicates that TiO_2 reduces superoxide formation compared to an Al_2O_3 scaffold, and therefore enhances device stability. Given the complex interaction of illumination, environmental agents, and various components in the device architecture, it is critical to characterize and study the degradation of devices under constant operating conditions in ambient atmospheres to gain insight relevant to real world applications.

In addition to encapsulation with glass and epoxy, researchers have also successfully implemented Al_2O_3 buffer layers [29], [42], [43], hydrophobic oligothiophene hole-transporting layers [44], pinhole-free 2,2′,7,7′-tetrakis(N,N-di-p-methoxyphenylamino)-9,9′-spirobifluorene (Spiro-OMeTAD) hole-transporting layers [53], polymer/carbon nanotube composites [41], and thick carbon electrodes [46], [92] to enhance device stability. To date, the most stable organic-inorganic perovskite solar cells have been based on a hole-conductor-free architecture with a 10-μm-thick carbon electrode through which a mixed cation perovskite based on methylammonium and 5-aminovaleric acid is drop-casted [46], [92]. The enhanced stability of these unencapsulated devices was attributed to the water-retaining properties of the carbon electrode that prevent the

ingress of moisture, which highlights the importance of device architecture and electrode selection on the device stability.

Although Au and Ag are most commonly used for the metal electrodes in organic-inorganic perovskite solar cells, Zhao *et al.* previously reported that a MoO_x/Al contact could also be used as a cost-effective alternative [93]. This type of contact uses an oxygen-deficient molybdenum trioxide (herein referred to as MoO_x) layer, which has a high work function that enables efficient hole extraction [94]. MoO_x interlayers have been used previously to improve performance and stability in organic light-emitting diodes [95], [96], organic photovoltaics [97]–[99], and quantum dot solar cells [100], [101].

Here, we study the effects of using various hole-collecting anode configurations on the initial $MAPbI_3$ solar cell efficiency and the device stability. Specifically, we examine the effect of adding a MoO_x hole-extraction layer to commonly used metals such as Au, Ag, and Al, as shown in Fig. 1. First, we find that adding a thin (15 nm) MoO_x layer on $MAPbI_3$/Spiro-OMeTAD films provides conformal coverage and reduces decomposition of the $MAPbI_3$ films under illumination in ambient conditions. Next, we fabricated devices with MoO_x/Al electrodes and characterized the stability in varying humidity conditions. To determine if the MoO_x was serving as an encapsulation layer, we varied the thickness of the MoO_x layer and found that although all devices possess the same initial efficiency, the devices with thinner MoO_x are more stable over time. These results indicate that the MoO_x is not improving the device by reducing the amount of moisture introduced to the device. Instead, the device stability is likely enhanced by specific details at the MoO_x/Al interface, which do not affect the initial device efficiency. We then observe a greater resistance to degradation for devices employing a MoO_x/Al electrode as compared to devices with more conventional Au or Ag electrodes. Furthermore, the device durability is not only dependent on the use of a MoO_x hole-

extraction layer, but more specifically dependent on the MoO_x/metal combination with MoO_x/Al electrodes yielding the highest stability. We emphasize that *all stability studies were conducted by operating devices with different electrode configurations under constant illumination and constant resistive load in laboratory ambient conditions.* By monitoring the devices during constant operation, we observe significant differences in the degradation behavior of devices employing different back electrode configurations.

2.3 METHODS

2.3.1 *Materials synthesis and device fabrication*

Materials. All chemicals were purchased from Sigma-Aldrich and used as received unless otherwise specified. Methylammonium iodide (CH_3NH_3I) was synthesized using a modified procedure of Bolink *et al* [102]. In a typical preparation, 139 mL (1.05 mol) HI (stabilized, 57 wt%) were added to a 500-mL Erlenmeyer flask and immersed in an ice/salt bath. 104 mL (1.20 mol) of methylamine (aqueous, 40 wt%) were added slowly to the stirred solution. The reaction mixture was stirred and the bath temperature maintained below 5°C for about 2 h. Subsequently, the volume of water was reduced by rotary evaporation at 50 °C. Ethanol (~100 mL) was added and white crystals were collected by vacuum filtration. The crystals (56.0 g) were dried in a vacuum oven (50 °C). A second crop of crystals (24.3 g) was collected from the ethanolic filtrate. The total crude yield (~80 g) was 48%. The crystals were further purified by repeated recrystallization from ethanol.

Perovskite film fabrication. $MAPbI_3$ perovskite films were deposited by a slightly adapted solvent-engineering procedure reported by Jeon *et al* [103]. A 1.3M solution of CH_3NH_3I (MAI) and PbI_2 in a 7:3 (v/v) mixture of gamma-butyrolactone (GBL) and dimethylsulfoxide (DMSO)

was spin-coated onto the TiO_2 layers to achieve a film thickness of ~250–300 nm. A toluene drip was cast during the spin-coating process to remove residual DMSO and produce a smooth, compact film. The resultant transparent film was annealed at 100 °C for 15 min to fully convert the precursor into a smooth, dense perovskite film.

Solar cell device fabrication. Prepatterned FTO (Thin Film Devices, Inc.) was cleaned by sonication in acetone and 2-propanol prior to 20 min of ultraviolet ozone cleaning. A ~60 nm blocking TiO_2 layer was deposited from a sol-gel method [68] followed by a thin ~50 nm mesoporous TiO_2 layer consisting of ~33 nm TiO_2 nanoparticles in an ethanol, ethyl cellulose, terpineol ink formulation [104]. The perovskite photoactive layer was deposited using the procedure described above. The hole-transporting layer was spin-coated from a solution consisting of 72.3 mg of spiro-OMeTAD (Lumtec, >99.5%) dissolved in 1 mL of chlorobenzene, 28.8 μL of 4-*tert*-butylpyridine, and 17.5 μL of a bis(trifluoromethane)sulfonimide lithium salt (Li-TFSI) solution. The Li-TFSI solution consisted of 520 mg of Li-TFSI dissolved in 1 mL of acetonitrile. The solution was spin-coated at 4,000 rpm for 25 s to achieve a film thickness of ~100 nm. All of the spin-coating processes were performed in ambient. The MoO_x interlayer was deposited on spiro-OMeTAD at a rate of 0.2–1.0 Å/s at a base pressure lower than 4×10^{-6} mbar. The thickness of the MoO_x was varied from 8 to 200 nm. Metal electrodes (i.e., Ag, Au, or Al) were evaporated through a shadow mask at a rate ranging from 0.5–2 Å/s for a total thickness of 200 nm. In metal-only electrode configurations, the metal was deposited directly on the spiro-OMeTAD layer. A schematic of the completed device stack and a cross-section SEM image of a completed device is provided in **Figure 2.1**.

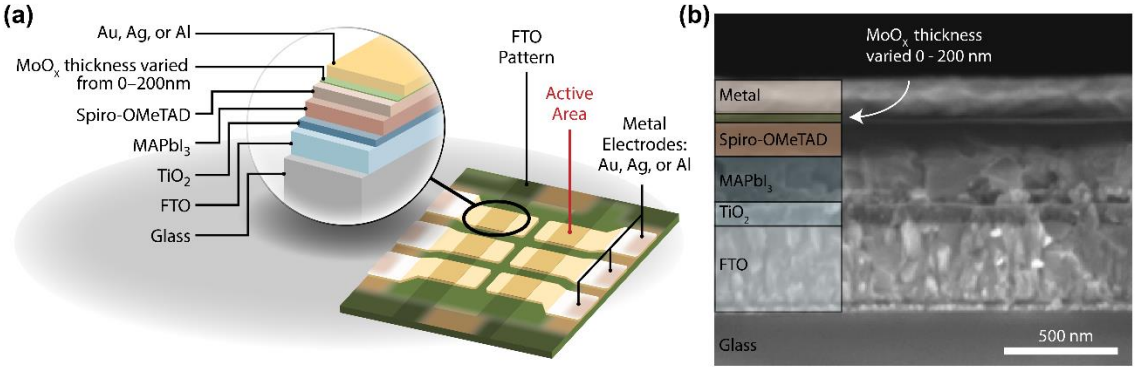

Figure 2.1. Schematic representation of the $MAPbI_3$ perovskite solar cell and cross-sectional scanning electron microscope image. **(a)** Schematic representation of the layer structure in cross-section and top-down view of a completed photovoltaic device. The active area of a solar cell is defined by the overlap of the metal electrode and patterned FTO strip, denoted as the darker gold region on the metal electrodes. During measurement, a metal aperture mask is placed over the glass substrate with precisely positioned holes to ensure that illumination only occurs on the active area. Each substrate has six individual devices. **(b)** Scanning electron microscopy cross-sectional image of a perovskite solar cell with individual layers labeled.

2.3.2 *Film characterization, photovoltaic device testing and stability measurements*

Film characterization. Transmittance and diffuse reflectance measurements were acquired by a Shimadzu UV-3600 UV-Vis NIR spectrophotometer with an integrating sphere. Photodegradation studies were conducted in laboratory ambient with illumination from a 4-bulb array of Eiko Solux tungsten-halogen light source (50 W, MR16 bulbs with a color temperature of 4700 K) with a light intensity calibrated to ~1-sun flux. Photoemission experiments were performed in a Kratos AXIS Nova photoelectron spectrometer operated at a base pressure of 1×10^{-9} mbar. XPS spectra were taken using monochromated Al Kα radiation (1486.7 eV) at a resolution of 400 meV. The acquired spectra were calibrated to the Fermi edge of a sputter-cleaned Au surface.

Device testing. After fabrication, devices were stored and initially measured in a N_2-filled glove box. The *J-V* characteristics were recorded with a Keithley 2400 SourceMeter and controlled by a LabView program designed in-house. The scan direction was set from +1.2 V to -0.2 V, with

0.01 V steps, and a scan rate of 0.2 V/s. We also scanned devices in the forward direction from -0.2V to 1.2V and observed hysteresis (**Figure 2.2(a)**), which is common in lead halide perovskite solar cells. The stabilized power output (**Figure 2.2(b)**) yielded an efficiency value close to the PCE value obtained from the reverse *J-V* scan, which is in agreement with the literature [105]. A solar simulator (Newport, Oriel Sol3A) equipped with an AM1.5 filter and calibrated with an NREL-certified Si photodiode illuminated the devices through a metal aperture with an active area defined as 0.06 cm^2. The EQE was measured with a Newport Oriel IQE-200 with a chopping frequency of 60 Hz.

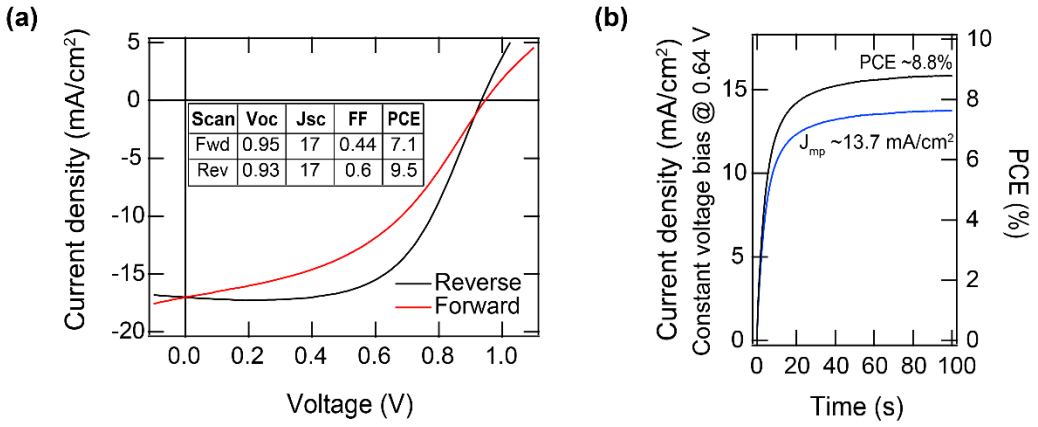

Figure 2.2. Hysteresis observed in *J-V* scans and stabilized output power. **(a)** *J-V* plots of a typical photovoltaic device scanned in the forward and reverse directions in red and black, respectively. **(b)** The stabilized photocurrent density of the same device held at a constant voltage of 0.64V. The stabilized power conversion efficiency at 0.64V is in better agreement with reverse direction *J-V* scans than the forward direction *J-V* scans.

Stability measurements. Stability testing was conducted with a large-area, modular device array testing apparatus designed in-house. The unencapsulated devices were held in laboratory ambient while being illuminated by a sulfur plasma lamp (color temperature ~5300 K) with overall intensity adjusted to 80%–85% of 1-sun. The testing followed ISOS-L-1 protocols as defined by the consensus stability testing protocols for PV devices [106]. Each cell was covered by a metal mask allowing only 0.061 cm^2 of illumination area in order to eliminate stray current edge effects.

Several silicon photodiodes with KG5 filters were used to monitor the light intensity at various points on the sample holder platform. Custom-built electronics were used to measure the current-voltage (*I-V*) responses of the cell at periodic time intervals. Between *I-V* measurements, the devices were held at a static load of 510 Ω. Samples were cooled by a liquid chiller set to 25 °C, with the device surface measuring ~30 °C. *I-V* curves were measured from +1.3 V to -0.2 V in 0.02 V steps. *I-V* curves were measured every 60 min to monitor the solar cell performance over time. The relative humidity during device operation was recorded by an EXTECH Instruments RH520A humidity and temperature recorder.

2.4 RESULTS AND DISCUSSION

Earlier work by Ono *et al.* [53] and Yang *et al.* [30] showed that the hole-transporting layers (HTLs), such as Spiro-OMeTAD, can mitigate decomposition of an underlying $MAPbI_3$ film; however, poor continuity in the HTL allows the ingress of moisture and the egress of volatile decomposition products. Thus, we hypothesized that evaporating a thin layer of MoO_x could effectively fill pinholes in the Spiro-OMeTAD film and reduce moisture ingress to the $MAPbI_3$ film and reduce moisture ingress to the $MAPbI_3$ film. We performed XPS studies on $MAPbI_3$/Spiro-OMeTAD films with and without a MoO_x layer on top to compare the coverage and conformity of the Spiro-OMeTAD and MoO_x films on the $MAPbI_3$ layer. In the XPS spectra shown in **Figure 2.3**, we see the presence of the I 3d and Pb 4f core levels, respectively, on the surface of $MAPbI_3$/Spiro-OMeTAD films without MoO_x, in contrast to the absence of these I 3d and Pb 4f signals on the surface of devices with a MoO_x layer on top. The presence of Pb and I signals is consistent with reports in the literature that indicate pinhole formation in the ~100 nm thick Spiro-OMeTAD layer [53]. It has been suggested that these pinholes provide a path for

moisture and oxygen ingress to degrade the absorber [53]. By filling in pinholes in the Spiro-OMeTAD layer, it is likely that the MoO_x interlayer can suppress degradation of the $MAPbI_3$ layer.

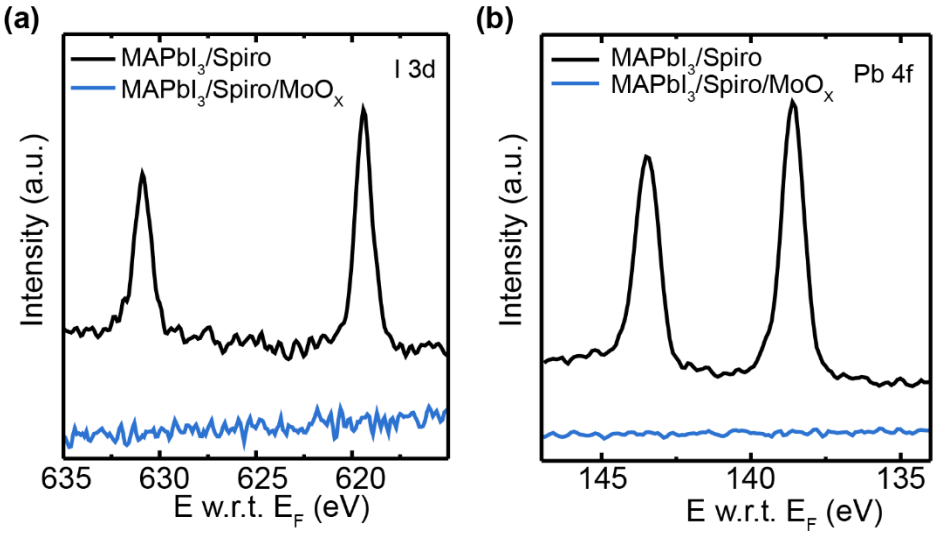

Figure 2.3. XPS characterization of $MAPbI_3$ films without and without MoO_x. XPS core level spectra of **(a)** I 3d and **(b)** Pb 4f regions of $MAPbI_3$/Spiro-OMeTAD films on TiO_2 with (in blue) and without (in black) a MoO_x layer. The emergence of features in the glass/TiO_2/$MAPbI_3$/Spiro-OMeTAD case is consistent with pinhole formation in the spiro-OMeTAD layer. The 15 nm thick MoO_x layer on top obscures any evidence of iodine or lead, which is consistent with the concept of sealing of these pinholes.

To determine the effect of the MoO_x interlayer on the degradation of $MAPbI_3$ films, we monitored the absorptance of $MAPbI_3$ films with prolonged light exposure in ambient laboratory conditions. We compared the absorption of (i) $MAPbI_3$, (ii) $MAPbI_3$/Spiro-OMeTAD, and (iii) $MAPbI_3$/Spiro-OMeTAD/MoO_x film stacks on glass/TiO_2 substrates. The films were illuminated by an Eiko Solux tungsten-halogen light source set to a light intensity equivalent to 1-sun flux in laboratory ambient conditions. As seen in **Figure 2.4**, after 115 h of illumination, the absorption spectra of the $MAPbI_3$ and $MAPbI_3$/Spiro-OMeTAD films without MoO_x exhibited significant absorption losses in the spectral region between 500 and 800 nm, which indicates degradation of the $MAPbI_3$ film. The degraded $MAPbI_3$ and $MAPbI_3$/Spiro-OMeTAD absorption spectra

resemble the absorption spectrum of PbI_2, which has an absorption onset at about 520 nm. In contrast, most of the absorption of the $MAPbI_3$/Spiro-OMeTAD/MoO_x film was retained except for slight reduction in the absorption throughout the 650–800 nm wavelength regime. This reduction in absorption was significantly less than the $MAPbI_3$ and $MAPbI_3$/Spiro-OMeTAD films in the same wavelength region and occurred after a much greater duration of light exposure (not shown here) indicating an enhanced stability from the MoO_x layer. Furthermore, we did not observe any absorption losses in films stored under dark conditions for 115 h (**Figure A.2**), which indicates that illumination played a critical role in the degradation of these $MAPbI_3$ films.

To quantify the loss in the absorption over time, the spectral absorptance was integrated with the AM1.5G solar spectrum to calculate the number of solar photons that would be absorbed by each film after light exposure. We then normalized this number of solar photons absorbed by the light-exposed film relative to the initial, pristine film, which is provided in **Figure 2.4**. This ratio of absorption by the light-exposed film relative to the pristine film declines rapidly after a mere 1.5 h of light exposure and then plateaus at roughly 40% for the $MAPbI_3$ film. Adding a Spiro-OMeTAD film on the $MAPbI_3$ film retards this reduction in absorptance until 10 h of light exposure, after which the absorptance deteriorates to the same 40% of initial absorptance as the $MAPbI_3$ film. More importantly, when a thin (15 nm) MoO_x layer is deposited on the $MAPbI_3$/Spiro-OMeTAD stack, 94% of the initial absorptance is retained after 115 h of illumination. These results indicate that the MoO_x mitigates photo-induced decomposition of the $MAPbI_3$ film.

We can also see these trends in the optical images of the films in **Figure 2.4**. The initially dark brown $MAPbI_3$ film turned yellow after 3 h of light exposure and remained yellow with continued light exposure, which corresponds with the plateau in the absorption loss. The

$MAPbI_3$/Spiro-OMeTAD films also turned yellow after 115 h, whereas the $MAPbI_3$/Spiro-OMeTAD/MoO_x film only lightened slightly after 115 h of illumination, which corresponds with the slight absorption loss in the 650–800 nm regime in Fig. 2C. The observed transformation of the dark brown $MAPbI_3$ film to the resultant yellow film is consistent with previous reports of $MAPbI_3$ degradation to PbI_2 [18], [33], [37]. X-ray diffraction (XRD) patterns of the samples after 115 h of illumination (**Figure A.3**) is consistent with the decomposition of $MAPbI_3$ to PbI_2. The $MAPbI_3$/Spiro-OMeTAD stack and $MAPbI_3$ film did not reveal any clear diffraction peaks after degradation and appeared significantly more disordered. We suggest this is due to further decomposition of the PbI_2 under continued exposure to illumination and ambient oxygen and moisture.

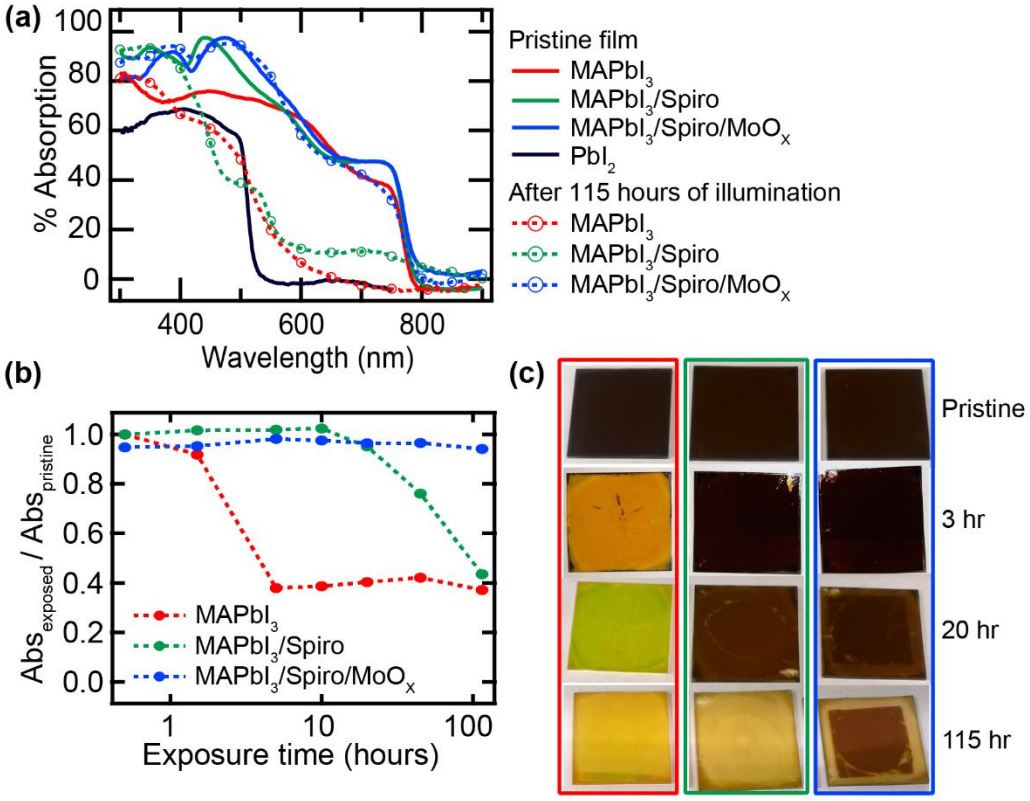

Figure 2.4. Absorptance of films under illumination in laboratory ambient. **(a)** Absorption spectra of bare $MAPbI_3$ (red), $MAPbI_3$/Spiro-OMeTAD (green), and $MAPbI_3$/Spiro-OMeTAD/MoO_x (blue) films on glass/TiO_2 before and after 115 h of illumination. Degradation was induced by constant illumination from a tungsten-halogen light source in ambient conditions. The absorption spectrum of PbI_2 (black) is also provided. **(b)** The ratio of absorption by the exposed film relative to the pristine film over light exposure time. The absorption was quantified by integrating the absorption spectrum of the film with the AM 1.5 solar spectrum. **(c)** Optical images of the films with increasing light exposure show the decomposition of $MAPbI_3$ film from brown to yellow with increasing light exposure. The films pictured here were deposited on 1 in x 1 in glass slides. Since the MoO_x layer was deposited through a shadow mask, the edges of the $MAPbI_3$/Spiro-OMeTAD/MoO_x sample are bleached where the MoO_x is absent, but the protected center remained optically dark.

To support the hypothesis of moisture and/or oxygen ingress being deleterious to device performance and determine whether a thin MoO_x layer can serve as an effective moisture barrier, we examine three sets of devices with MoO_x/Al electrodes degraded with different ambient humidity due to seasonal variations in our lab. As expected, we find increasing levels of relative humidity (RH) to accelerate degradation rates. Several devices with the same device configuration

were fabricated and tested in low, medium, and high RH conditions with humidity ranges of 16±4%, 33±9%, and 51.5±1.5%, respectively. The normalized efficiency of representative devices and the recorded humidity data are provided in **Figure 2.5**. The device tested in high RH had degraded to roughly 61% of the initial efficiency after 24 h of operation, whereas the devices in the medium and low RH conditions were still at 90% and 99%, respectively, of the initial efficiency after the first 24 h of operation. After 50 h of operation, the devices in medium and low RH conditions had maintained roughly 71% and 91%, respectively, of the initial device efficiency, which further corroborates the moisture sensitivity of the $MAPbI_3$ films and devices previously reported [30], [40]. Although a 15 nm layer of MoO_x may be retarding the level of moisture/oxygen ingress, there is still a clear sensitivity to humidity.

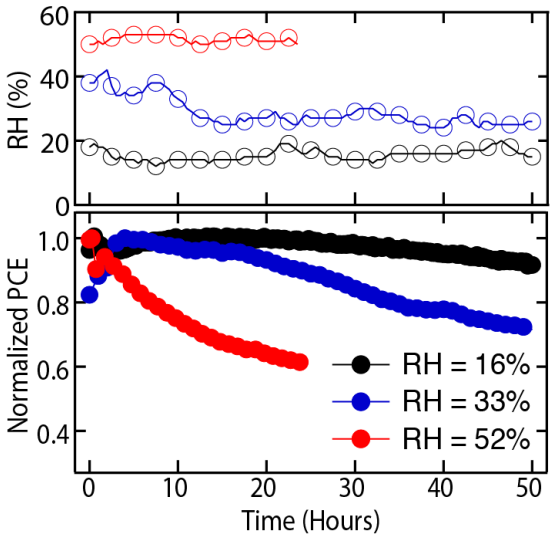

Figure 2.5. Effect of relative humidity (RH) on degradation. The normalized power conversion efficiency of similarly fabricated cells measured in three different RH conditions. All of the devices had the same electrode configuration of 15 nm of MoO_x/200 nm of Al.

To explore the possibility of improving the barrier properties of the MoO_x interlayer, we varied the MoO_x interlayer thickness and fabricated devices with MoO_x thicknesses of 8 nm, 15 nm, 50 nm, 100 nm and 200 nm. The initial measurement of the devices yielded average device

efficiencies ranging from 9.2%–9.8%, as seen in **Figure 2.6**. Among the devices selected for stability testing, the initial device performance did not have a strong thickness dependence, which is unlike the study by Zhao *et al.* that found a decrease in PCE with MoO_x thicknesses exceeding 10 nm [93]. We did, however, observe a lower yield in measureable devices for the 8 nm MoO_x case (**Figure A.4**) indicating that 8 nm may not provide complete coverage.

After the initial measurement, the devices with varying MoO_x interlayer thicknesses were operated in laboratory ambient for 150 h. As the stability testing setup used a sulfur plasma light source, *J-V* scans under an AM1.5G solar simulator were acquired before and after the laboratory weathering. Despite having comparable initial efficiencies across the varying MoO_x thicknesses, devices with thicker MoO_x interlayers had lower PCEs after constant operation for 150 h in ambient, as seen by the open squares in **Figure 2.6(b)**. In this case, the inverse correlation between MoO_x thickness and device lifetime is more apparent from the measurements taken in ambient during constant operation, as seen in **Figure 2.6(c)**. This is due to the rapid decline in device performance in the first 25 h for the 50 nm MoO_x devices, which cannot be observed by the single post-degradation measurement in **Figure 2.6(b)**.

From visual inspection of the degraded devices, we observe corrosion under the metal electrodes for the thinner 8 nm and 15 nm MoO_x devices, but not for the devices with thicker MoO_x interlayers. Thus, the thicker MoO_x interlayers help prevent corrosion under the Al electrodes, but this corrosion is not the primary cause of device failure as it occurs outside of the active device area. Instead, we see faster degradation in device performance with the thicker MoO_x layers, but without many visual indicators for this decrease in stability. The degradation in performance also corresponds with a rapid increase in series resistance during the continuous operation of the devices with thicker MoO_x interlayers (not shown here). This inverse correlation between the

MoO_x thickness and the device lifetime is consistent with an interfacial effect between the MoO_x and Al or spiro-OMeTAD layers, a bulk compositional change to the MoO_x, or some combination of these rather than the MoO_x interlayer acting as a moisture/oxygen barrier. More specifically, mechanisms for this reduction in durability with increasing MoO_x interlayer thickness may include the following: First, the increased MoO_x interlayer thickness may lead to an increase in delamination due to an increase in strain. Second, a larger MoO_x interlayer may correspond to greater, electrically-driven Al_2O_3 formation at the MoO_x/Al interface. Third, the MoO_x layer may undergo compositional changes either with the relative oxygen content or through interaction with outward diffused Pb and/or I. Changes to the oxidation state have been shown to vary the work function [107], resistivity [108], and gap state density [109] of MoO_3. Each of these potential mechanisms is consistent with the reduced charge extraction observed with time. Currently, further studies are required to determine the root cause of the inverse MoO_x thickness dependence on the device stability.

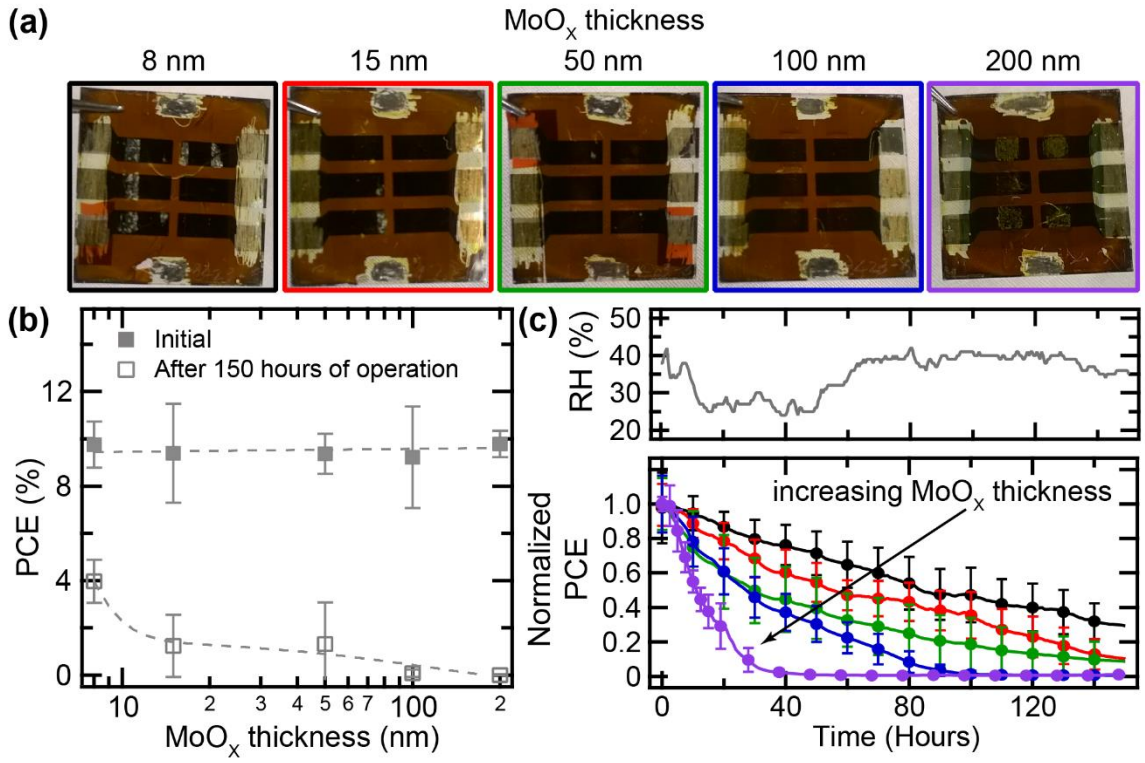

Figure 2.6. Effect of MoO_x thickness on degradation of perovskite solar cells. **(a)** Optical images of the devices with MoO_x/Al electrodes with varying thicknesses of MoO_x after 150 h of constant operation. The devices pictured here were fabricated on 1 in x 1 in glass substrates. **(b)** The efficiency of devices before (closed squared) and after 150 h of constant operation (open squares) measured in a N_2-filled glovebox. **(c)** The relative humidity and normalized efficiency of devices measured during the 150 h of operation. The normalized average efficiency of devices with MoO_x thicknesses of 8 nm, 15 nm, 50 nm, 100 nm, and 200 nm are shown in black, red, green, blue, and purple, respectively. Error bars shown represent one standard deviation of the measured cells.

We compared devices where the back electrode is Au, Ag, or Al either with or without a MoO_x interlayer, thus producing six electrode combinations. In the devices containing MoO_x, a thin layer of 15 nm was introduced between the Spiro-OMeTAD HTL and the back metal electrode as shown in **Figure 2.1**. With the exception of the Al-only electrode, the initial performance of devices with these different electrode configurations were comparable, as seen in the current density-voltage (*J-V)* characteristics in **Figure 2.7(a)**. The median PCE of the devices varied from 9.2% to 10.2%, with the lowest-performing devices having a MoO_x/Al electrode and the highest-

performing devices having a Au electrode, as seen in **Figure 2.7(c)** (black box plots). Devices with Al-only electrodes resulted in efficiencies of <0.1%, which is consistent with previous work by Zhao *et al*.[93] In the case of Au and Ag, the MoO_x interlayer was not necessary to yield working devices and did not affect the initial performance significantly.

After 24 h of constant operation in laboratory ambient, the MoO_x/Al electrodes, not commonly used in perovskite solar cells, retained the highest PCE of initially comparable devices. Devices with Au and MoO_x/Au electrodes show the second- and third-highest PCEs after 24 h, respectively. The relative humidity of the laboratory averaged 51.5±1.5% during this test period. Similar to the previous stability tests, *J-V* measurements were acquired with an AM1.5G solar simulator before and after weathering. The *J-V* curves of champion cells are shown in **Figure 2.7(b)** and the efficiencies are shown in the red box plots in **Figure 2.7(c)**. In the case of MoO_x/Al electrodes, the enhanced stability can be attributed to greater preservation of the short-circuit current density (*Jsc*), whereas a more stable open-circuit voltage (*Voc*) and fill factor (*FF*) are responsible for the relatively high performance of the Au devices. Although Ag is often used in $MAPbI_3$ solar cells, we note that neither the Ag nor the MoO_x/Ag devices survived the degradation run, with average PCEs below 0.1% after 24 h of constant operation. This result is consistent with other reports of poor stability and corrosion of Ag electrodes in perovskite devices.[40], [45]

A comparison of the *Jsc* of the degraded devices in **Figure 2.7(f)** reveals that devices with the MoO_x interlayer had higher *Jsc* than devices without MoO_x for all three metals used in this study. External quantum efficiency (EQE) spectra in **Figure 2.7(e)** provides greater insight on the relative improvements observed by adding a MoO_x interlayer. First, we see that the devices with Au or Ag electrodes without MoO_x have significant EQE losses in the longer wavelength regime. This is similar to the absorption spectrum of the degraded $MAPbI_3$ films shown in **Figure 2.4**, and is

consistent with a reduction in charge generation due to decomposition of the perovskite active layer. In the case of Au, adding a MoO_x interlayer resulted in a slight improvement in the EQE relative to the Au-only devices, but overall, the MoO_x/Au devices still suffered a significant loss in the longer wavelength regime relative to the pre-degraded device. Comparing the Ag and MoO_x/Ag devices, we see that the additional MoO_x interlayer preserves significantly more of the EQE in the longer wavelength regime. The EQE of the degraded MoO_x/Al device shows the greatest preservation in shape relative to a pre-degraded device, and the highest EQE overall. Thus, we see that the enhanced stability in the MoO_x-containing devices are affected by the choice of the metal electrode. Although the choice in metal electrode did not affect the initial performance, we see that electrode choice has a significant effect on the device degradation.

To gain insight into the increased stability of MoO_x/Al devices as compared to MoO_x/Au and MoO_x/Ag devices, we conducted XPS studies on thin, 5 nm metal films (Au, Ag, and Al) on bare ITO and on ITO/MoO_x substrates. In these studies, we can see that Au and Ag do not react with the MoO_x surface (**Figure A.6**). The Al, however, does react with the underlying MoO_x film, which results in the formation of metallic Mo and MoO_2, as seen from the appearance of Mo^0 and Mo^{4+} components, respectively. We speculate that due to the relative formation enthalpy of Al_2O_3 (Δ_fH = -1669.8 kJ/mol) compared to MoO_3 (Δ_fH = -745.17 kJ/mol),[110] we may be forming Al_2O_3, or other non-stoichiometric aluminum oxides, at the MoO_x/Al interface. Previous studies have suggested that Al_2O_3 interlayers improve device stability by serving as a physical barrier to moisture.[29], [43] While this remains a possibility, it seems peculiar that a thin alumina layer would impart so much better of a barrier than the thick metal layers. It also doesn't fully explain the observed differences in the EQE spectra of **Figure 2.7(e)**.

Visual inspection of the degraded devices reveals some further insight. As seen in **Figure 2.7(d)**, photographs of the devices without a MoO_x interlayer exhibit photobleaching in areas below or near the metal electrode after 24 h of operation in ambient. This photobleaching of the dark brown $MAPbI_3$ layer yielded a yellow film similar to the degraded $MAPbI_3$ films seen in **Figure 2.7(e)**, and indicates decomposition of the $MAPbI_3$ layer. Using Ag or Al without MoO_x results in the most photobleaching, whereas Au electrodes without MoO_x result in some, but significantly less, photobleaching. This is consistent with Au, a noble metal, being significantly less reactive with the perovskite active layer than both Al and Ag. It also suggests that the MoO_x interlayer mitigates this reaction.

Visual indications of corrosion of the metal electrode are present in both the Al and the MoO_x/Al case. More specifically, we observe areas of transparency beneath the Al and MoO_x/Al electrodes. This occurs next to the FTO pad, but not in device's active area. This indicates that a different degradation mechanism may occur when an Al contact is used. The presence of the transparent areas beneath the Al electrodes, instead of either brown (indicating $MAPbI_3$) or yellow (indicating PbI_2) areas, suggests that the formation of PbI_2 is either inhibited or decomposed further due to the presence of Al. In the case of the MoO_x/Al devices, the active areas were not affected appreciably and were still operable.

Taking these different pieces together, we propose a potential mechanism. First we review the relevant observations. Devices with Au electrodes appear to degrade in a manner similar to the non-contacted samples in **Figure 2.4**. Introducing a thin MoO_x layer to a device with Au electrodes has only a mild effect in reducing the degradation of the perovskite active layer. However, the presence of a reactive metal such as Ag or Al without a protective interlayer accelerates the active layer decomposition. Inserting a MoO_x interlayer significantly slows the active layer

decomposition when Ag or Al is used, even relative to the Au case (**Figure 2.7**). Increasing the thickness of the MoO_x layer accelerates degradation, suggesting that MoO_x is not primarily serving as a moisture barrier layer. Depositing Al or Ag on a thin oxide layer can lead to an interfacial oxide that would not form when deposited on spiro-OMeTAD. Al in particular not only has an oxide with a high tendency to form, but is also a strongly passivating oxide as a result of its Pilling-Bedworth ratio (ratio of volume of elemental cells of the oxide to metal). Devices with MoO_x/Au contacts compared to Au-only experience little alteration in the EQE spectrum as a result of degradation. In contrast, Ag and Al based devices see a dramatic change in their spectral response compared to their counterparts with MoO_x, which suggests that the MoO_x benefit is related to the formation of a protective oxide. The fact that increased MoO_x thickness is detrimental to stability further supports that the role of the MoO_x is connected to interfacial stability. Changing series resistance of the MoOx thickness series suggests that MoO_x may have its composition evolve with time. Very thin layers may serve to pin the workfunction at the spiro-OMeTAD interface while nucleating a stable oxide at the metal interface. The self-passivating nature of aluminum oxide explains the increased stability of MoO_x/Al over MoO_x/Ag. The introduction of Al (or Ag) oxide then leads to the slowing of iodization of the back contact. This work directly addresses the previously identified need to minimize iodization in Ag back contacts, while preserving initial efficiency and without requiring a significantly altered device architecture.

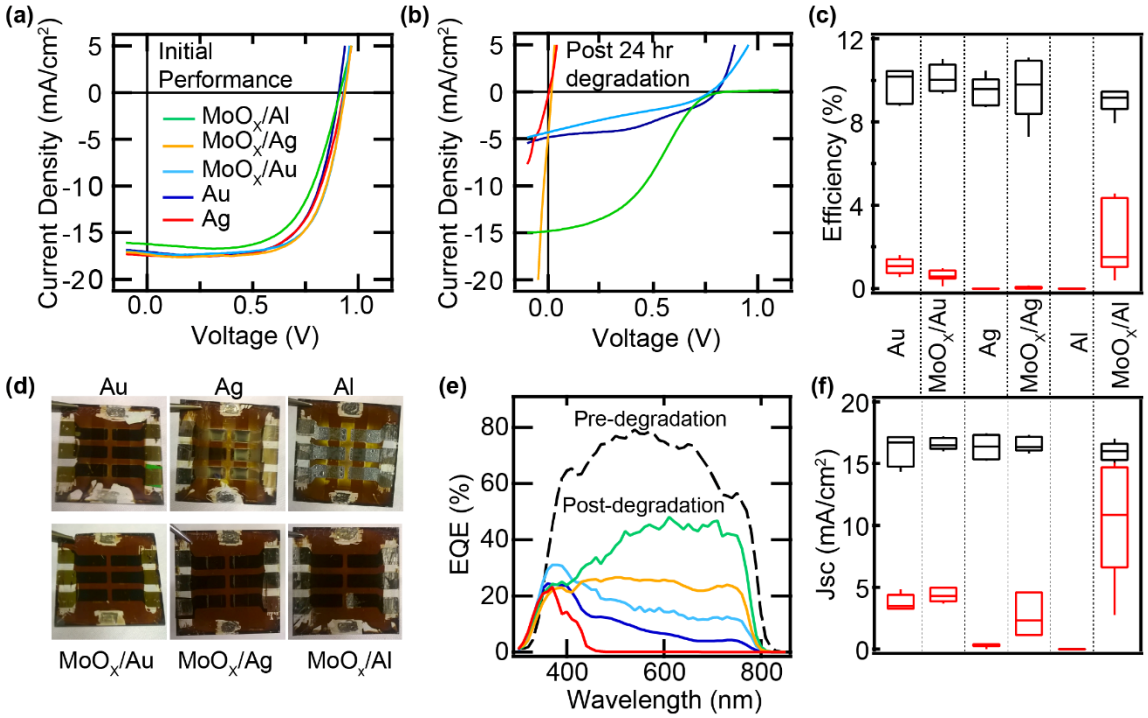

Figure 2.7. Effect of electrode selection on initial efficiency and lifetime of perovskite solar cells. The current density-voltage characteristics of representative devices with Au (dark blue), Ag (red), MoO_x/Au (light blue), MoO_x/Ag (orange), or MoO_x/Al (light green) electrodes **(a)** before and **(b)** after 24 h of constant operation in ambient. The MoO_x interlayers had a thickness of 15 nm. **(c)** Box plots of the efficiency before (black) and after (red) degradation. **(d)** Optical images taken from the glass side of the device show visual signs of $MAPbI_3$ decomposition for devices without the MoO_x interlayer. The devices pictured here were fabricated on 1 in x 1 in glass substrates. **(e)** External quantum efficiency of the devices after 24 h of constant operation. The EQE spectra of a typical as-prepared device is also shown in black. **(f)** Box plots of the short-circuit current density show that the relative post-degradation short-circuit current corresponds with the area under the EQE spectra.

In addition to studying the ambient operational stability of devices, we also wanted to gain some insight on the stability improvements we can expect with encapsulation. Commercial solar panels utilize encapsulation to prevent the ingress of ambient moisture and oxygen, as well as providing additional mechanical durability, to increase solar panel lifetime. To anticipate the role of encapsulation for $MAPbI_3$ perovskite solar cells, we conducted preliminary operational stability tests with a thin, 26 nm layer of Al_2O_3 encapsulant layer deposited via atomic layer deposition. Although this thin alumina layer is considered a leaky encapsulant due to discontinuities and

imperfections in the film, it will still provide some insight into the role of ambient oxygen and moisture on the relative rate of degradation. $MAPbI_3$ solar cells were fabricated with electrodes consisting of 200 nm of MoO_x and 200 nm of Al and then tested using the same stability testing procedures described above. The normalized efficiencies, as shown in **Figure 2.8**, indicate that the alumina encapsulation dramatically increased the stability of the $MAPbI_3$ solar cells. The T80, a term for the number of hours before the device efficiency decreases to 80% of its initial efficiency, of the devices increased from 5 h without the encapsulant up to 337 h with the encapsulant. This 67-fold increase emphasizes the role ambient moisture and oxygen play in hastening the degradation of the perovskite solar cells.

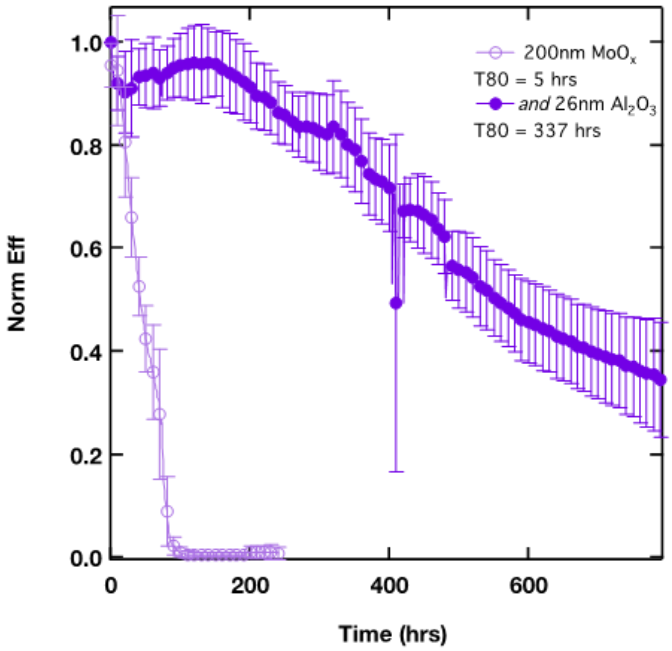

Figure 2.8. Effect of thin alumina encapsulant on operational lifetime of $MAPbI_3$ solar cells. Normalized efficiency of $MAPbI_3$ solar cells with (filled circles) and without (open circles) 26 nm layer of alumina coating around the device shows the significant improvement in stability with an unoptimized encapsulant layer. The error bars indicate the standard deviation of the measured devices.

2.5 CONCLUSION AND OUTLOOK

In conclusion, we demonstrated that electrode selection for $MAPbI_3$ devices have a profound effect on the device stability despite having comparable initial efficiencies. Specifically, MoO_x/Al electrodes yielded the most stable solar cells. Furthermore, while we find that MoO_x thickness has little impact on the initial efficiency, thinner MoO_x interlayers yield more durable devices. These results are consistent with enhanced stability due to an interfacial effect with the MoO_x. The absorption spectra and XRD patterns of illuminated $MAPbI_3$ films indicate that a thin MoO_x layer prevents photobleaching of the $MAPbI_3$ film and mitigates decomposition. In conjunction with these $MAPbI_3$ film studies, we also see a lack of photobleaching in devices with MoO_x interlayers. However, the device stability studies indicate that the presence of a MoO_x interlayer alone is not responsible for alterations to device stability; instead, the specific MoO_x/metal combination plays a critical role. These results suggest that in addition to design rules for maximizing initial efficiency such as tailoring the workfunction for optimal charge extraction, the evolution of these interfaces may provide a key to understanding the long-term performance of perovskite solar cells. While this work focused on the effects of the back contact on stability for the most commonly used perovskite absorber composition, it is a template and baseline for addressing stability in perovskite solar cells employing alternate absorber compositions or front contacts.

Stability remains a critical area of research for perovskite solar cells. Several studies have demonstrated the necessity for careful electrode selection, as well as more robust HTLs and ETLs. In addition to long term operational studies, more rigorous studies of at elevated temperatures and elevated humidity is necessary to prove that this relatively new technology can transition to real world applications. As highlighted in this work, understanding the durability of each layer and the interfaces between layers is of particular importance. In addition to improving individual layers

within the device stack, the moisture sensitivity of the devices are particularly troubling. Although commercial solar panels rely on glass-glass encapsulation, edge seals can fail, which would lead to catastrophic failure in these $MAPbI_3$ perovskite solar cells. Thus, developing more robust perovskite active layer chemistries, or more hydrophobic protective layers (either active or passive) is another potential area for further research.

In addition to research on the stability of completed $MAPbI_3$ perovskite solar cells, studies on the degradation of neat films are also invaluable. In a publication that I co-authored entitled "Structural and chemical evolution of methylammonium lead halide perovskites during thermal processing from solution," we showed that the processing window required to remove residual solvent and precursor phases overlaps with decomposition of volatile products, which highlights the sensitivity of $MAPbI_3$ to thermal decomposition [111]. Other studies conducted on the thermal stability of $MAPbI_3$ films show evidence of degradation in inert environments at 85°C [31], which is well within possible operating temperatures of solar panels. Thus, we explored alternative perovskite active layer chemistries to replace the relatively fragile methylammonium cation with a more thermally stable alternative. In the following chapters, I will discuss our work using all inorganic $CsPbI_3$ perovskite QDs. Not only is $CsPbI_3$ compositionally stable up to its melting point (>400 °C), but the nanocrystal synthesis decouples crystallization from deposition which removes thermal processing challenges seen with $MAPbI_3$ film formation.

Chapter 3. QUANTUM DOT-INDUCED PHASE STABILIZATION OF α-$CsPbI_3$ PEROVSKITE FOR HIGH-EFFICIENCY PHOTOVOLTAICS

Adapted with permission from:
Swarnkar, A.; Marshall, A. R.; Sanehira, E. M.; Chernomordik, B. D.; Moore, D. T.; Christians, J. A.; Chakrabarti, T; Luther, J. M. Quantum dot-induced phase stabilization of α-$CsPbI_3$ perovskite for high-efficiency photovoltaics. *Science*, **2016**, *354* (6308), pp 92-95.

3.1 ABSTRACT

We employ nanoscale phase stabilization of $CsPbI_3$ quantum dots (QDs) to low temperatures, to utilize $CsPbI_3$ perovskite as the active component of efficient optoelectronic devices. $CsPbI_3$ is an all-inorganic analogue to the hybrid organic cation halide perovskites. However, the cubic phase of bulk $CsPbI_3$ (α-$CsPbI_3$, the variant with desirable bandgap) is only stable at high temperature, preventing its adoption within the community. We describe formation of α-$CsPbI_3$ QD films, phase stable for months in ambient air, with long-range electronic transport, leading to the fabrication of the first colloidal perovskite QD solar cells with an open-circuit voltage of 1.23 V and efficiency of 10.77 %. These devices also function as light emitting diodes (LEDs) with low turn-on voltage and tunable emission. The synthesis of normally unstable material phases stabilized through colloidal QD synthesis provides another mechanism for materials design for photovoltaics, LEDs, and other applications.

3.2 INTRODUCTION

Hybrid organic-inorganic halide perovskites, with the common formulation ABX_3 (where A is an organic cation, B is commonly Pb^{2+}, and X is a halide), were first applied to PVs as $MAPbI_3$ in

2009 [13]. After only seven years of research, perovskite PV devices processed from solution inks now convert >22% of incident sunlight into electricity, on par with the best thin film chalcogenide and silicon devices. The major technical hurdle in the commercialization of this technology lies in the durability of the semiconductor. Under environmental stress, $MAPbI_3$ dissociates into PbI_2 and CH_3NH_3I, the latter of which is volatile [111]. An all-inorganic structure without a volatile organic component is highly desired.

The all-inorganic Pb-halide perovskite with the most appropriate bandgap for PV is cubic (α) $CsPbI_3$ (E_g=1.73 eV) because geometrical constraints of the perovskite crystal structure require a large +1 A-site cation and Cs^+ is the most feasible. However, below 320 °C, the orthorhombic (δ) phase (E_g=2.82 eV) is thermodynamically preferred [112]. Nevertheless, groups have explored $CsPbX_3$ compounds as PV materials, but films of α-$CsPbI_3$ undergo immediate transformation to the orthorhombic phase when exposed to ambient conditions [59]. Attempts to stabilize the cubic phase through alloying with Br^-, $CsPbIBr_2$ shows a much reduced δ to α phase transition temperature of 100 °C [112], however it also leads to an undesired increase in the bandgap. Here, we show that nanocrystal surfaces can be utilized to stabilize α-$CsPbI_3$ at room temperature, far below the phase transition temperature for thin film or bulk materials. We further show that we can fabricate the electronically-coupled quantum dot (QD) arrays to produce air-stable, efficient solar cells (initial efficiency above 10%) based on this all-inorganic material.

Many physical properties differ between nanometer-sized and bulk crystalline materials of the same chemical compound. One such example is the structural phase in which the constituent atoms are arranged. For example, the semiconductors CdS and CdSe embody a rock salt structure at high pressure. However, the solid-solid phase transition point between the rock salt phase and the hexagonal wurtzite phase can vary greatly in temperature and pressure as a function of crystal

size [113], [114]. Manipulated size-dependent phase diagrams have been explored in a variety of material systems with advantageous properties of the crystals emerging at reduced dimensions in oxides (*e.g.*, TiO_2), lanthanides (*e.g.*, $NaYF_4$) [115], metals (*e.g.*, Ag) [116], and ferroelectrics (*e.g.*, the perovskite $BaTiO_3$) [117].

Synthetic protocols of colloidal halide perovskite QDs have recently been reported [60], [118]–[124]. $CsPbX_3$ QDs exhibit improved room temperature cubic phase stability and attractive optical properties for a wide range of applications [60], [125]–[129]. Experiments on size and shape dependent optical properties [60], [130]–[132], surface chemistry [133], and other photophysics [134] are being explored for $CsPbBr_3$ QDs. However, previous studies were unable to achieve cubic $CsPbI_3$ QDs that were stable enough to extensively characterize, let alone to fabricate optoelectronic devices. In this Chapter, I detail the novel purification and film deposition methods that enabled the first demonstration of a $CsPbI_3$ QD solar cell and the most efficient all-inorganic $CsPbX_3$ perovskite solar cell at the time of publication.

3.3 METHODS

3.3.1 *Quantum dot and materials synthesis*

Chemicals. All chemicals were purchased from Sigma Aldrich and used without purification, unless otherwise noted. Cesium carbonate (Cs_2CO_3, 99.9%), lead (II) iodide (PbI_2 99.9985%, Alfa Aesar), oleic acid (OA, technical grade 90%), oleylamine (OAm, technical grade 70%), 1-octadecene (ODE, technical grade 90%), toluene (anhydrous 99.8%), hexane (reagent grade ≥95%), octane (anhydrous, ≥99%), 1-butanol (anhydrous 99.8%), methyl acetate (MeOAc, anhydrous 99.5%), lead (II) acetate trihydrate (Pb(OAc)2·3H2O, 99.999%), lead (II) nitrate ($Pb(NO_3)_2$, 99.999%), rhodamine-6G (99%), ethanol (EtOH, 200 proof, ≥99.5%), titanium

ethoxide (≥97%), hydrochloric acid (HCl, 37% in water), 2,2′,7,7′-Tetrakis(N,N-di-p-methoxyphenylamine)-9,9′-spirobifluorene (spiro-OMeTAD, Lumtec, ≥99.5%), chlorobenzene (anhydrous, 99.8%), 4-tert-butylpyridine (4-TBP), bis(trifluoromethane)sulfonimide lithium salt (Li-TFSI), and acetonitrile (anhydrous, 99.8%).

Synthesis of Cs-oleate as a cesium precursor. 0.5 g of Cs_2CO_3, 2 mL OA and 50 mL ODE were added to a 100 mL 3-necked round bottom flask and stirred under vacuum for 30 min at 120 °C. The flask was purged with N_2 for 10 min and then placed back under vacuum. This process of alternately applying vacuum and N_2 was repeated 3 times to remove moisture and O_2. The reaction was considered complete when the solution was clear, indicating that the Cs_2CO_3 had reacted with the OA. The Cs-oleate solution in ODE was stored in N_2 until it was needed for the QD synthesis.

Synthesis of colloidal $CsPbI_3$ QDs. $CsPbI_3$ QDs were synthesized following the previous report by Protesescu, *et al.* [60] with some modification. The synthesis was scaled up by 10 times to have sufficient product for device fabrication. Various sizes of colloidal $CsPbI_3$ QDs were synthesized by tuning the reaction temperature. PbI_2 (1 g) and ODE (50 mL) were stirred in a 500 mL round bottom flask and degassed under vacuum (~0.1 Torr) at 120 °C for 1 hour. The flask was then filled with N_2 and kept under constant N_2 flow. OA and OAm (5 mL each, pre-heated at ~70 °C) were injected. The flask was put under vacuum again until the PbI_2 completely dissolved and the solution and bubbling from the reaction stopped (15 – 30 min). The temperature was then varied depending on the desired QD size (60 °C for 3.4 nm, 100 °C for 4.5 nm, 130 °C for 5 nm, 150 °C for 6.8 nm, 170 °C for 8 nm, 180 °C for 9 nm, and 185 °C for 12.5 nm QDs). The Cs-oleate (~0.0625 M, 8 mL) precursor, pre-heated to 70 °C under N_2 atmosphere, was swiftly injected into the reaction mixture. The reaction mixture turned dark red and the reaction was quenched by immediate immersion of the flask into an ice bath (~5 s after injection).

Isolation of colloidal $CsPbI_3$ QDs. Due to the ionic nature of the $CsPbI_3$ QDs and the proposed ionic binding of the ligands, polar anti-solvents traditionally used to wash QDs from reaction solutions instead cause a reversion to the orthorhombic phase due to agglomeration or simply redissolve the $CsPbI_3$ QDs. A variety of low polarity non-solvents were tested: 1-butanol, acetone, and ethyl acetate destabilized the QDs and resulted in a pale yellow suspension, while MeOAc successfully extracted cubic phase $CsPbI_3$ QDs. The synthesized $CsPbI_3$ QDs were precipitated by adding 200 mL MeOAc (ratio of QD reaction solution:MeOAc is 1:3) and then centrifuged at 8000 RPM for 5 min. The wet pellet of QDs in each centrifuge tube was redispersed in 3 mL hexane, precipitated again with an equal volume MeOAc and centrifuged at 8000 RPM for 2 min. *Note: Adding excess MeOAc removes the surface ligands, causing the QDs to agglomerate and revert to the orthorhombic phase.* The QDs were dispersed in 20 mL of hexane and centrifuged again at 4000 RPM for 5 min to remove excess PbI_2 and Cs-oleate. The solution of colloidal $CsPbI_3$ QDs was kept in the dark at 4 °C for 48 hours to precipitate excess Cs-oleate and Pb-oleate, which solidify at low temperatures. The QD solution was decanted and centrifuged again at 4000 RPM for 5 min before use. For device fabrication, the hexane was dried and the QDs were dissolved in octane at a concentration of ~50 mg/mL. The temperature range of the synthesis is determined by the solubility of the precursors; Cs-oleate is insoluble in ODE below 60 °C and PbI_2 begins to precipitate out of the reaction solution above 185 °C.

3.3.2 *QD Film and Device Fabrication*

Fabrication of QD arrays. Ligand solutions were made by sonicating 10-20 mg of lead salt (either $Pb(OAc)_2$ or $Pb(NO_3)_2$) in 20 mL of anhydrous MeOAc for 10 min. Excess salt was removed by centrifugation at 4000 RPM for 5 min. The QDs (~50 mg/mL in octane) were spin-cast on the substrate at 1000 RPM for 20 s followed by 2000 RPM for 5 s, and then swiftly dipped

2-3 times in the ligand solution. The film was rinsed via dipping in neat, anhydrous MeOAc, then dried with a stream of air. Films grown using only MeOAc (*i.e.*, no ligand treatment) were treated with only a single rinsing step. This procedure was repeated multiple (3-5) times to build up 100 – 500 nm thick films.

Device Fabrication. A ~50 nm TiO_2 layer was deposited *via* a sol-gel method onto pre-patterned FTO on glass substrates (Thin Film Devices, Inc.). Sol-gel TiO_2 was prepared by mixing 5 mL EtOH, 2 drops HCl, 125 μL deionized water, and 375 μL of titanium ethoxide, resulting in a clear solution. The headspace of the vial was filled with nitrogen and the solution was stirred for 48 hours, and then kept in the freezer until use. The sol-gel was spin-cast at 3000 RPM for 20 s, annealed at 115 °C and 450 °C for 30 minutes each. The $CsPbI_3$ QD photoactive layer was deposited using the procedure described above, resulting in a total thickness of ~150 nm. The spiro-OMeTAD hole transporting material was spin-cast at 4000 RPM for 30 sec from a solution with a nominal concentration of 72.3 mg of spiro-OMeTAD, 1 mL chlorobenzene, 28.8 μL of 4-TBP, and 17.5 μL of Li-TFSI stock solution (520 mg/mL in acetonitrile). All of the spin-coating processes were performed in ambient. MoO_x was deposited at a rate of 0.2-1.0 Å/s at a base pressure lower than 2×10^{-7} Torr for a total thickness of 15 nm. Al electrodes were evaporated at a rate ranging from 0.5-2 Å/s for a total thickness of 200 nm.

3.3.3 *Quantum dot and Film Characterization*

Ultraviolet-visible (UV-vis) absorption spectra were recorded using a Shimadzu UV-3600 UV-vis-NIR spectrophotometer. Steady-state photoluminescence (PL) and room temperature PL quantum yields (QY) were measured using a Horiba Jobin Yvon fluoromax-4 spectrophotometer. For PLQY measurements, the QDs were dispersed in toluene using rhodamine 6G in EtOH as a reference. UV-vis absorption and PL experiments were done in solution and on thin films

(prepared as described below). Powder X-ray diffraction (XRD) data were recorded using a Bruker D8 Discover X-ray diffractometer with a Hi-Star 2D area detector using Cu K_α radiation (1.54 Å). Transmission electron microscopy (TEM) studies were carried out using FEI T30 at 300 kV. TEM grids were prepared by dropping a dilute colloidal solution of QDs in a hexane-octane mixture onto the carbon coated copper grids.

To further explore the structural properties of the QDs, Rietveld analysis of the XRD data was performed using Materials Analysis Using Diffraction (MAUD) [135], [136] software. In this analysis, the background structural parameters (atomic coordinates, occupancies, lattice parameters, *etc*.), and microstructural parameters (particle size, lattice strain, residual stress, *etc*.) are refined through a least-squares method. This XRD refinement shows that the cubic model provides quantitative fits of the experimental XRD patterns, while the orthorhombic model using experimentally measured lattice parameters [137] cannot be fitted to the XRD pattern. Peak broadening and decreased signal-to-noise complicate the accurate Rietveld refinement of the XRD patterns of the smaller QDs; however, peaks of cubic $CsPbI_3$ are qualitatively observed in all samples.

3.3.4 *Device Characterization*

Devices were tested in both a N_2-filled glovebox or in ambient lab air. The solar simulators used for both setups are Newport Oriel Sol3A solar simulators with xenon lamps. A calibrated reference solar cell (either GaAs or KG2 filtered Si to minimize the spectral mismatch) was used to set the intensity of the lamp to 100 mW/cm^2 AM1.5 conditions. Devices were illuminated for 5 s prior to starting the *J-V* sweep and the device area was 0.10 cm^2. Devices were measured with and without a metal aperture (0.06 cm^2) and produced equivalent current densities. Stabilized power output was measured by holding the device at a constant voltage corresponding to the

voltage at the maximum power point of the *J-V* scan. External quantum efficiency (EQE) measurements were taken using a Newport Oriel IQE200.

3.4 RESULTS AND DISCUSSION

We present an improved synthetic route and purification approach to $CsPbI_3$ QDs. We demonstrate that, once purified, the QDs retain the cubic phase for months in ambient air and even at cryogenic temperatures. A new method for perovskite QD film assembly is described that allows for efficient dot-to-dot electronic transport while retaining the phase stability of the individual nanoparticles. At the time of publication, the solar cells produced from this approach had the highest scan efficiency of 10.77% and stabilized power output of 7.9% of any all-inorganic perovskite absorber, produce 1.23 V at open circuit, among the best of any perovskite PV, and also function as LEDs, emitting visible red light with low turn-on voltage.

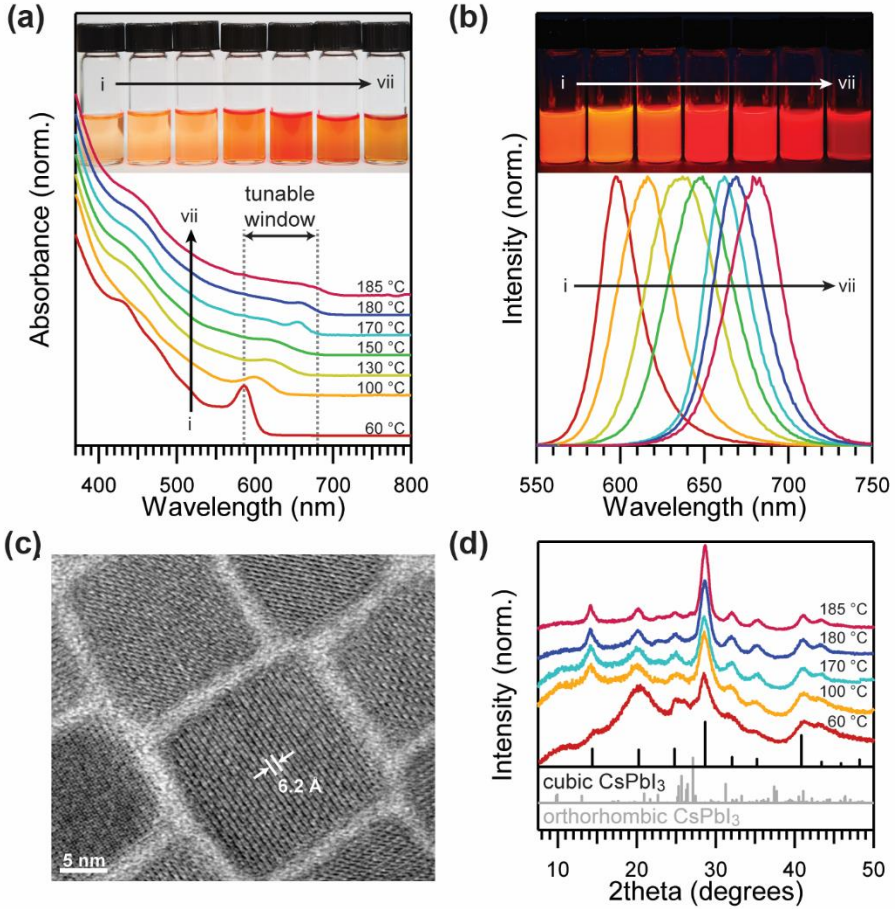

Figure 3.1. Characterization of $CsPbI_3$ QDs. **(a)** UV-Visible absorption spectra and photographs of $CsPbI_3$ QDs synthesized at (i) 60 (3.4 nm), (ii) 100 (4.5 nm), (iii) 130 (5 nm), (iv) 150 (6.8 nm), (v) 170 (8 nm), (vi) 180 (9 nm), (vii) 185 °C (12.5 nm), average size from TEM shown in parentheses. **(b)** Normalized photoluminescence spectra and photographs under UV illumination of the QDs from **(a)**. **(c)** High resolution transmission electron micrograph (HRTEM) of $CsPbI_3$ QDs synthesized at 180 °C. **(d)** XRD patterns of QDs synthesized at (from bottom to top) 60, 100, 170, 180, and 185 °C confirming that they crystallize in the cubic phase of $CsPbI_3$.

Figure 3.1 shows the tunability of the bandgap, due to quantum confinement, in a series of $CsPbI_3$ QDs synthesized at temperatures between 60 and 185 °C. The excitonic peak of $CsPbI_3$ shifts between 585 and 670 nm corresponding to QD sizes between 3 and 12.5 nm. The corresponding normalized PL spectra of the samples are shown in **Figure 3.1(b)**, along with a photograph of the QDs in hexane. Upon UV excitation, emission is in the orange (600 nm) to red (680 nm) color range corresponding to a bandgap between 2.07 and 1.82 eV (photographs showing

PL from dried NC powders are shown in **Figure A.8**). The full width at half maximum of the PL for the smallest QDs is 83 meV, and increases slightly for the larger sizes while the PL quantum yield varied from 21 to 55% for different sizes (**Figure A.9**).

In contrast to the cubic phase instability of bulk $CsPbI_3$ at room temperature, nanocrystals have been reported to retain the cubic phase because of the large contribution of surface energy [59], [60] (**Figure 3.1(d)**). $CsPbX_3$ QDs gain colloidal stability from the dynamic bonding of the ionic, organic ligands [133]. The softer basic nature of I^- compared to Br^- results in weaker acid-base interactions between the halide and the oleylammonium ligand (a hard acid) in the case of $CsPbI_3$, compared to $CsPbBr_3$ [138], [139]. Therefore, the isolation of $CsPbI_3$ QDs is significantly more difficult than that of $CsPbBr_3$ QDs due to loss of ligand during extraction, causing reversion to the orthorhombic phase. To maintain adequate ligand coverage, and thereby preserve the cubic phase of the $CsPbI_3$ QDs, we developed an antisolvent extraction approach utilizing methyl acetate (MeOAc).

The high-resolution transmission electron micrograph (TEM) of the sample synthesized at 180 °C (**Figure 3.1(c)**) shows an interplanar distance of 0.62 nm, consistent with the (100) plane of cubic phase $CsPbI_3$ [59], [131], [137]. Similar to previous reports [139], [140], we find that unpurified QDs transform to the orthorhombic phase within several days (**Figure A.10**). However, we find that QDs purified and washed using this procedure remain stable in the cubic phase for months with ambient storage. In **Figure 3.2**, **(a)** and **(b)**, powder XRD patterns and UV-vis absorption spectra confirm the absence of diffraction peaks or the high energy (~3 eV) sharp absorption characteristic of orthorhombic phase formation [59], despite 60 days of storage in ambient. Additionally, the QDs remained in the cubic phase even after the solution was cooled to 77 K, further demonstrating the expanded temperature stability of the cubic phase.

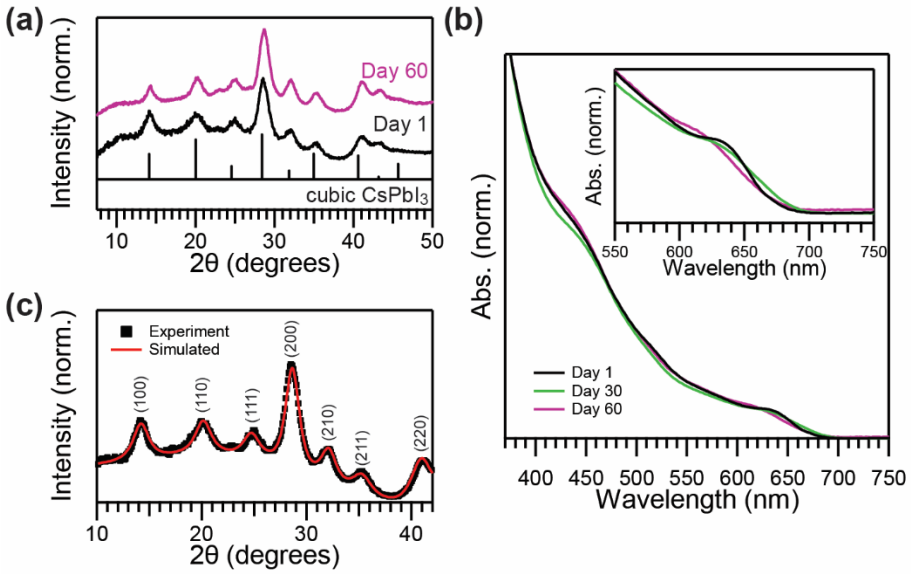

Figure 3.2. Phase Stability of CsPbI3 QDs. **(a)** Powder XRD patterns and **(b)** UV-Visible absorption spectra, normalized at 370 nm, of $CsPbI_3$ QDs synthesized at 170 °C and stored in ambient conditions for a period of 60 days. Inset shows the slight blue shift that is seen in the excitonic peak with extended storage. **(c)** Rietveld refinement fitting of $CsPbI_3$ NC XRD pattern revealing pure cubic phase $CsPbI_3$.

Rietveld refinement of the XRD patterns, shown in **Figure 3.2(c)** and described in the Methods (Section 3.3.3), allows quantification of the contribution from cubic and orthorhombic phases. No detectable orthorhombic phase is found. Additionally, lattice parameters of three different size $CsPbI_3$ NC samples are estimated and shown in **Table 3.1**. The lattice parameter values show a size dependence, such that smaller QDs yielded larger lattice parameters, and are lower than the previously measured experimental value (6.2894 Å at 634 K) of bulk cubic $CsPbI_3$. We note that our measurements were performed at 273 K, whereas high temperatures are required to characterize bulk cubic $CsPbI_3$. The size dependence of the lattice constant validates the role of surface energy of the cubic phase stabilization and reveals how the NC maintains the cubic phase despite containing a smaller A-site cation. A similar increase in lattice parameter with decreasing particle size has been reported in other systems, attributed to electrostatic relaxation with decreasing crystal size [141].

Table 3.1. Results of the Rietveld refinement of varying sizes of $CsPbI_3$ QDs.

QD Size (TEM)	QD Size (Rietveld)	a (Å)	R_{wp}
8 nm	9 ± 1 nm	6.231 ± 0.002	3.42
9 nm	10 ± 1 nm	6.220 ± 0.002	6.50
15.5 nm	17 ± 2 nm	6.189 ± 0.002	7.79

We also assessed the thermal stability of a drop-casted α-$CsPbI_3$ QD film on a Si wafer heated with an *in-situ* heating stage in a N_2 atmosphere at a ramp rate of 1 °C /min. An XRD scan was acquired each minute and the intensities are shown in the color scale in **Figure 3.3** as a function of the 2 theta in the x-axis and temperature along the y-axis. The vertical yellow and red lines at 2θ of 14.1° and 19.9° correspond the cubic, α-$CsPbI_3$ phase, whereas the disappearance of those peaks and emergence of new peaks at ~10° and ~13° correspond to the orthorhombic phase. The white dashed lines serve as a guide for the eye to the phase transition from cubic to orthorhombic at ~210 °C and then the transition from orthorhombic at ~330 °C. We then used Rietveld refinement on scans immediately before and after the cubic to orthorhombic phase transition at ~210 °C to quantify the contribution of cubic and orthorhombic $CsPbI_3$ phases. At 206 °C, the sample remained entirely in the cubic phase with an estimated crystal size enlarged to 70 ± 20 nm. Once the sample temperature reached 213 °C, however, the resultant XRD pattern was consistent with a sample that was 90 wt. % orthorhombic and 10 wt. % cubic. The mixed phase makes the refinement fitting challenging, however we get values consistent with the 206 °C XRD pattern. **Table 3.2** shows summary of the fitting. These results indicate that reversion to the orthorhombic phase correspond with an increase in the QD size. Thus, achieving enhanced cubic phase stability at elevated temperature may be possible by maintaining a smaller nanocrystallite size at higher temperatures. This might be achieved through more robust surface passivation with

durable inorganic capping ligands or infilling of the QD array with a thermally stable matric material, such as an infilled alumina deposited via atomic layer deposition [142].

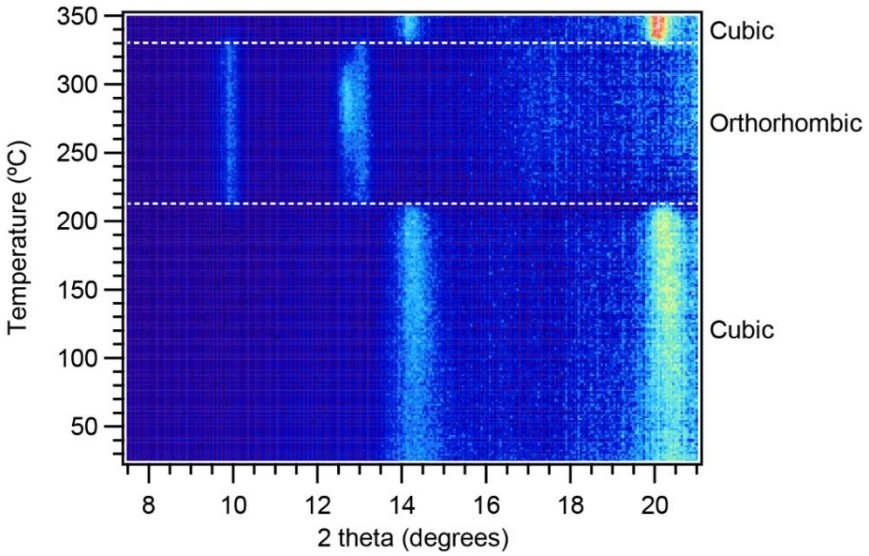

Figure 3.3. Temperature-dependent XRD of drop-casted $CsPbI_3$ QDs. XRD patterns taken at a rate of one scan per min as the sample was heated at a rate of 1 °C per min. The color scale from blue to red indicates the XRD signal intensity, with red coloring indicating higher signal intensity. The dashed white lines were added to serve as a guide to denote phase transition temperatures. The corresponding phase for each temperature range is listed to the right of the plot.

Table 3.2. Results of the Rietveld refinement of $CsPbI_3$ QD film at elevated temperature.

Sample	a (Å)	QD size (Rietveld)
206 °C Cubic	6.207 ± 0.006	70 ± 20 nm
213 °C Orthorhombic (90 wt. %)	a = 10.11 ± 0.05 b = 4.66 ± 0.1 c = 18.07 ± 0.1	100 ± 100 nm
213 °C Cubic (10 wt. %)	6.20 ± 0.1	100 ± 100 nm

To utilize highly phase-stable α-$CsPbI_3$ QDs in optoelectronic devices, we developed a method to cast electronically conductive NC films. QDs are first spin-cast from octane, then dipped in a saturated MeOAc solution of either $Pb(OAc)_2$ or $Pb(NO_3)_2$ (neat MeOAc was used as a control). This process is repeated multiple times, typically 3-5, to produce NC films with thicknesses between 100 and 400 nm. **Figure 3.4** shows characterization of films used in devices. In **Figure 3.4(a)** the optical absorption and PL spectra are shown for three samples with indicated reaction temperature. In each case, the film absorbance and PL is red-shifted ~20 nm from that of the QDs in solution, while the tunable emission properties of the films indicate that quantum confinement is preserved. Fourier transform infrared (FTIR) spectra show the removal of organic ligands from the film with exposure to neat MeOAc (**Figure 3.4(b)**) due to the near absence of C-H modes near 3000 cm^{-1} or below ~2000 cm^{-1} belonging to oleylammonium, oleate, or octadecene.

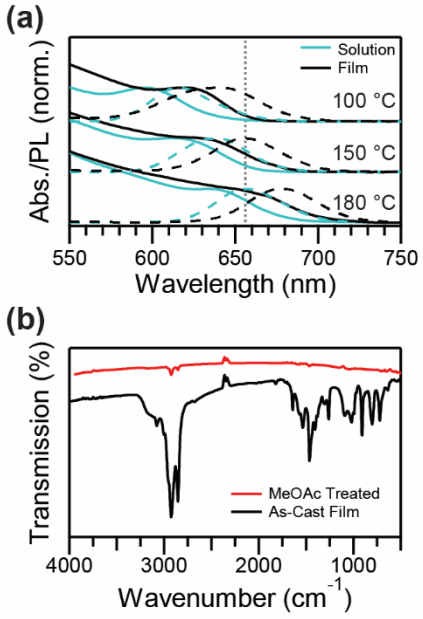

Figure 3.4. Absorption, photoluminescence and FTIR $CsPbI_3$ QD films. (a) UV-visible absorption (solid lines) and PL spectra (dashed lines) of $CsPbI_3$ QDs in solution (blue) and cast as films (black) for QDs synthesized at 100, 150, and 180 °C. (a) FTIR spectra showing the IR transmission of a $CsPbI_3$ NC film as cast (black) and after treating with MeOAc (red).

Furthermore, we probed the interaction of Pb^{2+} salts with QDs in solution and on films by monitoring the fluorescence (**Figure A.11**). Titration of a small amount of $Pb(OAc)_2$ to the NC solution shows an enhancement in PL, suggesting improved surface passivation. Titrations using only MeOAc cause fast PL quenching. Similarly, dip-coating of the NC film in a saturated solution of $Pb(OAc)_2$ in MeOAc results in a significant PL enhancement.

Based on these findings, we fabricated solar cells employing $CsPbI_3$ QDs as a photoactive material with the initial trials showing very promising results (schematic of device architecture shown in **Figure 3.5(a)**, scanning electron micrograph cross section image shown in **Figure 3.5(b)**). The reverse scan *J-V* curves show an V_{OC} of 1.23 V, and 10.77% PCE for a cell made and tested completely in ambient conditions (relative humidity ~15-25%) (**Figure 3.5(c)**). Furthermore, the PCE improved from its initial value over the course of 15 days storage in dry but ambient conditions. In **Figure A.13**, we show the stabilized power output of 7.9% by measuring the current density while the device is biased at 0.92 V, which is represented by the black diamond in **Figure 3.5(c)**. In **Figure 3.5(d)**, the spectral response of the solar cell is shown. Both, the *J-V* scan efficiency and stabilized power output are higher for these QD devices than other previously published devices employing all-inorganic perovskites as the absorber material [57]–[59]. Additionally, previous reports indicate that $CsPbI_3$ devices must be fabricated and measured in nitrogen dry boxes [59], in contrast to what we find using QDs. The high V_{OC} is unprecedented in QD solar cells, and among the highest V_{OC} in all perovskite literature for bandgaps below 2 eV. This is despite the fact that we have not optimized the device architecture nor the NC film treatment scheme. We find that dip-coating spin-cast films in neat MeOAc, and MeOAc saturated with $Pb(OAc)_2$ or $Pb(NO_3)_2$ all work reasonably well (*J-V* scanned PCE > 9%) in photovoltaic devices.

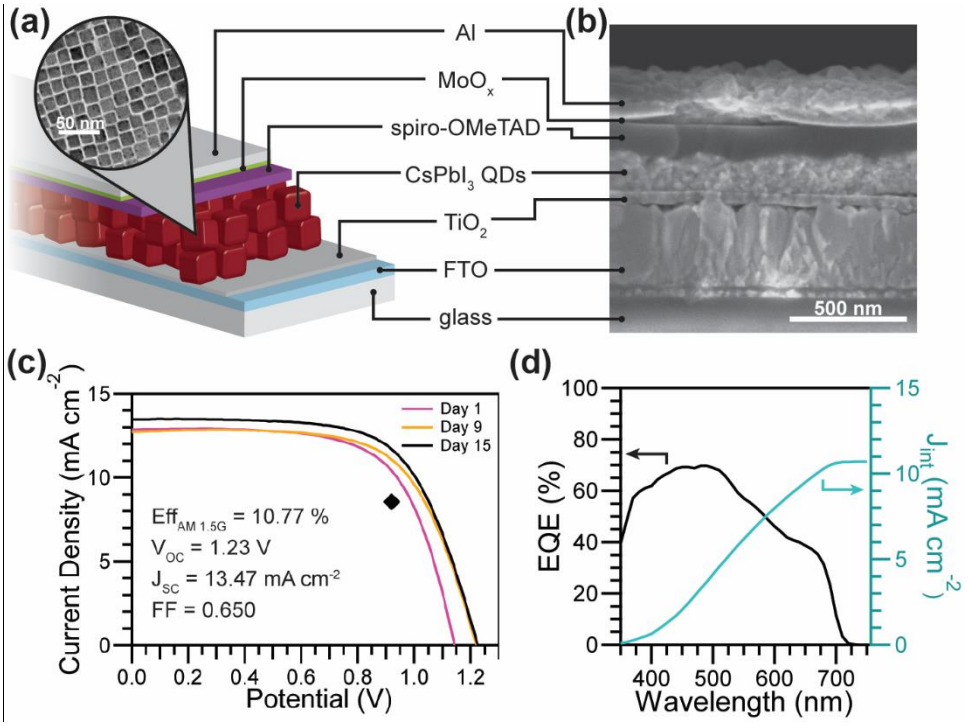

Figure 3.5. $CsPbI_3$ Optoelectronic Devices. **(a)** Schematic (with HRTEM image of QDs) and **(b)** SEM cross-section of the $CsPbI_3$ solar cells. **(c)** Current-voltage curves of a device measured in air over the course of 15 days. The black diamond represents the stabilized output of the device at 0.92 V, as shown in **Figure A.13**. **(d)** External quantum efficiency (black, left ordinate) and integrated current density (blue, right ordinate) of the device.

To assess the relative stability different inorganic $CsPbX_3$ perovskite absorber materials we fabricated a set of devices with $CsPbI_3$ QDs, thin film $CsPbI_3$ and thin film $CsPbI_2Br$. The $CsPbI_3$ and $CsPbI_2Br$ thin films were fabricated using methods reported by Eperon *et al.* [59] and Sutton *et al.* [58], respectively. The same device stack, described above, was used for each of the three perovskite absorber layers. The *J-V* scans were acquired upon initial fabrication and then retested after 2 days of storage in an ambient environment with relative humidity of 40-60% as shown in **Figure 3.6**. The device parameters from these scans are summarized in **Table 3.3**. Comparing the initial *J-V* scans in this set of devices, we observe the highest efficiency from the $CsPbI_3$ QDs absorber with 9.5%. The performance of the thin film $CsPbI_2Br$ solar cell is only slightly lower at 8.18%, and the thin film $CsPbI_3$ solar cell is significantly lower at 2.42%, which are both

comparable to the literature values. The $CsPbI_3$ QD device had a higher *Voc* and *FF* compared to the thin film $CsPbI_2Br$ solar cells, whereas the $CsPbI_2Br$ had a slightly higher J_{SC}. Interestingly, the thin film $CsPbI_3$ had a significant boost in the J_{SC}, but suffered dramatic losses in the *Voc*.

After 2 days of storage in relative humidity of 40-60%, all of the devices degraded significantly. The $CsPbI_3$ QDs, however, preserved the most of its initial efficiency compared to the thin film variants. Notably, the J_{SC} for both the $CsPbI_3$ and $CsPbI_2Br$ thin film solar cells had reduced to less than 1 mA cm^{-2}, whereas the $CsPbI_3$ QD solar cells maintained ~64% of its initial J_{SC}, yielding 6.65 mA cm^{-2}. A phase transition to the higher bandgap orthorhombic phase would lead to a dramatic drop in the J_{SC} due to a significant reduction in light absorption in the solar spectrum. It could also have further implications on the charge transport, however, the electronic structure of the orthorhombic phase, and cubic-orthorhombic mixed phases was not investigated in this work. Additionally, further research on the role of moisture on the phase transition of these inorganic $CsPbX_3$ perovskite devices is necessary given the relatively poor storage stability of devices made from all three of these perovskite absorber materials.

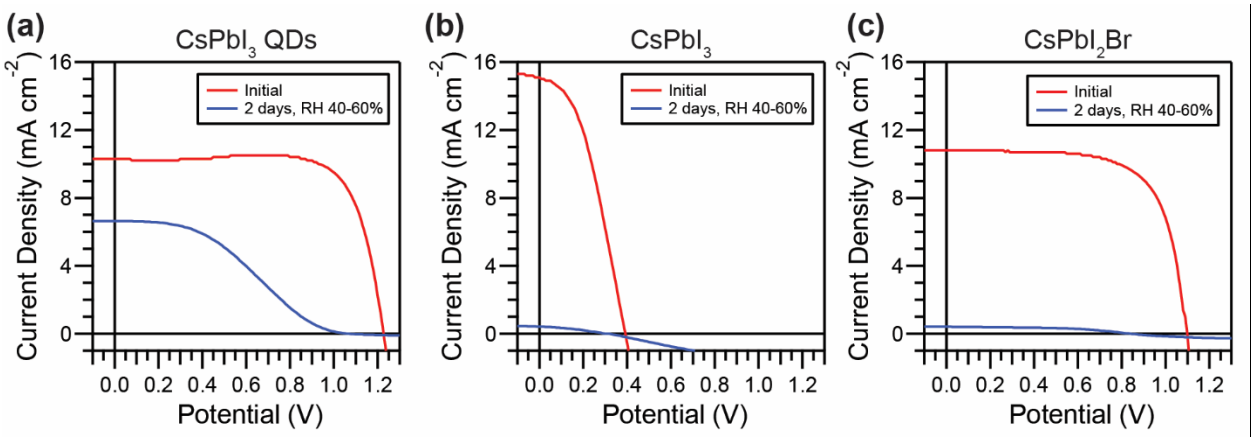

Figure 3.6. $CsPbI_3$ QDs versus bulk $CsPbX_3$ films in humid air. Current density-voltage curves of TiO_2/perovskite/spiro-OMeTAD/MoO_x/Al solar cells with **(a)** $CsPbI_3$ QD, **(b)** bulk $CsPbI_3$, **(c)** and bulk $CsPbI_2Br$ perovskite active layers. The devices were measured following fabrication (red curves) and after storage for 2 days in the dark in ambient conditions (blue curves). The ambient relative humidity was 40-60%.

Table 3.3. Summary device performance with storage in 40-60% relative humidity.

Perovskite Active Layer	Test	J_{SC} (mA cm^{-2})	V_{OC} (V)	FF	PCE (%)
$CsPbI_3$ QDs	Initial	10.30	1.23	0.743	9.50
	2 days, RH 40-60%	6.65	1.07	0.358	2.55
Bulk $CsPbI_3$	Initial	15.40	0.40	0.393	2.42
	2 days, RH 40-60%	0.47	0.32	0.289	0.044
Bulk $CsPbI_2Br$	Initial	10.80	1.10	0.689	8.18
	2 days, RH 40-60%	0.43	0.85	0.472	0.17

Operational stability of the three different inorganic $CsPbX_3$ perovskite absorber materials was also investigated. The initial *J-V* scans of the $CsPbI_3$ QD, thin film $CsPbI_3$ and thin film $CsPbI_2Br$ devices are shown in **Figure 3.7 (a)**, **(b)**, and **(c)**, respectively. The *J-V* scans were used to determine the max power point voltage, which was then used to measure stabilized power output as seen in **Figure 3.7(d)**. The stabilized power output of each of the devices was measured in ambient conditions with a relative humidity of ~40-60% without any encapsulation or active heating or cooling of the devices. The operational stability study indicates that the $CsPbI_3$ QDs also maintain the best operational stability of the inorganic perovskite absorber layers studied here. In contrast, the thin film $CsPbI_2Br$ declines nearly linearly over the course of 3600 s. The thin film $CsPbI_3$ solar cell doesn't decrease dramatically, however, the low initial efficiency is problematic. Stabilized power output of the $CsPbI_3$ QD solar cell was also measured at an elevated temperature of 85 °C (**Figure 3.7(e)**), with surprising durability. Although there is a decline in power output over the 7200 s of measurement, it should be noted that this device architecture uses Spiro-OMeTAD, which known to degrade at moderate temperatures in ambient [143].

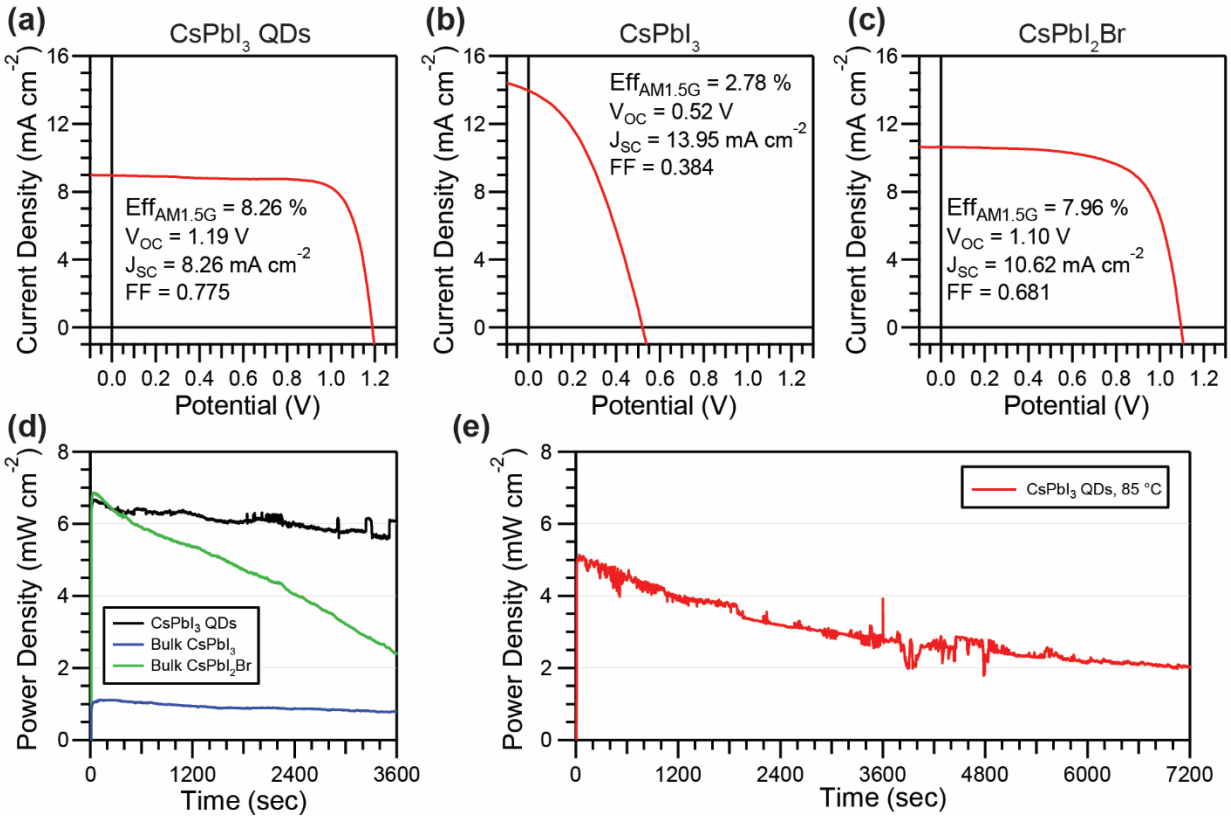

Figure 3.7. Long-term stabilized power output in humid air. Current density-voltage curves of TiO_2/perovskite/Spiro-OMeTAD/MoO_x/Al solar cells with **(a)** $CsPbI_3$ QD, **(b)** bulk $CsPbI_3$, **(c)** and bulk $CsPbI_2Br$ perovskite active layers. **(d)** The stabilized power output (SPO) of the solar cells shown in (a-c) conducted in ambient conditions, without active heating/cooling, over the course of 3600 s. The bias voltages used were 0.92 V, 0.30 V, and 0.88 V, respectively. **(e)** SPO measurements conducted for 7200 s at 85 °C on a $CsPbI_3$ QD solar cell (J_{SC} = 10.71 mA cm^{-2}, V_{OC} = 1.19 V, FF = 0.642, efficiency = 8.16 %) near the maximum power point of the device at this elevated temperature (bias voltage = 0.65 V). For all of these measurements the devices were completely unencapsulated.

Given the impressive PL properties of these perovskite QDs, we were also interested in their ability to perform as LEDs. We find that the photovoltaic devices also produce visible electroluminescence (EL) when biased above the V_{OC}. **Figure 3.8(a)** shows the EL properties of the devices. The EL is characterized by a low turn-on voltage near the bandgap of the $CsPbI_3$ with increasing intensity at larger applied biases. These spectra provide direct evidence that quantum confinement is retained in the complete devices as seen by the shift in both the EL and PL spectra of devices with different size QDs (**Figure 3.8(f)**).

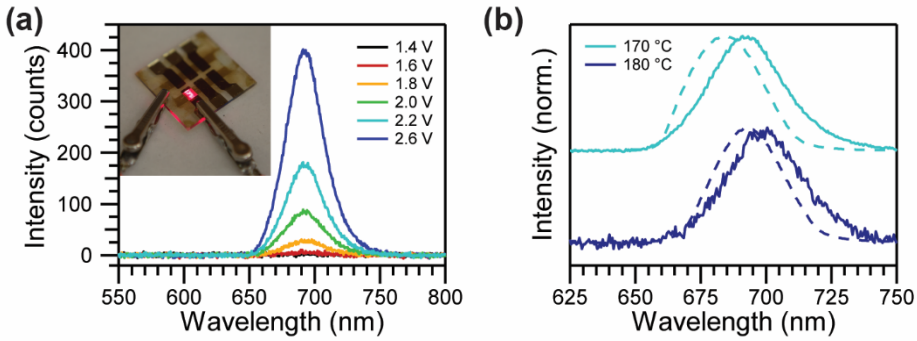

Figure 3.8. Electroluminescence of $CsPbI_3$ QD devices. **(a)** EL spectra of $CsPbI_3$ solar cell ($CsPbI_3$ synthesized at 170 °C) under forward bias. The inset shows a photograph of the luminescent device. **(b)** PL (dotted lines) and EL (solid lines) spectra of completed devices fabricated using $CsPbI_3$ QDs synthesized at 170 and 180 °C demonstrating size quantization effects in the completed devices.

3.5 Conclusions and Outlook

Herein, we have shown greatly improved phase stability of all-inorganic halide perovskite materials. We utilize colloidal nanocrystals to stabilize $CsPbI_3$ in the cubic perovskite phase, which is highly desirable for optoelectronic applications. We then developed a ligand exchange that removes the organic capping group, enabling electronic coupling of the nanocrystal film yet still preserving cubic phase stability. This results in the highest reported solar cell efficiency for an all-inorganic perovskite even though the absorber is composed of quantum dots. The devices can also be operated as LEDs when forward biased and show low turn-on voltages, while exhibiting exceptional phase stability compared with bulk or thin film versions of the same chemical composition.

These results could have a dramatic impact on the field of perovskite solar cells. First, the bandgap range of $CsPbI_3$ QDs is well-suited for multi-junction and tandem solar cells. Considering the remarkably high voltage achieved with this material, it could lead to efficient all perovskite tandem solar cells. Furthermore, compared to organic-inorganic perovskite materials, it is likely that the $CsPbI_3$ QDs will be more robust to various processing conditions. This is particularly

useful for depositing a transparent electrode, which may require a relatively harsh physical deposition process. Second, the use of colloidally-synthesized perovskite QDs decouples the grain growth from film deposition. In many cases, the precursor solutions and annealing conditions of thin film perovskite must be optimized for both complete surface coverage, as well as high crystallinity. Therefore, by decoupling these two processes, perovskite QDs may produce better photoactive layers overall. Third, the QD synthesis, isolation, and film processing use industry-friendly solvents unlike conventional perovskite precursor solutions. $CsPbI_3$ QD film deposition uses octane and MeOAc, which are significantly less toxic than dimethylformamide and lead-containing dimethylsulfoxide solutions used for thin films. Additionally, there are no annealing steps required for the $CsPbI_3$ QD films, which makes it compatible with a number of low-temperature substrates. Finally, we observed remarkably high *Voc* from the $CsPbI_3$ QD solar cells not observed in their thin film counterparts. Although we have not identified the mechanisms for this extremely high *Voc,* it may be related to the QD band structure or the high photoluminescence quantum yield. Given these very promising results, I continued to investigate the $CsPbI_3$ QD system and explored strategies to improve its photovoltaic performance.

Chapter 4. ENHANCED MOBILITY OF $CsPbI_3$ QUANTUM DOT ARRAYS FOR RECORD EFFICIENCY, HIGH VOLTAGE PHOTOVOLTAIC CELLS

Manuscript submitted for publication:
Sanehira, E. M.; Marshall, A. R.; Christians, J. A.; Harvey, S. P.; Ciesielski, P. N.; Wheeler, L. M.; Schulz, P.; Lin, L. Y.; Beard, M. C.; Luther, J. M. Enhanced mobility $CsPbI_3$ quantum dot arrays for record efficiency, high voltage photovoltaic cells.

4.1 ABSTRACT

We developed lead halide perovskite quantum dot (QD) films with new surface chemistry based upon A-site cation halide salt (AX) treatments. QD perovskites offer colloidal synthesis and processing using industrially friendly solvents, which decouples grain growth from film deposition, and produce larger open circuit voltages (V_{OC}'s) compared to thin film perovskites. $CsPbI_3$ QDs, with a tunable bandgap between 1.75 and 2.13 eV, are an ideal top cell candidate for all-perovskite multijunction solar cells and have demonstrated a smaller V_{OC} deficit than their thin film counterpart. Here, we show that charge carrier mobility within perovskite QD films is dictated by the chemical conditions at the QD-QD junctions. Understanding what chemical conditions are necessary for optimal charge transport is essential for fabricating high quality QD films and devices. The AX treatments presented here double the film mobility, enabling increased photocurrent and lead to a certified QD solar cell (QDSC) efficiency of 13.43%.

4.2 INTRODUCTION

Colloidal quantum dot (QD) materials offer unique properties over those afforded by conventional thin films for optoelectronic and other applications. While it is well known that colloidal QD systems offer immense tunability in the material bandgap, energetic position of the

electronic states, and surface chemistry, more unique features are being discovered [144]–[147]. For photovoltaics (PVs), colloidal QDs exhibit efficient multiple exciton generation which led to the first PV and photoelectrochemical cells with external quantum efficiency (EQE) exceeding unity within the solar spectrum [63], [148]. Additionally, it has recently been shown that colloidal $CsPbI_3$ QD materials stabilize the cubic perovskite crystal phase [60], [147], whereas thin film $CsPbI_3$ materials relax to an orthorhombic phase at ambient temperature [59]. In this Chapter, we greatly improve QD surface properties through A-site cation halide (AX) treatments doubling the $CsPbI_3$ QD film mobility, thus enabling increased photocurrent and a certified record QD solar cell (QDSC) power conversion efficiency (PCE) of 13.43%.

$CsPbI_3$ with $Pm\bar{3}m$ cubic symmetry exhibits the lowest bandgap (E_g = 1.73 eV) [22] among the all-inorganic Pb-halide perovskite materials for PV. At room temperature, however, the orthorhombic phase with $Pnma$ space group symmetry (E_g = 2.82 eV) is thermodynamically preferred [149]. To overcome this phase instability, the addition of bromide ($CsPbI_{3-x}Br_x$) has been shown to reduce the phase transition temperature from over 300 °C to ~110 °C [149]; however, for PV applications, this reduction in temperature is not low enough, and alloying comes at the expense of increasing the bandgap to ~1.9 eV for $CsPbI_2Br$ [57], [58]. In an alternative approach, we previously demonstrated that by leveraging the surface energy of QDs, the cubic phase can be stabilized at room temperature and below, leading to a PV device with efficiency >10% [147]. Although we observed a high open-circuit voltage (V_{OC}) (~85% of the maximum voltage from the Shockley Queisser analysis for the given bandgap), the short-circuit current density (J_{SC}) was limited by transport. This is a common trade-off in QDSCs whereby increasing light absorption with thick absorber layers reduces charge extraction efficiency in transport-limited QD films [68]. Herein, we show an AX post-treatment (AX, where A = formamidinium, FA^+; methylammonium,

MA^+; or cesium, Cs^+, and X = I^- or Br^-) that greatly improves the electronic coupling between QDs which enhances carrier mobility. We characterize the structural and optical properties of the resultant $CsPbI_3$ QD films and determine that the fabrication process enables the films to retain nanocrystalline character to preserve quantum confinement, and that the AX salt species coats the QDs in the array rather than alloying or inducing grain growth in the films (these AX post-treated $CsPbI_3$ QD films are thus subsequently referred to as AX-coated).

4.3 METHODS

4.3.1 *Quantum dot synthesis and film deposition*

Materials. All chemicals were purchased from Sigma-Aldrich and used as-received unless otherwise specified. Cesium carbonate (Cs_2CO_3, 99.9%), lead (II) iodide (PbI_2, 99.9985%, Alfa Aesar), oleic acid (OA, technical grade 90%), oleylamine (OAm, technical grade 70%), 1-octadecene (ODE, technical grade 90%), hexane (reagent grade ≥95%), octane (anhydrous, ≥99%), methyl acetate (MeOAc, anhydrous, 99.5%), lead (II) nitrate ($Pb(NO_3)_2$, 99.999%), ethyl acetate (EtOAc, anhydrous, 99.8%), cesium iodide (CsI, 99.999%), formamidinium iodide (FAI, Dyesol), formamidinium bromide (FABr, Dyesol), methylammonium iodide (MAI, Dyesol), methylammonium bromide (MABr, Dyesol), ethanol (EtOH, 200 proof, ≥99.5%), titanium ethoxide (≥97%), hydrochloric acid (HCl, 37% in water), 2,2′,7,7′-Tetrakis(N,N-di-p-methoxyphenylamine)-9,9′-spirobifluorene (spiro-OMeTAD, Lumtec, ≥99.5%), chlorobenzene (anhydrous, 99.8%), 4-tert-butylpyridine (4-TBP, 96%), bis(trifluoromethane)sulfonimide lithium salt (Li-TFSI), and acetonitrile (anhydrous, 99.8%).

Quantum dot synthesis and purification. $CsPbI_3$ QDs were synthesized [60] and purified [147] using previously reported methods with slight modifications. Cs-oleate in ODE solution (0.125M)

was synthesized by first degassing 0.407 g Cs_2CO_3, 1.25 mL OA and 20 mL ODE in a 100 mL 3-neck flask under vacuum at 120 °C for 30 min under stirring. After purging the flask with N_2, the flask was heated to 150 °C until the reaction was complete, and yielded a clear solution. The Cs-oleate in ODE solution was cooled and stored in N_2 until needed for a QD synthesis. To synthesize $CsPbI_3$ QDs, 0.5 g of PbI_2 and 25 mL of ODE was degassed in a 100 mL 3-neck flask under vacuum at 120 °C for 30 min under stirring. Pre-heated OA and OAm (130 °C, 2.5 mL of each) was added to the reaction flask and degassed briefly until the PbI_2 had completely dissolved. The reaction flask was purged with N_2 and then heated to the desired reaction temperature (typically 185 °C) to achieve the desired nanocrystal size. Once the reaction temperature was reached, 2 mL of pre-heated Cs-oleate in ODE (130 °C, 0.125M) was injected into the reaction flask. The reaction was quenched in an ice bath after 5-10 sec. To isolate the QDs, 35 mL of MeOAc was added to 15 mL of the QD reaction liquor and then centrifuged at 7,500 RPM for 5 min. The supernatant was discarded and the QD pellet was redispersed in ~5 mL of hexane. A minimal amount of MeOAc (~5-8 mL) was added to the QDs until the dispersion appeared cloudy, and then it was immediately centrifuged at 7,500 RPM for 5 min. The resultant QD pellet was dispersed in 15 mL of hexane and then stored in the dark at 4 °C for at least 24 h to precipitate excess Cs-oleate and Pb-oleate. Prior to use, these solid precipitates were removed from the QD solution via centrifugation at 7,500 RPM for 5 min.

Film fabrication. Coupled $CsPbI_3$ QD films were fabricated using previously reported methods.[147] Saturated $Pb(NO_3)_2$ in MeOAc and AX salt (where AX = FAI, FABr, MAI, MABr, or CsI) in EtOAc solutions were prepared by sonicating 20 mg of $Pb(NO_3)_2$ (or AX salt) and 20 mL of MeOAc (or EtOAc) for 10 min. Because all of the salts were only slightly soluble in their corresponding solvent, excess salt was removed via centrifugation at 3,500 RPM for 5 min. Each

layer of $CsPbI_3$ QDs was spin-cast from a concentrated QD solution in octane (~75 mg/mL) at a spin speed of 1,000 RPM for 20 s, and 2,000 RPM for 5 s. The film was then briefly dipped (~1 s) into the $Pb(NO_3)_2$ in MeOAc solution, rinsed in a solution of neat MeOAc, and then immediately dried in a stream of dry air. This process of spin-coating QDs and dipping in $Pb(NO_3)_2$ in MeOAc solution was repeated 3-5 times to achieve a total film thickness of 100-500 nm. Once the desired film thickness was achieved, the films were post-treated by soaking the film in the AX salt in EtOAc solution for 10 s before rinsing in MeOAc and then immediately drying under a stream of dry air. All film fabrication was carried out in dry ambient conditions (relative humidity ~16-20 %).

4.3.2 *Film characterization.*

Optical and structural characterization. Ultraviolet-visible (UV-vis) absorption spectra were recorded using a Shimadzu UV-3600 UV-vis-NIR spectrophotometer. Absorptance was calculated from the reflectance and transmittance spectra acquired with an integrating sphere. Steady-state photoluminescence (PL) were measured using a Horiba Jobin Yvon fluoromax-4 spectrophotometer. Powder X-ray diffraction (XRD) data were recorded using a Bruker D8 Discover X-ray diffractometer with a Hi-Star 2D area detector using Cu Kα radiation (1.54 Å). Fourier Transmission Infrared (FTIR) spectra were acquired with a Nicolet 6700 FTIR spectrometer on QD films on Si substrates.

Time-of-flight Secondary Ion Mass Spectrometry. Secondary Ion Mass Spectrometry (SIMS) is a powerful analytical technique for determining elemental and isotopic distributions in solids, as well as the structure and composition of organic materials [150]–[152]. An ION-TOF ToF-SIMS V Time of Flight SIMS (ToF-SIMS) spectrometer was utilized to depth profile the perovskite QD films. Analysis was completed utilizing a 3-lens 30 kV BiMn primary ion gun, the

Bi^{3+} primary-ion beam (operated in bunched mode; 20 ns pulse width, analysis current 0.7 pA), was scanned over a 25×25 micron area. Depth profiling was accomplished with a 3 kV oxygen ion sputter beam (10.8 nA sputter current) raster of 150×150 micron area. All spectra during profiling were collected at or below a primary ion dose density of 1×10^{12} ions/cm^2 to remain under the static-sims limit. The data is plotted with the intensity for each signal at each data point normalized to the total ion counts measured at that data point, which diminishes artifacts from a changing ion yield in different layers when profiling through completed devices, as well as artifacts due to minor fluctuations in the primary ion beam current. We assigned the *m/z* signals at 45, 127, 206 and 266 to FA^+, I^+, $^{206}Pb^+$ and Cs_2^+, respectively, and simply refer to these signals as the FA, I, Pb and Cs signals in the manuscript, respectively. The Cs_2^+ and $^{206}Pb^+$ signals were tracked because they were the most intense species for Cs^+ and Pb^{2+}, respectively, which did not lead to detector saturation. In contrast, Cs^+, Pb^{2+}, and other abundant lead isotopes saturated the detector under the measurement conditions utilized.

Atomic Force Microscopy. QD films were prepared on FTO coated glass as described above. Samples were mounted using double-sided adhesive strips to metal disks exposing the QD layer. Imaging was performed with Multi-Mode scanning probe microscope equipped with a NanoScope IV controller (Bruker, Santa Barbara, CA). Height images were obtained in soft tapping mode using etched silicon probes (TESP, Bruker) with an auto-tuned resonance frequency range of 250 to 300 kHz at a scan rate of 2 Hz. Images were analyzed with Nanoscope Analysis v1.2 software.

Scanning electron microscopy. Samples were mounted on aluminum stubs with double-sided carbon tape and sputter-coated with 3 nm of Iridium prior to imaging. Images were obtained with a FEI Quanta 400 FEG instrument (FEI, Hillsboro, OR). Imaging was performed with a beam accelerating voltages of 30 keV.

THz spectroscopy. Films for THz measurements were deposited directly onto 1x2 cm quartz substrates following similar spin-coating procedures described above. PbS and PbSe QD samples were synthesized and fabricated as previously published using PbI_2 ligand exchange treatment [68], [77]. $MAPbI_3$ films were prepared as described by Ahn *et al.* by spin-coating from a DMF/DMSO solution containing stoichiometric MAI:PbI_2 [83]. The change in THz transmission was recorded as a function of delay from an optical pump pulse (wavelength = 516 nm) with a fluence of 5 x 10^{15} photons/cm^2/pulse. For thin films, the mobility and carrier lifetime are directly proportional to the change in THz transmission through the following relationship: $\left(\mu_e \cdot f_e(\tau) + \mu_h \cdot f_h(\tau)\right) = [\Delta E(\tau)/E] \cdot [(1 + n_s)c\varepsilon_0/(e \cdot J_{abs})]$ [153]. Here $\Delta E/E$ is the measured THz response (see **Figure 4.9(a)**) at a pump delay of τ, n_s is the refractive index of the substrate (n_s = 2.19 here), *c* is the speed of light, ε_0 is the permittivity of free space, *e* is the charge of an electron, and J_{abs} is the absorbed photon fluence and is related to the film OD by $J_{abs} = (1 - R) \cdot (1 - 10^{-OD}) \cdot J_{in}$ where *R* is the reflection coefficient and J_{in} is the measured photon fluence at the sample position. At $\tau = 0$, both the normalized electron and hole carrier decay is 1 ($f_e(0) = f_h(0) = 1$) and the signal in **Figure 4.9(b)** is the sum of the electron and hole mobilities; $(\mu_e + \mu_h) = \mu_s$.

X-ray photoemission spectroscopy. XPS data was taken on a Kratos NOVA spectrometer calibrated to the Fermi edge and core level positions of sputter-cleaned metal (Au, Ag, Cu, Mo) surfaces. Spectra were acquired using monochromated Al Kα radiation (1486.7 eV) at a resolution of 600 meV (pass energy 20 eV). The data was averaged from multiple spots on the sample while the X-ray intensity was held low (15 W anode power) to avoid sample degradation [154] and fit using Pseudo-Voigt profiles.

Time-resolved photoluminescence. Time resolved photoluminescence was measured using a Hamamatsu streak camera system (C10910-05), while the excitation source was a Fianium Supercontinuum high power broadband fiber laser (SC400-2-PP). The chosen excitation wavelength was 530 nm at ~25 μW power on a spot size of 0.02 mm^2.

4.3.3 *Photovoltaic device fabrication and characterization*

Photovoltaic device fabrication. A ~50 nm TiO_2 layer was deposited *via* a sol-gel method onto pre-patterned FTO on glass substrates (Thin Film Devices, Inc.). Sol-gel TiO_2 was prepared by mixing 5 mL EtOH, 2 drops HCl, 125 μL deionized water, and 375 μL of titanium ethoxide, resulting in a clear solution. The headspace of the vial was filled with nitrogen and the solution was stirred for 48 hours, and then kept in the freezer until use. The sol-gel was spin-cast at 3000 RPM for 20 seconds, annealed at 115 °C and 450 °C for 30 minutes each. The $CsPbI_3$ QD photoactive layer was deposited using the procedure described above, resulting in a total thickness of 100-400 nm. The spiro-OMeTAD hole transporting material was spin-cast at 5000 RPM for 30 sec from a solution with a nominal concentration of 72.3 mg of spiro-OMeTAD, 1 mL chlorobenzene, 28.8 μL of 4-TBP, and 17.5 μL of Li-TFSI stock solution (520 mg/mL in acetonitrile). All of the spin-coating processes were performed in ambient. MoO_x was deposited at a rate of 0.2-1.0 Å/s at a base pressure lower than 2×10^{-7} Torr for a total thickness of 15 nm. Al electrodes were evaporated at a rate ranging from 0.5-2 Å/s for a total thickness of 200 nm. A 70 nm layer of MgF_2 was evaporated on the glass side as an anti-reflective coating for the best-performing, certified PV device. A schematic and cross-sectional SEM image of the device stack is provided in **Figure 4.1**.

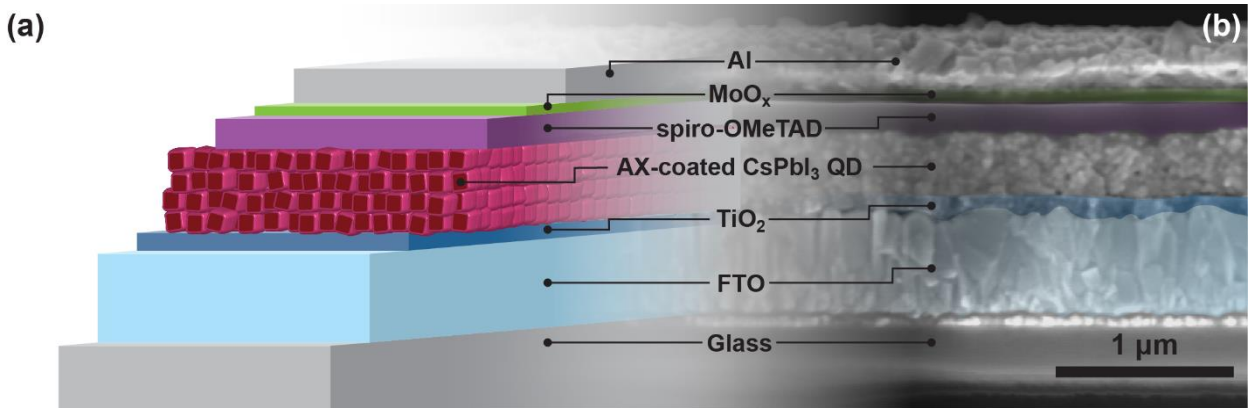

Figure 4.1. Cross section of AX-coated $CsPbI_3$ QDSC. (a) Schematic of the device cross-section and (b) SEM cross-section of a completed devices with false coloring used to delineate different layers in the device stack. Image credit: Alfred Hicks.

Device characterization. Devices were tested in a N_2-filled glovebox with a Newport Oriel Sol3A solar simulator with xenon lamp source. Light intensity was calibrated with a KG5 filtered Si reference diode to minimize the spectral mismatch and to set the intensity of the lamp to 100 mW/cm^2 AM1.5 conditions. Devices were illuminated through a metal aperture (0.058 cm^2) External quantum efficiency (EQE) measurements were taken using a Newport Oriel IQE200.

Due to the hysteretic nature of perovskite solar cells, it is important to develop rigorous testing protocols that yield meaningful metrics [155]. Although stabilized power output (SPO) – which is measured by monitoring the current over an extended period of time while the device is held at a constant voltage – can often be used to report the power conversion efficiency, it cannot provide other useful parameters such as *Voc* and J_{SC}. Stabilized *Voc* and J_{SC} can be measured separately, but this can be impractical for larger sets of devices. To achieve reasonable accuracy in a practical amount of time, slow *J-V* scans can provide nearly accurate photovoltaic parameters but without conducting multiple lengthy stabilized measurements.

The effect of the scan rate and direction of the *J-V* scan is demonstrated in **Figure 4.2(a)** and the photovoltaic parameters are summarized in **Table 4.1**. In these devices, reducing the scan rate to ~20 mV/s by setting the time delay between points to 0.5 s yielded the least hysteresis between

the forward and reverse *J-V* scans (ΔPCE=1.12%), whereas the fastest scan rate of ~1 V/s (time delay = 0.01 s) yielded a very significant difference in PCE between the forward and reverse scans (ΔPCE=6.34%). The SPO of this same device was measured at 4 different voltage set points (0.85, 0.9, 0.95 and 1 V) near the maximum power point (MPP) calculated from the slowest reverse *J-V* scan as shown in **Figure 4.2(b)**. In the inset of **Figure 4.2(b)**, the stabilized power output at these 4 voltage set points are plotted and a Gaussian fit is applied to calculate a MPP based on these measured SPO points. Both the measured SPO and calculated MPP are represented in **Figure 4.2(a)** by the gray and black x's, respectively. A summary of the SPO efficiencies, the calculated MPP from the Gaussian fit and the MPP from the slow reverse *J-V* scan is provided in **Table 4.2**.

First, it is observed that the *Voc* and J_{SC} values from the forward and reverse scans are in close agreement when the scan speed is reduced to ~20 mV/s (time delay = 0.5 s). Second, the PCE from the slow (time delay = 0.5 s) reverse *J-V* scan efficiency (11.35%) is within 0.4 absolute percent of the Gaussian fit MPP (10.95%) and within 0.5 absolute percent of the highest measured SPO point (10.89%), which is also in good agreement. Thus, the slowest scan rate of ~20 mV/s is used to determine the photovoltaic parameters in this chapter (unless otherwise noted). As a trade-off, fewer devices could be measured using such a slow scan rate. From the 4 measured SPO points, there is little difference between using the set voltage of 0.9 V (corresponding to 10.83%) and 0.95V (corresponding to 10.89%). Both of these voltage set points are within 50 mV of the calculated MPP from the slow reverse *J-V* scan (V_{MP} = 0.94 V), and we also see the that the Gaussian fit of the SPO points yielded a V_{MP} of 0.93 V; all of which suggests that a single SPO measurement at the calculated MPP from the slow reverse *J-V* scan will yield a PCE very close to the maximum PCE of the device.

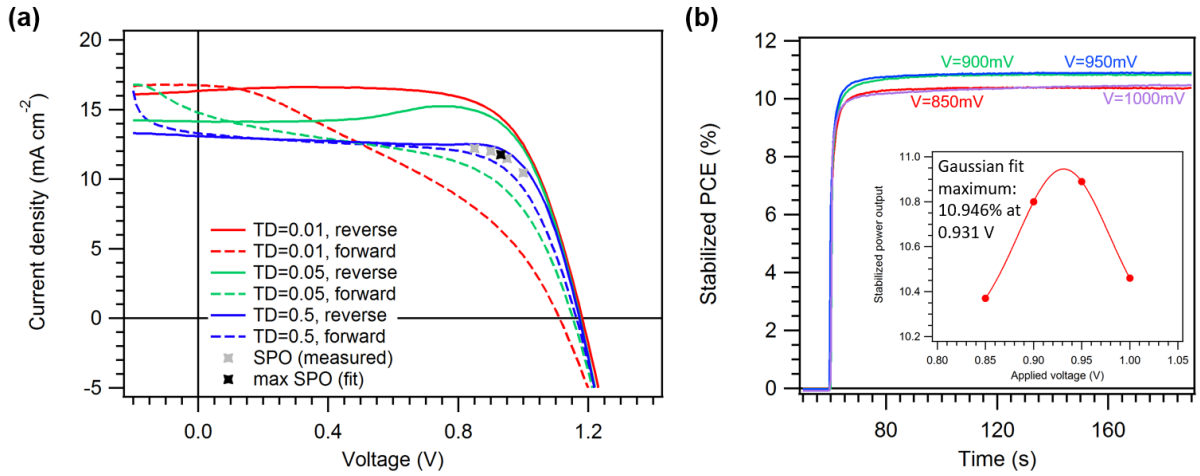

Figure 4.2. Comparison of *J-V* characteristics to stabilized power output. (a) Forward (dotted) and reverse (solid) *J-V* scans of the same device taken at different scan rates. The fastest to slowest scans taken with time delays of 0.01, 0.05 and 0.5 s between measurement points are shown in red, green, and blue, respectively. (b) Stabilized power output measured at 0.85 V, 0.9 V, 0.95 V and 1 V shown in red, green, blue and purple, respectively. In the inset, the SPO is plotted as a function of the set voltage point and then fit to a Gaussian curve to estimate a maximum PCE of 10.945% at 0.93 V.

Table 4.1. Effect of scan rate on photovoltaic parameters extracted from *J-V* scans.

Scan	V_{OC} (V)	J_{SC} (mA cm^{-2})	Fill factor	PCE (%)	Avg of fwd and rev scans
TD=0.01, reverse	1.182	16.32	0.699	**13.49**	10.3%
TD=0.01, forward	1.112	16.73	0.384	**7.15**	
TD=0.05, reverse	1.175	14.13	0.787	**13.07**	11.1%
TD=0.05, forward	1.153	14.78	0.537	**9.15**	
TD=0.5, reverse	1.173	13.08	0.740	**11.35**	10.8%
TD=0.5, forward	1.164	13.29	0.661	**10.23**	

Table 4.2. Stabilized power output voltage and corresponding efficiency. The "Measurement/Calculation" refers to one of three types of efficiencies listed here. SPO (meas) refers to the stabilized power output measurement in which the device is set to a constant voltage and the current is measured over 120 s. The Gaussian fit refers to the calculated maximum power in the inset of **Figure 4.2(b)**. The reverse scan MPP refers to the maximum power point calculated in the reverse scan (TD=0.5) in **Figure 4.2(a)**.

Measurement/ Calculation	Voltage (V)	PCE (%)
SPO (meas)	0.85	10.38
SPO (meas)	0.9	10.83
SPO (meas)	0.95	10.89
SPO (meas)	1	10.46
Gaussian fit of SPO data points	0.93	10.95
Reverse scan MPP (TD=0.5)	0.94	11.35

Certification. Devices certified by the National Renewable Energy Laboratory PV Performance Characterization Team were loaded into an air-free holder in a N_2-filled glovebox. Although our earlier work on $CsPbI_3$ QDSCs described in Chapter 3 yielded devices operational in ambient conditions, this was not the case for the AX-coated $CsPbI_3$ QDSCs (See Section 4.4.6 for further details). As a result, the devices were inserted into a stainless steel chamber with a glass window and without any temperature control. The device active area was illuminated through a metal aperture with an area of 0.058 cm^2, which was measured by the PV Performance Characterization Team. As an accredited PV testing facility, the PV Performance Characterization Team received and tested the packaged solar cell in accordance with their independent testing procedures.

4.4 RESULTS AND DISCUSSION

4.4.1 *Exploration of AX salt treatments for improved photovoltaic performance*

In previous work on Pb-chalcogenide QDSCs, metal halide salts, such as $CdCl_2$ and PbI_2 [68], [71], [75], [156], and molecular halides[157] have been used to improve QD coupling, passivate surfaces, tune device energetics, and improve stability of devices [71], [158]. Building on this work, we explore a variety of AX salts to improve electronic coupling in $CsPbI_3$ QDs. To fabricate the $CsPbI_3$ QD films for this work, $CsPbI_3$ QDs were synthesized as described previously [60], [147] and deposited in a layer-by-layer fashion by spin-coating from octane. To partially remove the native ligands and allow for further layers to be deposited without redispersing the existing layers, the film is immersed into a saturated $Pb(NO_3)_2$ solution in methyl acetate (MeOAc) after each QD layer.[147] After building up a sufficiently thick $CsPbI_3$ QD film (3-4 deposition cycles, leading to films 200-400 nm thick), the film was immersed in a saturated AX salt solution in ethyl acetate (EtOAc) for ~10 s. **Figure 4.3(a)** shows a flow diagram depicting this process for film assembly.

A series of solar cells with varied composition of the AX salt post-treatment, as well as a control device where only neat EtOAc is used, were fabricated and investigated to determine the role of the various A and X components as well as the structural makeup of the resulting films. **Figure 4.3(b)** compares *J-V* scans for devices with the various AX salt treatments. In comparison to the control, all of the AX salt post-treatments markedly increase the performance of the $CsPbI_3$ QDSCs, demonstrating the generality and effectiveness of this surface treatment scheme. Among the different AX salt post-treatments explored in this series, the highest PCE of 13.4% was achieved from the FAI treatment with a J_{SC} of 14.37 mA/cm^2, which was remarkably better than the neat EtOAc control with a PCE and J_{SC}, of 8.5% and 9.22 mA/cm^2, respectively. As seen in

Figure 4.3(b), the post-treatments have little impact on the V_{OC} or *FF*, the PCE improvement is almost entirely attributed to the increased J_{SC} (see **Table 3.1**).

We confirm the presence of the FAI salt in the film after the post-treatment via time-of-flight secondary ion mass spectrometry (ToF-SIMS) depth profiling as seen in **Figure 4.3(c-e)** (see Methods for description of *m/z* values assigned to ions used to track each component). Comparing the FAI-coated film (**Figure 4.3(d)**) to the control film (**Figure 4.3(c)**), the Cs, Pb, and I signals remained approximately the same while there is a significant increase in the FA signal intensity. To directly compare the Cs, I and FA, we calculate ratios of the signal intensities integrated over the thickness of the film (**Figure 4.3(e)**). The FAI-coated film has a significant increase in the FA:Pb ratio (as expected, the signal at *m/z* = 45 is at the instrument response limit before treatment) and a slight increase in the I:Pb ratio, whereas the Cs:Pb ratio is unchanged. Furthermore, the ToF-SIMS trace of the FA component indicates a higher concentration of FA^+ at the sample surface, which is corroborated by X-ray photoemission (XPS) (**Figure A.17**) confirming the presence of FA^+ on the surface. The slight increase in the I:Pb ratio is confirmed for the sample surface by XPS as well. We also identify the presence of FA^+ in the film by transmission FTIR (**Figure A.18**) from the emergence of a peak at 1712 cm^{-1} following FAI treatment which is characteristic of the C=N stretch in FA^+.

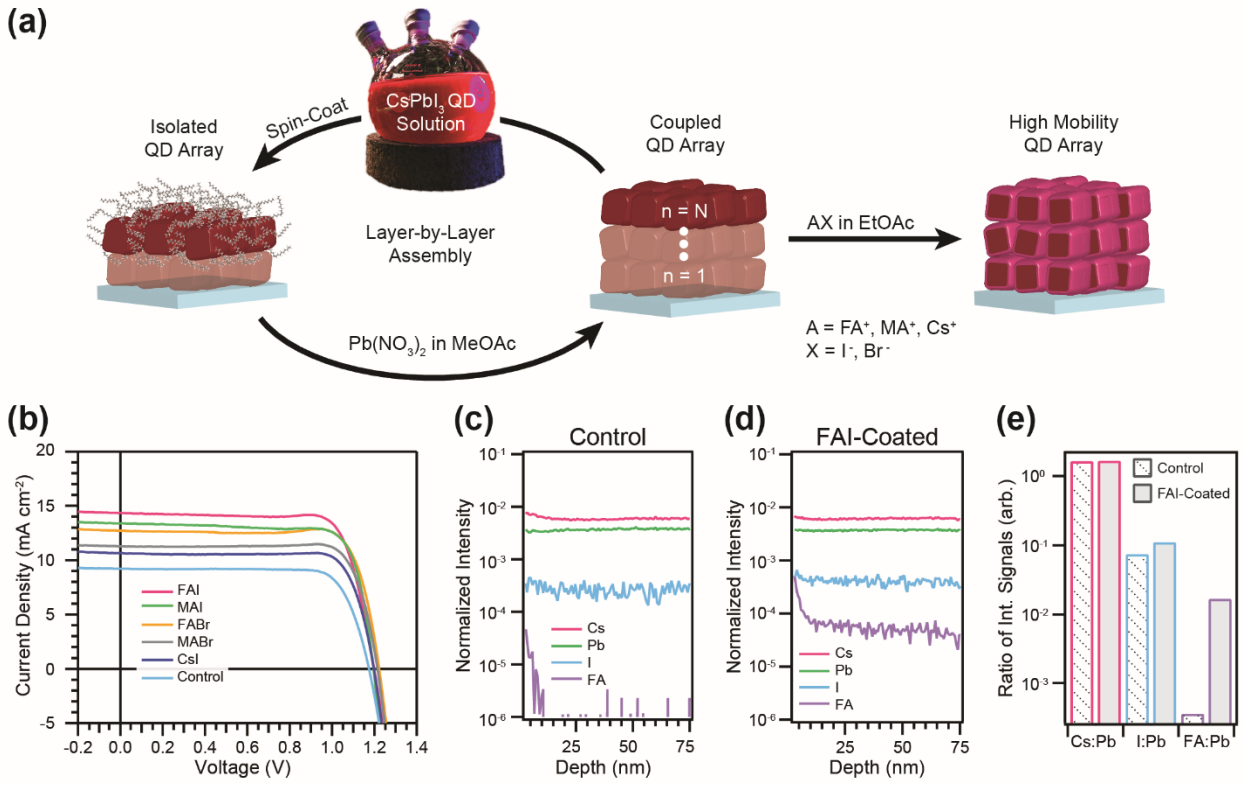

Figure 4.3. Effect of AX salts on $CsPbI_3$ QD films and photovoltaic performance. (a) Schematic of the film deposition process and AX salt post-treatment. (b) *J-V* characteristics of $CsPbI_3$ QD devices treated with FAI (pink), MAI (green), FABr (yellow), MABr (grey), CsI (dark blue) and neat EtOAc control (blue). ToF-SIMS depth profile of $CsPbI_3$ QD films (c) without and (d) with an FAI post-treatment. Intensity is normalized to total counts at each datapoint. (e) Ratios of Cs:Pb, I:Pb, and FA:Pb calculated from the integrated ToF-SIMS signal intensities throughout the film.

Table 4.3. Effect of AX salts on photovoltaic parameters extracted from *J-V* scans.

AX salt post-treatment	V_{OC} (V)	J_{SC} (mA cm^{-2})	Fill factor	PCE (%)
FAI (EtOAc)	1.20	14.37	0.78	13.4
FABr (EtOAc)	1.22	12.70	0.81	12.6
MAI (EtOAc)	1.20	13.39	0.79	12.6
MABr (EtOAc)	1.21	11.27	0.82	11.2
CsI (EtOAc)	1.20	10.64	0.81	10.3
neat EtOAc	1.17	9.22	0.78	8.5

4.4.2 *Optimization of FAI-coated $CsPbI_3$ QDSCs*

Based on the results in **Figure 4.3**, the deposition and processing conditions for the FAI treatment were optimized. Here I will describe the effect of two processing variables on the performance of the FAI-coated $CsPbI_3$ QD devices. The first variable that was optimized was the solvent used for the FAI solution. Initially, FAI in 2-propanol and FAI in MeOAc solutions were explored, borrowing from 2-step perovskite literature and our earlier $Pb(NO_3)_2$ ligand treatments in Chapter 3, respectively. In addition to 2-propanol and MeOAc, 1-propanol and EtOAc were included in the solvent study, deviating slightly from each of the original solvents. The *J-V* scans and SPO of devices fabricated with these FAI solutions and with neat 2-propanol are shown in **Figure 4.4**. As seen below, all of the devices except for the one soaked in FAI in 1-propanol solution yielded similar *J-V* scans, however the SPO reveals greater differentiation between the different treatments. (Note: Fast scans (time delay = 0.01 s) are shown in **Figure 4.4(a)**.) Comparing the SPO of the devices, FAI in EtOAc yielded the highest efficiency, followed closely by FAI in 2-propanol, and FAI in MeOAc. In contrast, neat 2-propanol and FAI in 1-propanol yielded less than half of the SPO of the other treatments indicating that the solvent can be detrimental to the performance of devices. Interestingly, the choice in solvent affects the response time as seen by the slow rise in SPO when FAI in 2-propanol and FAI in 1-propanol. On the other hand, when FAI in EtOAc or MeOAc was used, there is a flat, stable SPO immediately upon opening the shutter, which may be related to slow ion motion in the devices. Combining this slower response time with the poor performance of neat 2-propanol treated devices relative to neat EtOAc treated devices (Control device in **Figure 4.3(b)**) suggests that aprotic solvents lead to better performing devices. I speculate that this is either due to the ability of the protic solvents to dissolve the A-site cation or due to their ability to solvate the ionic ligands bound to the QD surface; however, further research

is necessary to determine the root cause. Because FAI in EtOAc yielded the highest SPO, I proceeded to optimize the FAI treatment using EtOAc. One trade-off to using EtOAc is the limited solubility of FAI compared to 2-propanol and 1-propanol, which means one fewer variable that can be tuned to optimize the process.

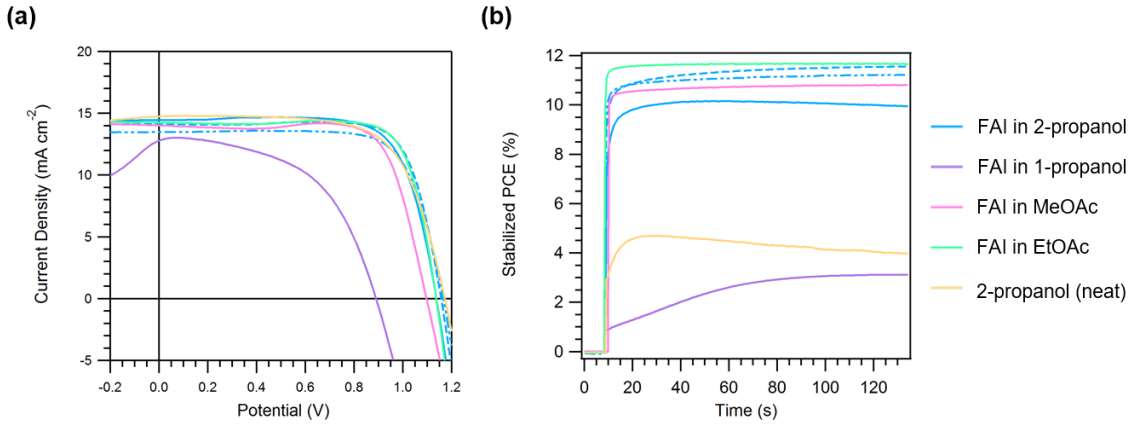

Figure 4.4. Effect of FAI solution solvent on FAI-coated $CsPbI_3$ QDSCs. (a) *J-V* scans and (b) SPO of device post-treated with a 10 s soak in FAI in 2-propanol (blue), FAI in 1-propanol (purple), FAI in MeOAc (pink), FAI in EtOAc (green) and neat 2-propanol (yellow). The dotted and solid blue lines represent 3 different FAI in 2-propanol devices.

The second processing variable I examined was the soak time used for the FAI treatment. In **Figure 4.5(a)** and **(b)**, the absorbance and PL of the $CsPbI_3$ QD films show an increasing red-shift in the optical properties with an increase in soak time, which highlights the tunability of this post-treatment method. Although a red-shift is typically associated with a decrease in bandgap, we will later show that in the first 10 s of FAI soak time, this red-shift is more likely due to enhanced QD-QD coupling. To make sure this effect is due to the FAI and not merely a solvent effect, **Figure 4.5(c)** shows that PL peak position remains unchanged after soaking the QD film in EtOAc for 10 s. In **Figure 4.5 (d)** and **(e)** the device performance peaks after soaking the QD film in FAI in EtOAc solution for 10 s. From the *J-V* scan we see an increase in J_{SC} and a decrease in *Voc* (with the exception of the control) with FAI soak time. The photovoltaic parameters extracted from the

J-V scans and the SPO are summarized in **Table 4.4**. The EQE spectra (**Figure 4.5 (f)**), however, indicate that this increase in J_{SC} does not correspond with any shift in the onset at ~700 nm, which would be indicative of a bandgap change. Thus, we speculate that this increase in J_{SC} is related to improvement in charge carrier extraction rather than generation. Further studies on the surface chemistry and the effect of the FAI soak time are currently underway and will be reported in a future publication.

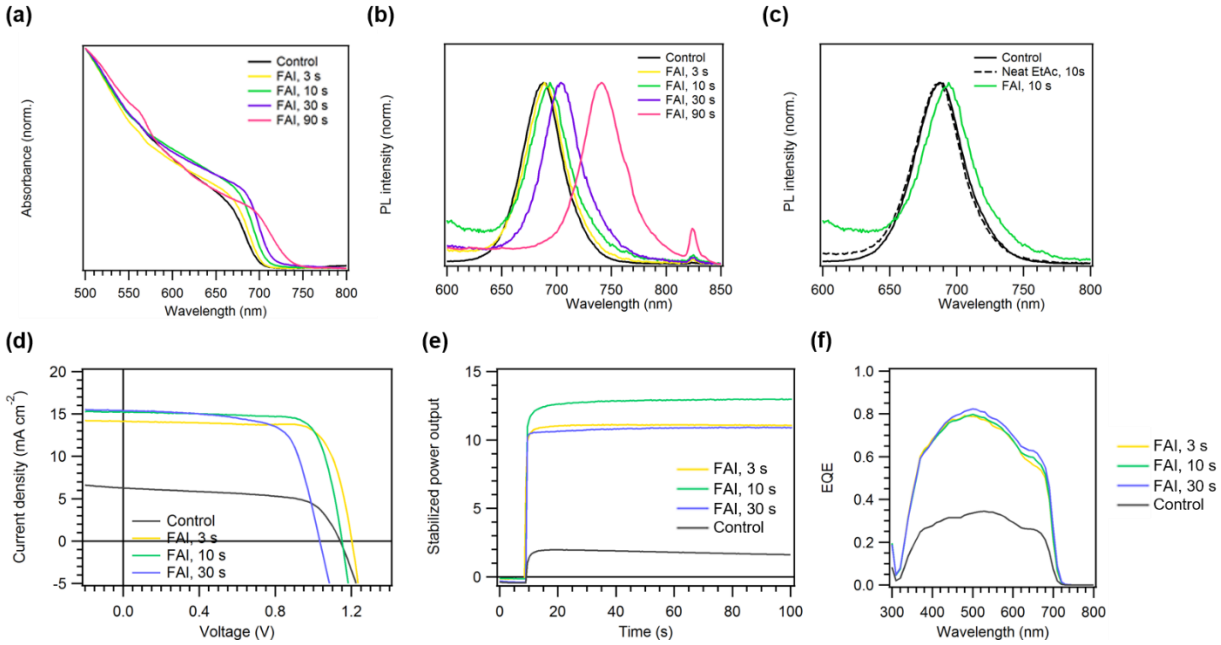

Figure 4.5. Effect of FAI soaking time on $CsPbI_3$ QD films and solar cells. (a) Absorbance normalized at 500 nm and (b) and normalized PL of $CsPbI_3$ QD films deposited on glass soaked in FAI in EtOAc solutions for 0 s (black), 3 s (yellow), 10 s (green), 30 s (purple) and 90 s (pink). (c) Normalized PL of the control (0 s soak, solid black line), neat EtOAc treated (10 s soak, dotted black line) and FAI treated (10 s soak, green) of QD films. (d) *J-V* scans, (e) SPO and (f) EQE of QDSCs soaked for 0 s (black), 3 s (yellow), 10 s (green) and 30 s (purple) in FAI in EtOAc solution.

Table 4.4. Effect of FAI soak time on photovoltaic parameters extracted from *J-V* scans and SPO.

Scan	V_{OC} (V)	J_{SC} (mA cm^{-2})	Fill factor	PCE (%)	SPO (avg. last 10 s)
Control	1.14	6.27	64.1	4.56	1.6%
FAI, 3 s	1.20	14.13	76.6	13.0	11.1%
FAI, 10 s	1.15	15.22	76.4	13.4	13.0%
FAI, 30 s	1.03	15.38	68.5	10.9	10.9%

4.4.3 *Champion FAI-coated $CsPbI_3$ QDSC certified with a record efficiency*

Our optimization process led to a champion device shown in **Figure 4.6**. Comparing the champion device treated with FAI to those treated with neat EtOAc, we see a ~60% improvement in J_{SC}, improving the PCE obtained from a *J-V* scan from 8.5% to 13.8% and improving the stabilized power output (SPO) from 6.1% to 13.5%. This photocurrent increase occurs due to a broadband improvement in the overall EQE, rather than a change in the EQE onset—which would indicate a change in the bandgap (**Figure 4.6(b)**). Moreover, the absorbance of the films using neat EtOAc and FAI treatments show similar onsets at ~700 nm, consistent with the EQE spectra, but also show similar overall light absorption (**Figure A.14**), ruling out the possibility that the improvement seen in J_{SC} arises from improved light absorption. We find a similar broadband improvement in EQE for all of the investigated AX salt post-treatments (**Figure A.15**), suggesting that this AX post-treatment scheme is a general way to improve the charge carrier collection efficiency in the $CsPbI_3$ QD films. We investigated the case of FAI in detail, however other AX salt post-treatments after optimization could yield even higher performance. In addition to an improvement in the PCE, we also observe a noticeable reduction in hysteresis between the forward (*i.e.*, J_{SC} to V_{OC}) and reverse (*i.e.*, V_{OC} to J_{SC}) *J-V* scans, as well as better agreement between the SPO and reverse *J-V* scan after the FAI post-treatment (**Figure 4.6**). Histograms of the PCE, V_{OC}, J_{SC} and FF of 78 devices fabricated with this FAI post-treatment are provided in **Figure A.16** to demonstrate the reproducibility of these high efficiency (>12%), high voltage (>1.15 V) QDSCs.

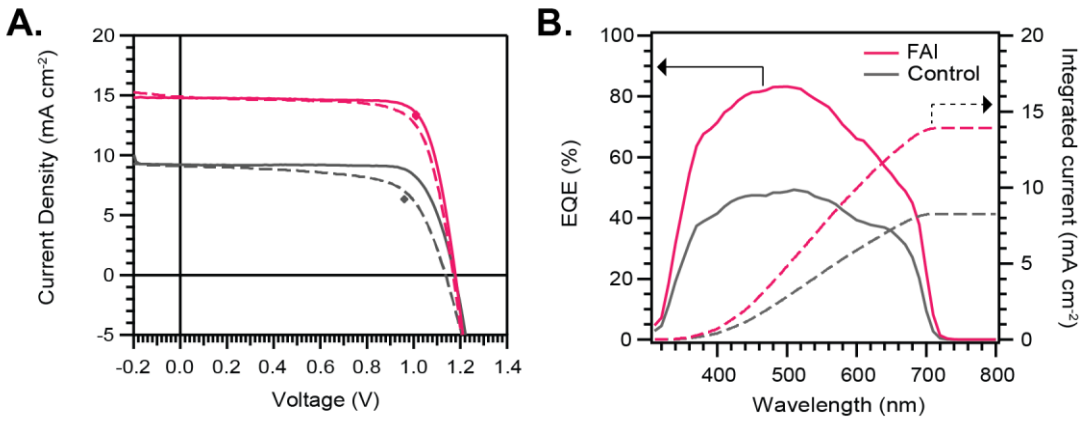

Figure 4.6. Performance of champion FAI-coated and control devices measured in our laboratory. (a) *J-V* scans in the forward (dotted) and reverse (solid) directions for FAI-coated (pink) and control (gray) devices. The SPO for each device is indicated by the diamond marker. (b) EQE (solid) and integrated current (dotted) for the FAI-coated (pink) and control (gray) devices.

Figure 4.7 show measurements performed by the National Renewable Energy Laboratory (NREL) PV Performance Characterization Team including a *J-V* scan (**Figure 4.7(c)**) for determining standard PV performance characteristics like the open circuit voltage, (V_{OC}), short circuit current density (J_{SC}), and the maximum power point. The device was held at a voltage of 0.95 V, and a measurement of the output current versus time was recorded and is shown in **Figure 4.7(d)**. Due to the hysteretic nature of perovskite solar cells [105], [155], this stabilized current output at a set voltage is used to determine the certified AM1.5G efficiency after the spectral mismatch (calculated in part from the external quantum efficiency (EQE) shown in **Figure 4.7(e)**) and device active area were determined. The stabilized current at 0.95V matches well to the reverse *J-V* scan shown in **Figure 4.7(c)** and results indicate an overall efficiency of 13.43% which is currently the highest efficiency colloidal QDSC reported to date (See **Figure 1.3**)[159].

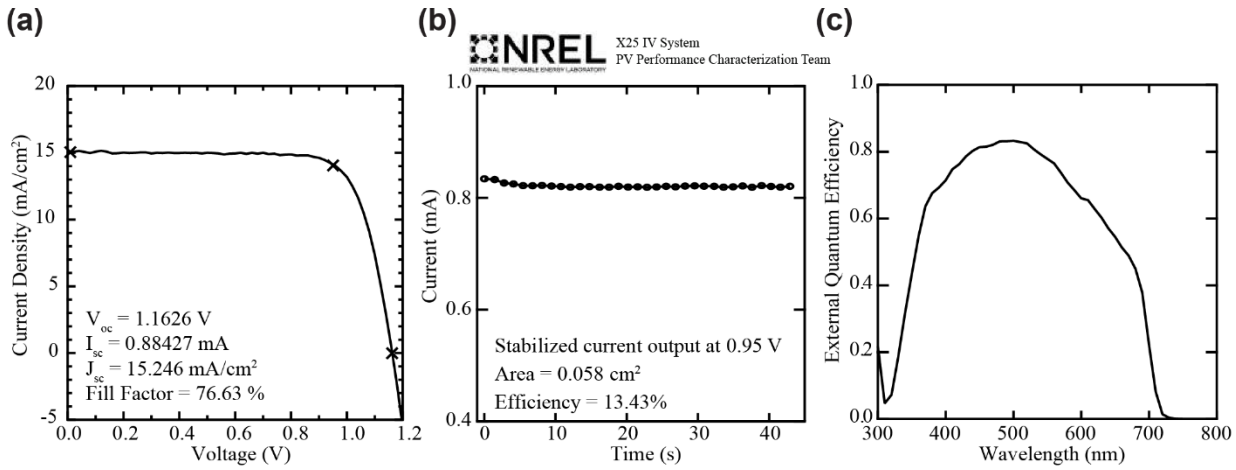

Figure 4.7. NREL certified efficiency of FAI-coated $CsPbI_3$ QDSCs. (a) J-V characteristics from forward bias to reverse bias, (b) stabilized current at a constant voltage of 0.95 V, and (c) external quantum efficiency of an encapsulated FAI-coated $CsPbI_3$ QDSC measured by the NREL PV Performance Characterization Team.

4.4.4 *Characterization of FAI-coated $CsPbI_3$ QD films*

As it is clear that FA^+ is present in the treated films, four scenarios are hypothesized regarding the interaction between FAI and the $CsPbI_3$ QD film: (i) the FAI interactions could be limited to the QD surface, either binding to the QD or infilling the void space between QDs, (ii) a partial cation exchange could result in an alloyed $Cs_xFA_{1-x}PbI_3$ QD core, (iii) a perovskite $FAPbI_3$ matrix or shell could form around the $CsPbI_3$ QDs if excess of Pb^{2+} and I^- are present, and (iv) the FAI salt could be inducing grain growth in the $CsPbI_3$ QD film, similar to the observed Ostwald ripening of $MAPbI_3$ thin films treated with MABr [160]. In scenario (iv) there would no longer be individual QDs present in the treated films and the films would resemble bulk $CsPbI_3$ or alloyed $Cs_xFA_{1-x}PbI_3$ films.

Because the EQE onset (**Figure 4.6** and **Figure A.15**) and absorption (**Figure A.14**) are effectively unchanged after FAI treatment, drastic changes to the chemical composition of the film are unlikely, as we would expect a greater red-shift in the case of a $Cs_xFA_{1-x}PbI_3$ alloying and an absorption onset at ~840 nm in the case of a $FAPbI_3$ matrix [22]. X-ray diffraction patterns before

and after the FAI treatment (**Figure A.19**) are absent of any detectable peak shifts or new peaks, which would indicate alloying or formation of a new perovskite phase, respectively. Therefore scenarios (ii) and (iii) are ruled out. Additionally, we see a decrease in the C-H modes associated with the as-synthesized oleate and oleylammonium ligands near 3000 cm^{-1} in the FTIR, suggesting additional native ligands have been removed following the FAI treatment, increasing QD coupling (scenario (i)), which is well known to induce a bathochromic shift in QD samples [161].

To assess whether the increased charge carrier collection is the result of $CsPbI_3$ QD grain growth induced by the FAI treatment (scenario (iv)), we characterized the PL from films of three different sizes of QDs which are readily synthesized by varying the reaction temperature (with lower reaction temperatures producing smaller QDs with increasing bandgap) [60], [147]. After performing the FAI treatment, there is still a significant blue shift in the spectral position of the PL peak with decreasing QD size (**Figure 4.8(a)**) compared to bulk $CsPbI_3$ which verifies that quantum confinement is retained following the FAI treatment. High resolution AFM (**Figure 4.8(b)** and **(c)**) and SEM (**Figure A.20**) images of the QD films before and after FAI treatment readily resolve individual QDs in the films and confirms the QD film morphology is maintained after FAI treatment. It should be noted that the grains shown in the AFM images in **Figure 4.8(b)** and **(c)** appear larger than those observed in SEM (**Figure A.20**) due to tip-sample convolution. Thus, we conclude that the $CsPbI_3$ QD structure remains intact, despite the addition of FA to the film. The combined evidence of absorption, EQE, PL, ToF-SIMS, FTIR, XRD, XPS, and multimodal microscopy are consistent with the addition of the FAI to the $CsPbI_3$ QD film without significant changes to the composition of the QD core. We therefore refer to the treated $CsPbI_3$ QD films as AX-coated films. A more detailed study of the interaction of the FAI treatment on the $CsPbI_3$ QD surface is forthcoming.

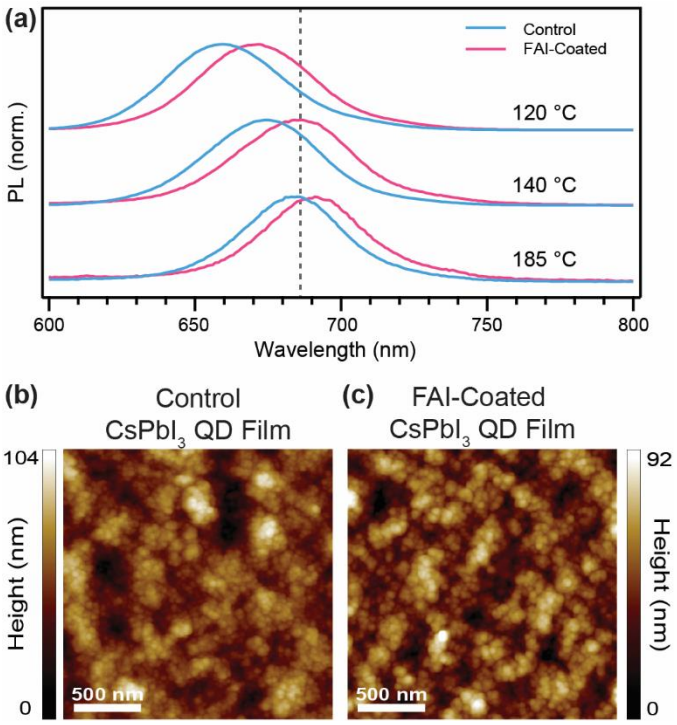

Figure 4.8. Confinement in FAI-Coated Films. (a) Normalized photoluminescence of $CsPbI_3$ QD films fabricated with three different sizes of QDs with (pink) and without (blue) FAI treatment. AFM images of $CsPbI_3$ QD films (b) without and (c) with an FAI post-treatment.

Because it is clear quantum confinement is preserved in the FAI-coated films, we hypothesize that the slight red-shift seen in the absorbance and PL following FAI treatment arises from the improved electronic coupling between individual QDs. Increasing the wavefunction overlap between neighboring QDs relaxes confinement in the QDs and improves charge carrier transport, which explains the increased photocurrent following AX-coating. We therefore probed the mobility of FAI-coated $CsPbI_3$ QD films using time-resolved terahertz spectroscopy, which is a contactless pump-probe optical method capable of characterizing both conductivity and carrier dynamics in semiconductor films. In addition to the $CsPbI_3$ QD films, we also probed $MAPbI_3$ thin films as well as PbSe and PbS QD films to compare $CsPbI_3$ QDs with more heavily studied materials [162]–[165]. The PbS QD sample was composed of 3 nm QDs utilized commonly in

literature for high efficiency QDSCs, whereas larger PbSe QDs (>6 nm) were chosen for their higher reported mobility [163].

4.4.5 *Enhanced mobility of FAI-coated $CsPbI_3$ QD films*

The time-resolved THz spectroscopy (TRTS) measurements were performed under identical conditions for a 3 nm PbS QD film, a 6 nm PbSe QD film, a $CsPbI_3$ QD film, an FAI-coated $CsPbI_3$ QD film and a $MAPbI_3$ film. For thin films, conductivity is directly proportional to the change in THz transmission [153]. **Figure 4.9(a)** shows the time-resolved change in THz transmission ($\Delta E/E$) for each of the films probed. Mobility and lifetime values were extracted from the traces in **Figure 4.9(b)** as described in the methods section and summarized in **Figure 4.9(c)** and **Figure 4.9(d)**, respectively. We find that the mobility for the control $CsPbI_3$ QD film is 0.23 $cm^2V^{-1}s^{-1}$, already significantly higher than that of the lead chalcogenide QD films (mobility of PbS and PbSe QD films were measured to be 0.042 and 0.090 $cm^2V^{-1}s^{-1}$ respectively). When the $CsPbI_3$ QD films are treated with FAI, the mobility improves from 0.23 to 0.50 $cm^2V^{-1}s^{-1}$. The mobility reaches a factor of 5 lower than the $MAPbI_3$ thin film (2.3 $cm^2V^{-1}s^{-1}$ in this study, similar to other literature reports) [165]. We also compare the carrier lifetimes that are extracted from the THz measurements. The lifetimes of the control $CsPbI_3$ and FAI-coated $CsPbI_3$ QD films were found to be 1.8 ns and 1.6 ns, respectively (neglecting the early sub 50 ps dynamics), largely similar to the 2.2 ns lifetime of the $MAPbI_3$ film. The dynamics for the PbS and PbSe QD films are quite distinct. At the earliest times the response decays rapidly; however, this is likely not recombination of carriers but rather a reduction in carrier mobility as carriers find lower energy states with lower carrier mobility. After this initial decay the mobility is reduced by another order of magnitude and we find the mobility to be ~ 0.003 $cm^2V^{-1}s^{-1}$, which falls in-line with other widely reported measurements of the carrier mobility in these QD films [162]–[164].

It is interesting to note that the carrier dynamics extracted with THz spectroscopy for both $CsPbI_3$ QD films are more similar to $MAPbI_3$ than PbS and PbSe carrier dynamics. This finding strongly suggests that the carrier transport mechanism is quite distinct in perovskite QD films compared to lead chalcogenide QD films. More work is underway exploring observed differences to understand their microscopic origins. For PV applications, mobility-lifetime product is of particular interest due to its relation to charge carrier diffusion length. The mobility-lifetime product was larger for the FAI-coated $CsPbI_3$ QD film compared to the untreated $CsPbI_3$ QD film (**Figure A.21**), and justifies the enhanced charge extraction. Time-resolved photoluminescence measurements (**Figure A.22**) show an increase in PL lifetime for FAI-coated films on a longer timescale than what is measured using THz spectroscopy, while the decay dynamics within the THz window are similar.

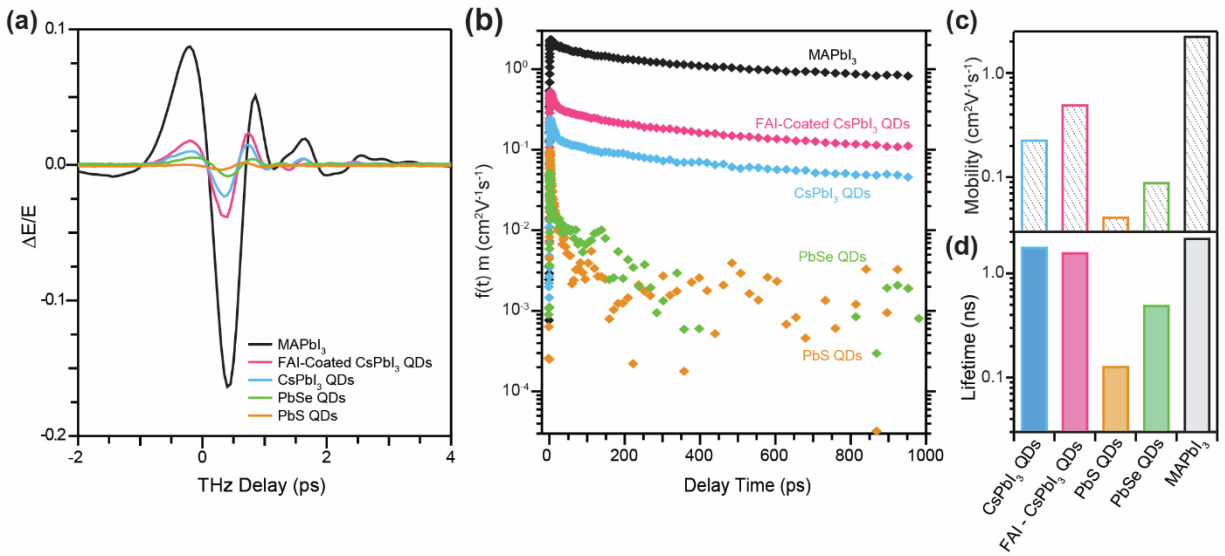

Figure 4.9. Improved mobility with FAI coating. **(a)** Time domain THz pulses through each of the films described in the text recorded at a pump delay time of ~1ps. **(b)** Time-resolved THz photoconductivity measurements of films of $CsPbI_3$ control sample (blue) compared to the FAI-coated $CsPbI_3$ QD films (pink) along with a traditional $MAPbI_3$ (black) thin film and films of 8 nm PbSe QDs (orange) and 3 nm PbS QDs (green). Comparison of the extracted mobility **(c)** and THz lifetimes **(d)** for each of the films.

4.4.6 *Stability of FAI-coated $CsPbI_3$ QDs*

Although stability was not the focus of this work, we conducted some preliminary operational stability measurements. First, it was observed that after implementing the FAI-treatment our devices were inoperable in ambient conditions. Unlike the $CsPbI_3$ QDSCs fabricated in Chapter 3 which yielded similar *J-V* scans when taken in a glovebox or in ambient laboratory conditions, the FAI-coated $CsPbI_3$ QDSCs saw a dramatic loss in *FF* upon photocurrent measurement in air as seen in **Figure 4.10**. Notably, using EtOAc as a solvent for the $Pb(NO_3)_2$ partial ligand removal did not induce the same loss in *FF*, nor did using an alternative inorganic AX salt, RbI. This suggests that there is something unique to the FAI chemistry that causes this behavior. Interestingly, the effect is reversible as retesting the same device in a N_2-filled glovebox yields more typical *J-V* characteristics with efficiencies in the >10% range. This odd phenomenon warrants further investigation as to the root cause of this reversible depleted *FF*.

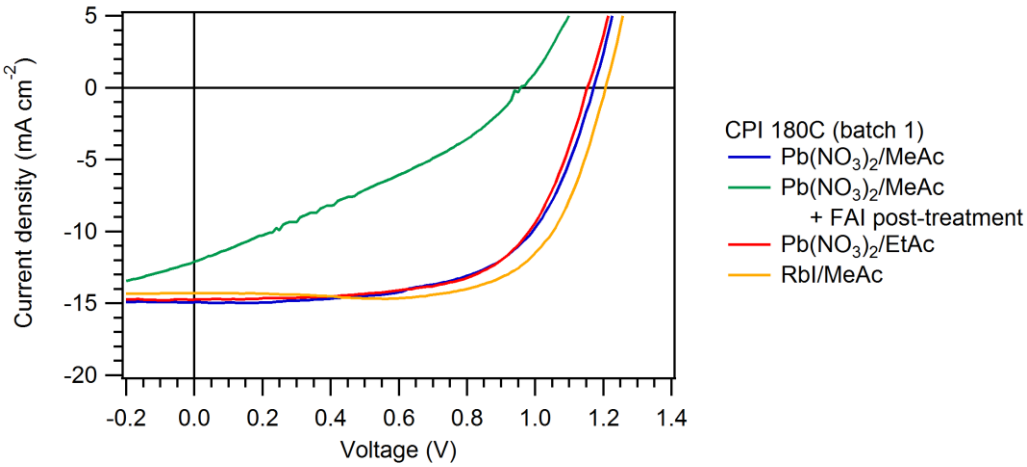

Figure 4.10. Ambient laboratory *J-V* scans of different $CsPbI_3$ QD devices. Reverse *J-V* scans of a control $Pb(NO_3)_2$ in MeOAc device (blue), FAI-treated $Pb(NO_3)_2$ in MeOAc device (green), a $Pb(NO_3)_2$ in EtOAc device (red) and a RbI in MeOAc device.

From an engineering perspective, one solution is to develop encapsulation schemes. For the purposes of NREL certification, an air-free holder was implemented. However, this can limit the

maximum achievable efficiency due to a glass window that introduces additional reflection losses, as well as the inability for temperature control, which can be detrimental to the *Voc* and also cause thermal degradation of the perovskite or HTL layers. Therefore, we also developed a method to encapsulate the device with a polyisobutylene (PIB) edge seal and a cover glass on the metal electrode side of the device stack. Using an encapsulated cell, we measured the *J-V* characteristics and the SPO for 30 min as shown in **Figure 4.11**. First, we see the reverse *J-V* scan yielded an efficiency ~12.5% without the depleted *FF* seen in the unencapsulated devices. Second, after an initial drop within the first 60 s, we see the SPO remain virtual constant at ~12% over the remaining 29 min of measurement, which is in good agreement of the reverse *J-V* scan. This preliminary stability data is encouraging and suggests that despite reversible photo oxidation effects, the FAI-coated $CsPbI_3$ QD active layer may prove to be a viable candidate in inert environments. This suggests that robust encapsulants may be sufficient to achieve overall device durability, or that further exploration in alternative ligand exchanges can be investigated for greater intrinsic durability.

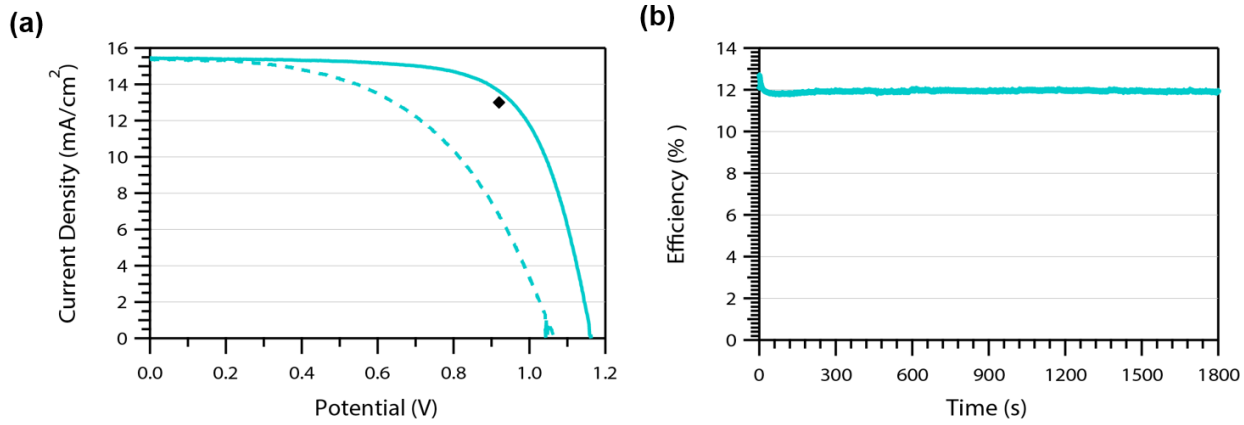

Figure 4.11. *J-V* scans and operational stability of an encapsulated FAI-coated $CsPbI_3$ QDSC. **(a)** *J-V* scans in the forward (dotted) and reverse (solid) directions. SPO is represented by the black diamond. **(b)** SPO of the encapsulated cell measured for 30 min.

4.5 Conclusions and Outlook

While QDs have the advantages of widely tunable bandgap and energetic position, and in the case of $CsPbI_3$ offer the added benefit of phase stability, QDSCs have traditionally suffered from both low V_{OC} relative to their bandgap and poor carrier collection. We demonstrate that both of these disadvantages of QDSCs can be, in large part, overcome by the coupling of $CsPbI_3$ QD films. The AX treatment strategy developed in this work yields a doubling of the already high mobility of $CsPbI_3$ QD films and results in a certified record PCE of 13.43%, positioning QDSCs above the best reported PCE for dye-sensitized solar cells, organic photovoltaics, and CZTSSe PV technologies. Additionally, the high V_{OC}, exceeding 80% of the Shockley-Queisser limit, and tunability of the bandgap make these devices well suited for use in high efficiency tandem solar cell architectures.

There are still many open questions to explore beyond this study. Although we found the FAI treatment worked the best among the AX salts we investigated in this current study, there are still open questions about whether the other AX salt treatments could be optimized further or whether expanding our library of salt treatments could improve the performance further. Understanding more about the surface chemistry and the role of the FAI treatment can provide insight into how to better tailor the ligand treatments we use. A series of DRIFTS and NMR studies have recently been conducted alongside XPS and XAS studies that verify our claims that the FAI initially acts as QD coating at limited soak times ($\leq$10 s), but then reveals that after longer soak times ($\geq$ 30 s) the QD films begin to observe alloyed $Cs_xFA_{1-x}PbI_3$ character. In addition, we are beginning to unravel different ligand exchange mechanisms that occur during the $Pb(NO_3)_2$ exchange and the FAI post-treatment, which seems to indicate each treatment can specifically target a ligand for removal. The ligand removed, however, must be exchanged with a robust

replacement ligand or else the QDs can agglomerate – thus, reducing the surface energy of the NCs and enabling conversion to the orthorhombic phase. Other strategies to retain the nanocrystalline character can be investigated such as atomic layer deposition infilling with a metal oxide matrix material [142] or embedding QDs in a durable polymer matrix [166].

In addition to improving photovoltaic performance, stability remains a key issue. We presented preliminary ambient and operational stability of the FAI-coated $CsPbI_3$ QD solar cells and observed promising operational stability in inert environments, but a peculiar reversible photo oxidation effect when the devices were measured in ambient. This raises questions about the root cause of the depleted *FF* and why it occurs specifically when the FAI treatment is used. This also suggests that further investigation in other ligand treatments could lead to more stable, and possibly equally efficient devices.

Chapter 5. CONCLUSIONS AND FUTURE OUTLOOK

5.1 SUMMARY OF WORK

The emergence of lead halide perovskite materials has revolutionized PV research and shifted the paradigm for solution-processable solar cells. With research cell efficiencies now rivaling those of more established technologies, stability and scalability remain as the major barriers to commercialization. Device durability is affected by several different aspects of the device including the stability of the photoactive layer, the stability of other layers within the devices stack, the interaction between layers, as well as the environmental and operating conditions. The selection and interfaces of the layers in the device stack need to enable high power conversion efficiency and operational stability. Scalability, on the other hand, is affected by the crystallization of the perovskite film and the need for both high quality crystal formation and uniform film coverage. One way to address this issue is to decouple crystal growth from film deposition as enabled by technologies like colloidal nanocrystals. The continued development of stable perovskite device architectures and novel photoactive layers are of great interest and importance to fueling a new clean energy future.

In Chapter 2, the lifetime of $MAPbI_3$ solar cells are first characterized under constant operating conditions using standardized stability testing protocols. We find that the choice in the electrode material has a significant impact on the device lifetime. MoO_x/Al electrodes with a thin 15 nm layer of MoO_x yielded the most stable device structure, while also delivering comparable initial PCE. This enhanced stability is due to the formation of alumina oxides at the MoO_x/Al interface, which provides a protective barrier. It remains an open question, however, whether this barrier protects the ingress of atmospheric molecules, such as H_2O and O_2, or if it protects the

migration of ions in the device stack, such as I^- or Li^+ ions migrating to the electrode. Further work on stable perovskite active layers and device architectures using rigorous constant operating stability testing is still needed. Other areas of research that remain outside of the scope of this work include the effects of the transparent conductor, the electron-transport layer, the hole-transport layer, and various encapsulation schemes on durability remain open questions in the field.

In Chapter 3, we used $CsPbI_3$ QDs as a compositionally-stable alternative to $MAPbI_3$ in efficient PV devices. Previously, thin film $CsPbI_3$ demonstrated poor ambient, room temperature phase stability due to the relatively small size of Cs^+. To overcome this phase stability issues, we leveraged the surface energy of nanocrystals to stabilize $CsPbI_3$ in the desirable cubic perovskite phase at room temperature. In order to fabricate efficient $CsPbI_3$ QDSCs, we developed both a purification method to maintain colloidal stability, and a film deposition method that yielded electronically-coupled QD films. We demonstrated the first $CsPbX_3$ QD solar cells and the most efficient all inorganic $CsPbX_3$ solar cell at the time of publication. The $Pb(NO_3)_2$ ligand exchange procedure enabled coupled QD films and resulted in a scan PCE of 10.77% and a stabilized power output of 7.9 mW cm^{-2}. We also characterized the thermal stability of drop-casted $CsPbI_3$ QD films, which maintained the cubic perovskite phase up to ~210 °C. This suggests that greater phase stability could be achieved through the development of more robust ligand shells or matrices. Exploration into increased coverage of durable inorganic ligands or infilling the QD film with metal oxides or robust polymeric materials could pave the way to more phase stable $CsPbI_3$ QD films.

In Chapter 4, we improved the photovoltaic performance of $CsPbI_3$ QDSCs by modifying the surface chemistry between QDs, which increased the film mobility two-fold. By applying an A-site cation halide (AX) salt post-treatment to the previously demonstrated $Pb(NO_3)_2$-treated QD

films, we were able to alter the $CsPbI_3$ QD surfaces, without changing the nanocrystalline character of the film. Thus, we maintained the surface energy required to stabilize the cubic perovskite phase and preserve quantum confinement in the QD films. We explored the effect of several different AX salts, including FAI, FABr, MAI, MABr and CsI, and demonstrated improved PV performance for all treatments. The greatest enhancement was observed from the FAI treatment, which we then optimized to achieve an NREL-certified solar cell efficiency of 13.43% -- a QDCS record on the NREL Best Research Cell Efficiency Chart. Time-resolved terahertz spectroscopy of the control $CsPbI_3$ QD film and the FAI-coated $CsPbI_3$ QD film reveal the improved performance stems from a two-fold enhancement in mobility. We are currently conducting studies to better understand the surface chemistry of the $CsPbI_3$ QDs and the role of both the $Pb(NO_3)_2$ and the FAI treatments. Better understanding of the role of each of these treatments can lead to more target ligand removal and exchange, which can further enhance photovoltaic performance. There are also open questions regarding the effect of the FAI treatment on the film stability. Illumination in ambient conditions causes a reversible decrease in the *FF* of PV devices, but the underlying mechanism is unclear. Although the encapsulated FAI-coated $CsPbI_3$ QD demonstrated promising operational stability, it is still preferred to develop materials with high ambient stability. Therefore, further exploration into other ligand treatments that both improve mobility and maintain ambient stability should be conducted.

5.2 FUTURE OUTLOOK AND APPLICATIONS

The results presented in this dissertation paint a promising future for perovskite and perovskite QD solar cells. The possibilities for future applications and research directions are endless; but I will highlight a few next steps in this section.

In Chapter 2, we demonstrated that the enhanced stability imparted by MoO_x/Al electrodes is due to the formation of Al oxides at the MoO_x/Al interface. It is unclear whether this Al oxide layer is a barrier to prevent external agents, such as water and oxygen, from entering the device stack, or prevents internal agents from within the device stack, such as I^- and Li^+, from leaving with the potential to react with the top metal electrode. Previous work on encapsulants developed by the existing solar industry can protect perovskite devices from external agents, however the mitigation of ion migration from within the device stack is unique to this material. Thus, further exploration into materials that prevent ion migration between device layers are currently underway and are likely to play a significant role in improving the operation stability. Some examples that have already been demonstrated is replacing spiro-OMeTAD with a substitute HTL, which does not require a Li dopant and using PCBM as an ETL, which helps getter the I^-. Other approaches to minimize ion migration may be the inclusion of thin Al oxides, polymers, or self-assembled monolayers, to act as barriers within the device layer stack. More generally, this work points toward the necessity of examining the stability of each layer in the device stack and questioning conventional wisdom of which materials are the most stable choices.

In Chapters 3 and 4, we developed high efficiency $CsPbI_3$ QD solar cells, which can pave the way for several different applications. First, the tunable bandgap range from 1.75-2.13 eV, is ideal for a top cell of a tandem solar cell. In particular, we demonstrated a low *Voc* deficit relative to the bandgap of the material, which is a key feature of the best III-V multijunction solar cells. The room temperature deposition processes also enable a wide range of thermally-limited bottom cell materials, including organic-inorganic perovskite for an all perovskite multijunction solar cell. Second, the lower end of the bandgap range is ideal for pure red emission. This is desirable for light-emitting diodes, and potentially for lasers as well. The enhanced electronic coupling that we

have demonstrated within these QD films can also enable more work in electrically-driven, as opposed to optically-pumped, devices. Finally the ability to deposit perovskite QDs on either other perovskite QD films of different size or composition, or on perovskite thin films can enable the exploration of heterostructures. Heterostructures can be beneficial to controlling internal electric fields within the device active layer or for providing barrier for charges flowing in the opposite direction. However, such a design requires careful band alignment and control. Thus, further exploration on the effect of different ligand treatments on the fermi level of the material would be necessary to successfully implement these designs. Overall, this materials has only recently been explored and many open questions remains. From studies of fundamental properties, to the implementation in novel device structures, or the large-scale manufacturing of photovoltaics, there are endless possibilities for the exploration and future impact of these perovskite QD materials.

Appendix A. SUPPORTING INFORMATION

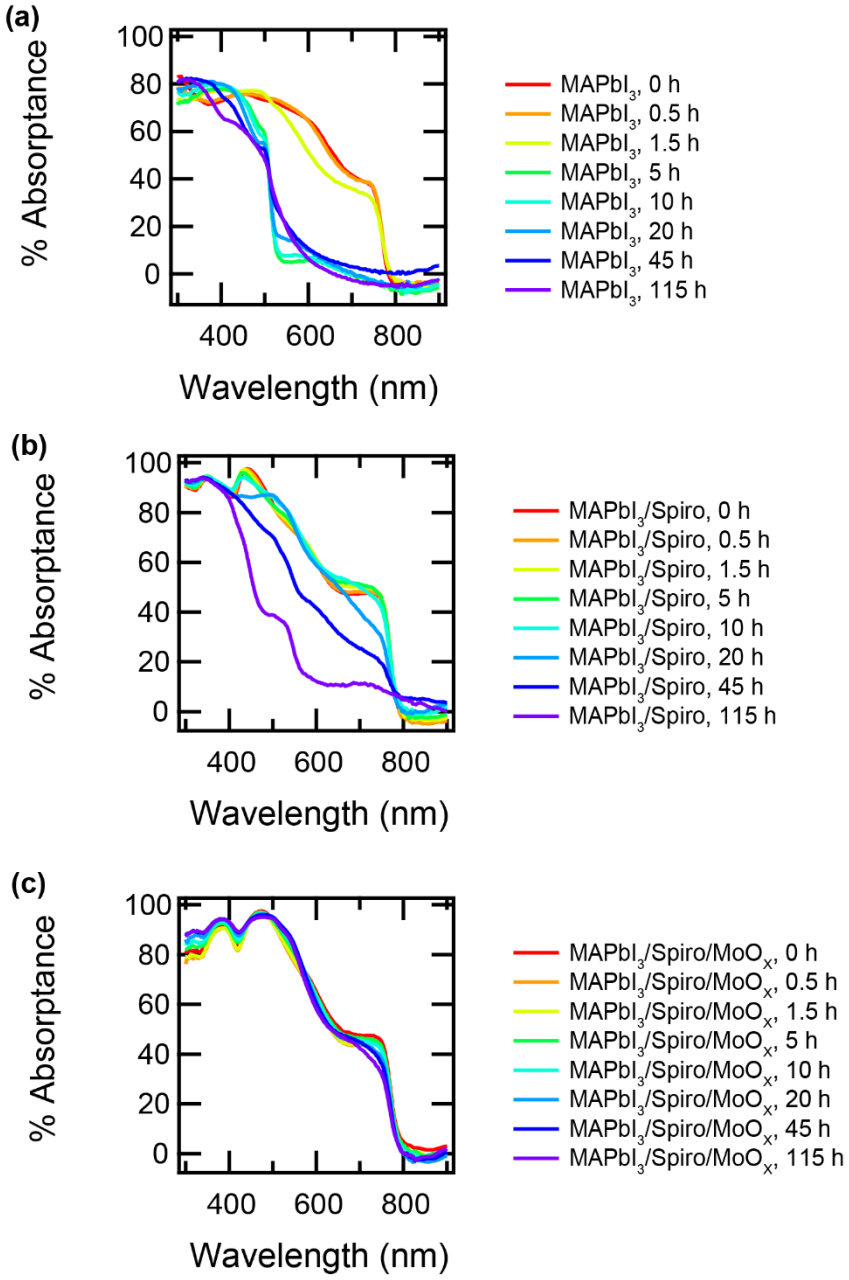

Figure A.1. Absorptance spectra of (a) $MAPbI_3$ films, (b) $MAPbI_3$/Spiro-OMeTAD films, and (c) $MAPbI_3$/Spiro-OMeTAD/15nm MoO_x films on glass/TiO_2 substrates with increasing illumination exposure. Photodegradation studies were conducted in laboratory ambient and constant illumination from a tungsten-halogen light source with an intensity calibrated to ~1-sun flux.

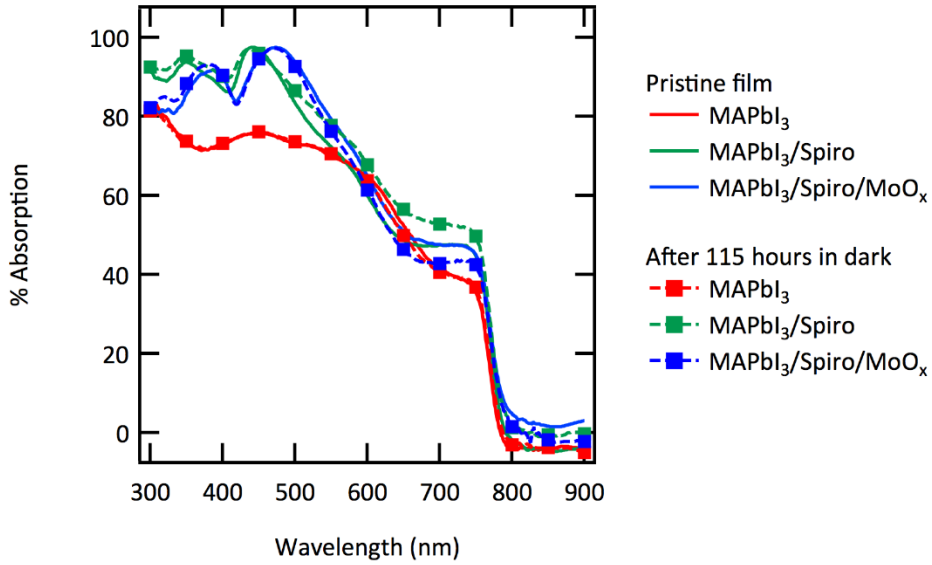

Figure A.2. Absorption spectra of $MAPbI_3$ films, $MAPbI_3$/Spiro-OMeTAD films, and $MAPbI_3$/Spiro-OMeTAD/15nm MoO_x films on glass/TiO_2 substrates before (solid lines) and after (dotted lines with square markers) 115 h of storage in dark under laboratory ambient conditions. Compared to the illuminated samples, there was little or no difference in the absorption spectra after 115 h of storage in dark.

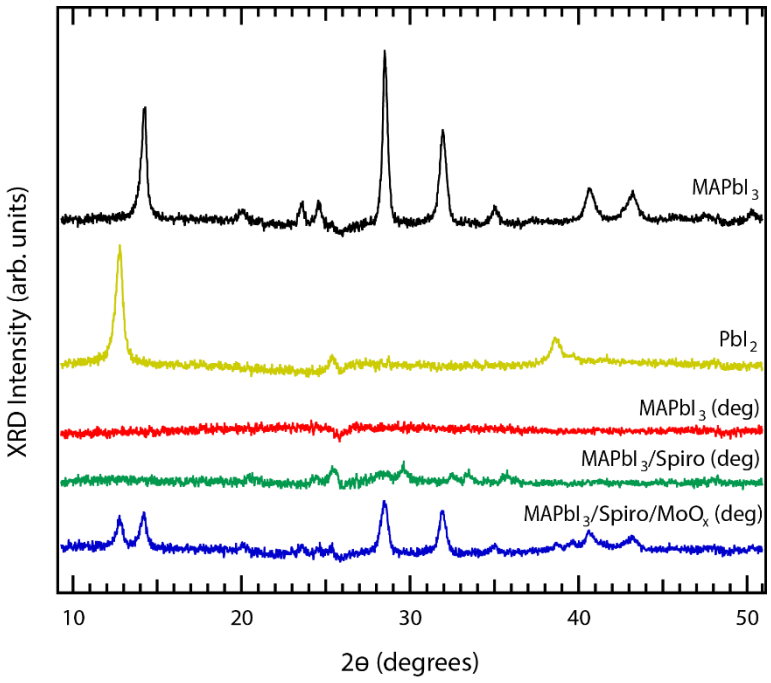

Figure A.3. X-ray diffraction scans of $MAPbI_3$ (black), PbI_2 (yellow), $MAPbI_3$ after 115 h of illumination (red), $MAPbI_3$/Spiro-OMeTAD after 115 h of illumination (green), and $MAPbI_3$/Spiro-OMeTAD/MoO_x (blue) after 115 h of illumination. The

scans were corrected by a glass/TiO_2 baseline. XRD patterns were obtained using a Bruker D8 Discover diffractometer using Cu Kα radiation and a 2D area detector.

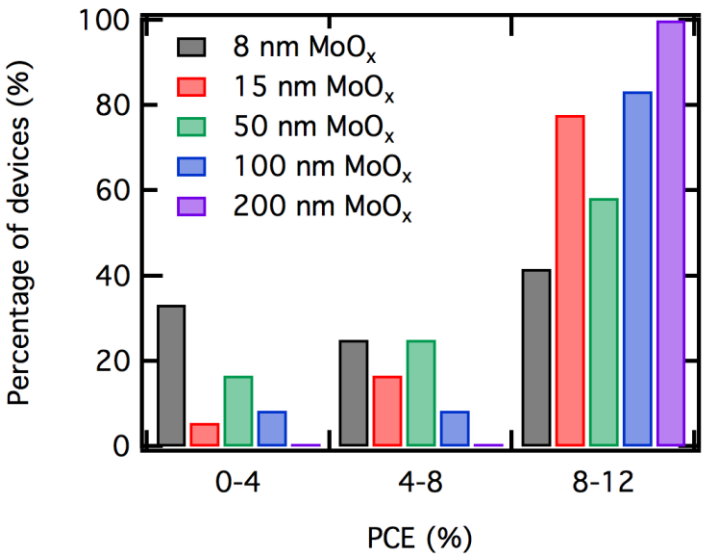

Figure A.4. A normalized histogram of the power conversion efficiencies (PCE) achieved by devices with varying MoO_x thicknesses in the MoO_x/Al electrode. The thin, 8 nm MoO_x devices have the highest percentage of devices with a PCE <4%, and also have the lowest percentage of devices with PCE ≥ 8%. The even distribution across the full range of PCE suggests poor reproducibility due to the exceedingly thin MoO_x interlayer.

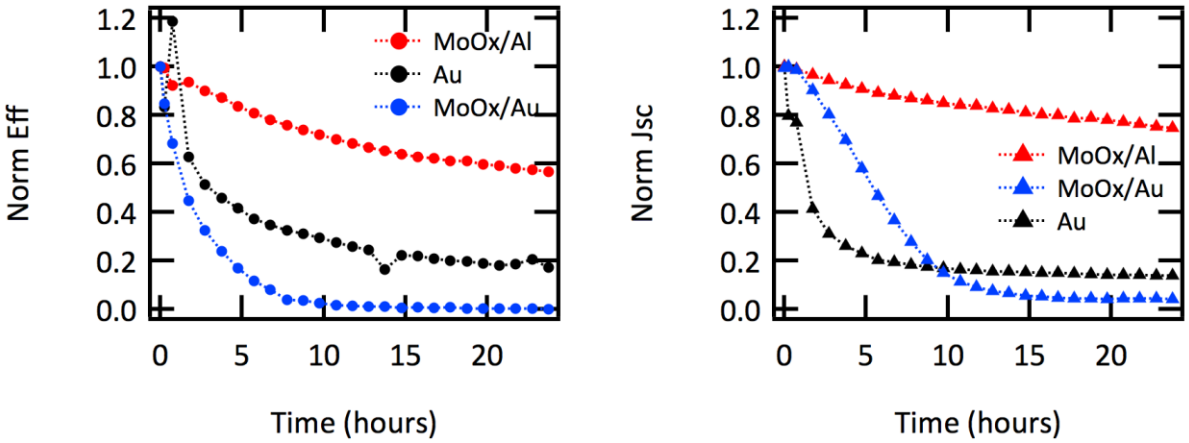

Figure A.5. The normalized PCE and normalized *Jsc* of select devices with Au, MoO_x/Au, and MoO_x/Al electrodes over 24 h of constant operation in ambient. The relative humidity during this testing period was 51.5±1.5%.

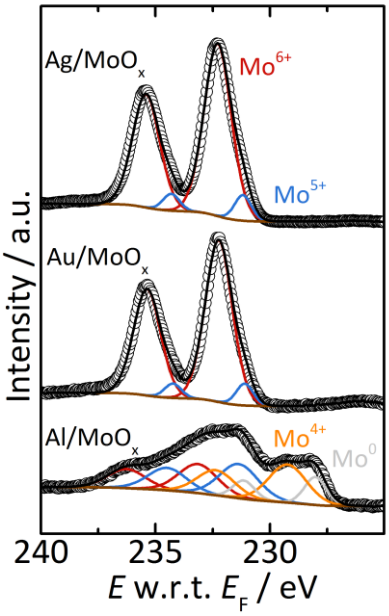

Figure A.6. XPS core-level spectra of thin (5 nm) metal layers on glass/ITO/MoO_3(15 nm). The deposition of Ag and Au does not impact the chemical composition of the MoO_x layer underneath which is determined to be in a slightly substoichiometric MoO_3 phase. In contrast, evaporation of Al on top leads to a pronounced reduction of the MoO_3 to MoO_2, as seen by the appearance of an Mo^{4+} feature, and to plain metallic molybdenum.

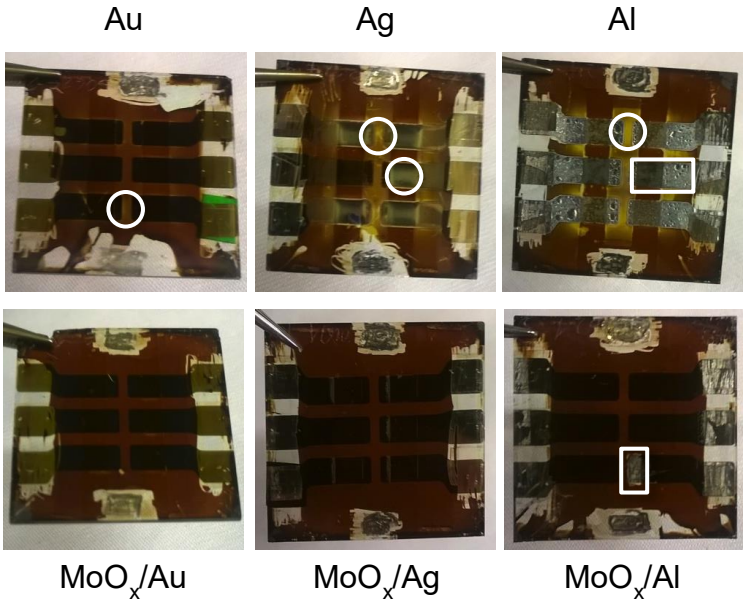

Figure A.7. Enlarged optical images in **Figure 2.7** with examples of $MAPbI_3$ yellowing and areas of transparency highlighted with white circles and squares, respectively. $MAPbI_3$ yellowing is seen in the devices without MoO_x interlayer,

although significantly less yellowing occurs in devices with Au electrodes. Devices with Ag show the most yellowing, with yellow areas both within and outside of the device active area. Both the Al and MoO_x/Al devices show areas of transparency that are not evident in the other electrode configurations. We speculate that this may be due to a reaction between $MAPbI_3$ and Al. The images of these devices were taken from the glass side after 24 h of constant operation in ~52% relative humidity.

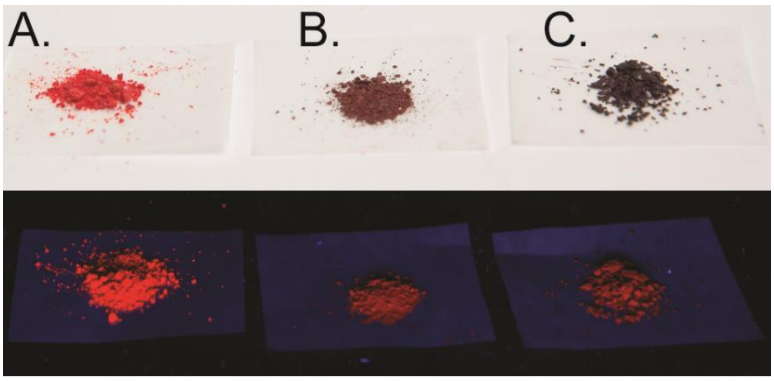

Figure A.8. Luminescent $CsPbI_3$ QD powders. Photographs under room light (top) and UV illumination (bottom) of $CsPbI_3$ QD powders synthesized at (A) 130, (B) 150, and (C) 180 °C.

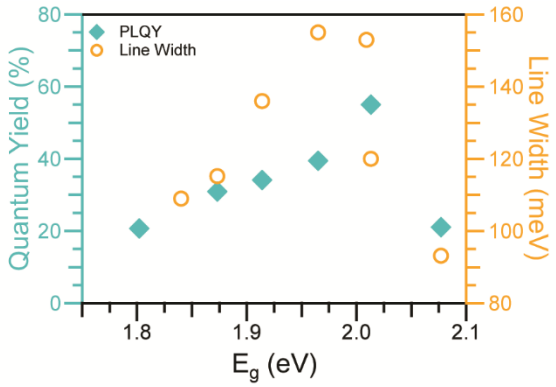

Figure A.9. FWHM and Photoluminescence Quantum Yield. PL quantum yield (blue diamonds, left ordinate) and PL line width (orange circles, right ordinate) with varying QD size/bandgap (E_g).

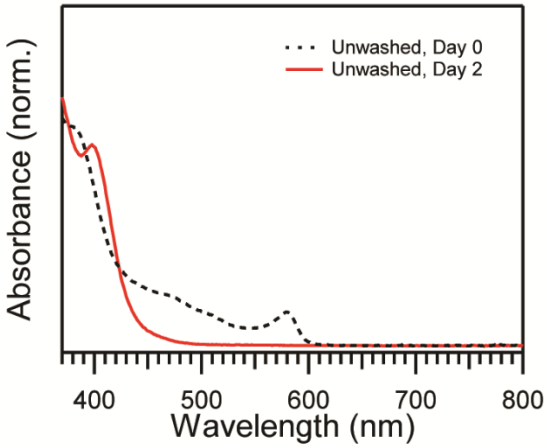

Figure A.10. Poor stability of unwashed QDs. Ultraviolet-visible absorption spectra of QDs synthesized at 60 °C and stored in ambient conditions without washing (separating QDs from unreacted precursors) for 2 days.

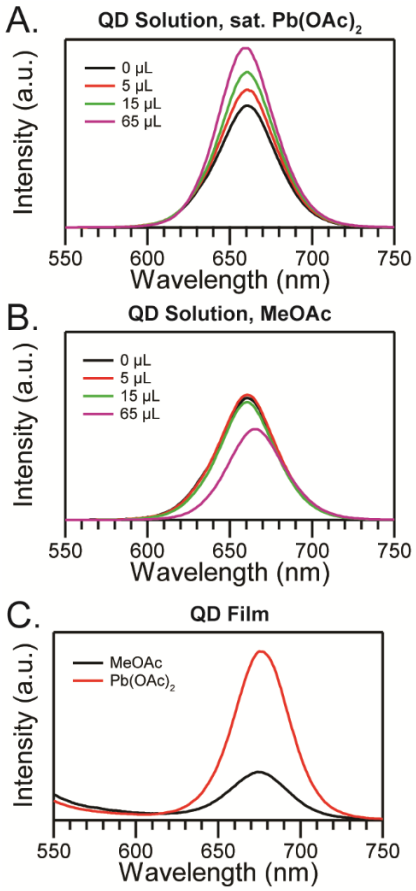

Figure A.11. Effects of $Pb(OAc)_2$ treatment on photoluminescence. Photoluminescence of 3 mL of ~3.6 µg/mL in hexane, synthesized at 180 °C, upon the addition of (**A**) a saturated solution of $Pb(OAc)_2$ in MeOAc, and (**B**) neat MeOAc. (**C**) Photoluminescence of a QD film dip-coated in neat MeOAc (black) and MeOAc saturated with $Pb(OAc)_2$ (red).

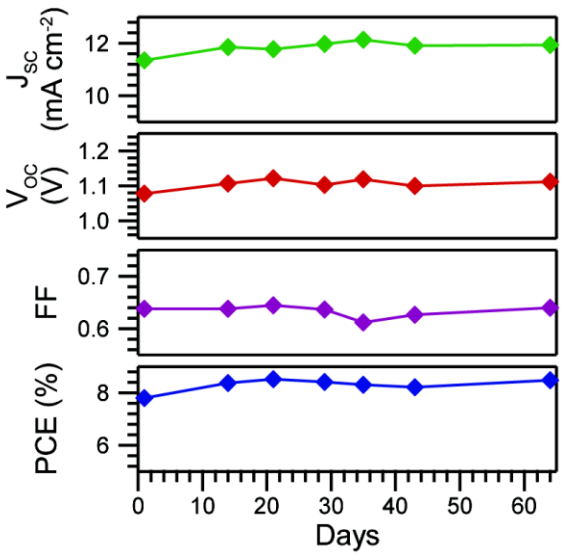

Figure A.12. Device performance characteristics over longer time scales. A typical device was periodically measured over a 64 day time period. Performance parameters were extracted from a 1 V/s voltage sweep from forward bias to short-circuit. Between measurements the device was stored in the dark in a desiccator.

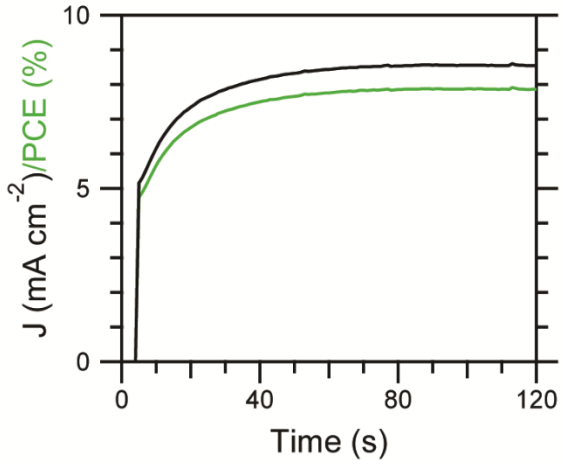

Figure A.13. Stabilized power output at constant voltage. Measured current response (black) of the device shown in Fig. 4 over 120 s when held at a constant voltage of 0.92 V. The corresponding stabilized power output is shown in green.

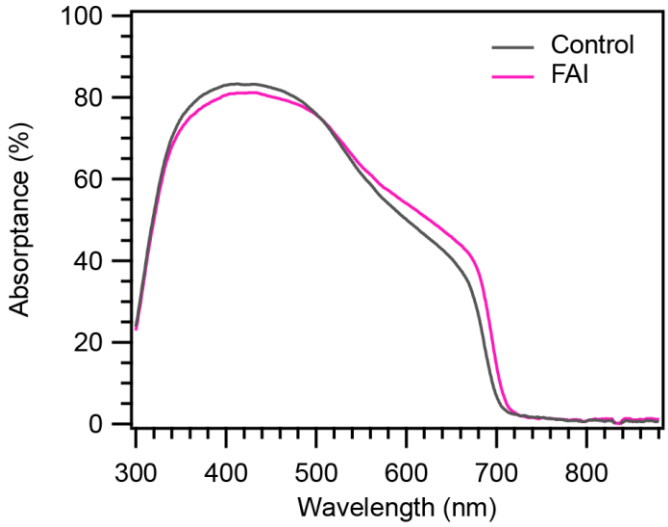

Figure A.14. Light absorption following FAI post-treatment. Absorptance spectra of $CsPbI_3$ QD films on glass with (pink) and without (gray) the FAI post-treatment.

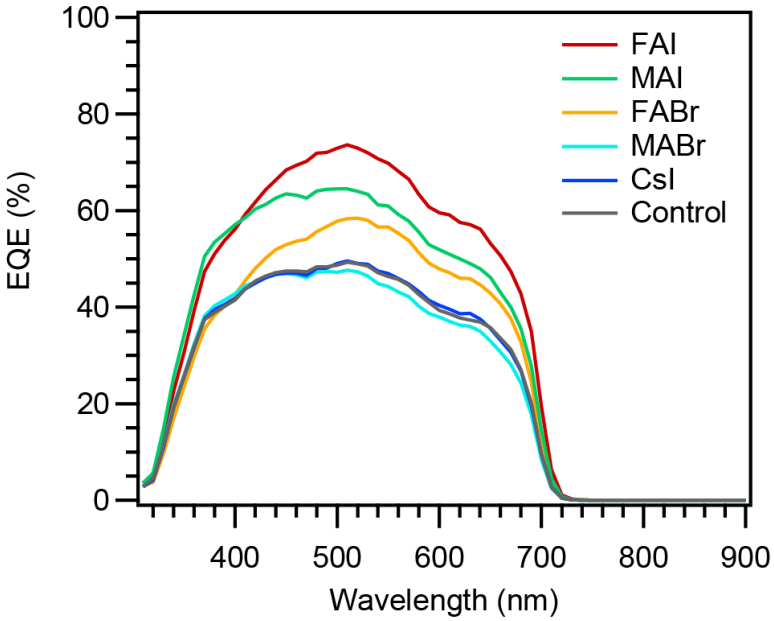

Figure A.15. Comparison of EQE with AX post-treatment. EQE of devices treated with different AX salts observe similar EQE onset at ~700 nm.

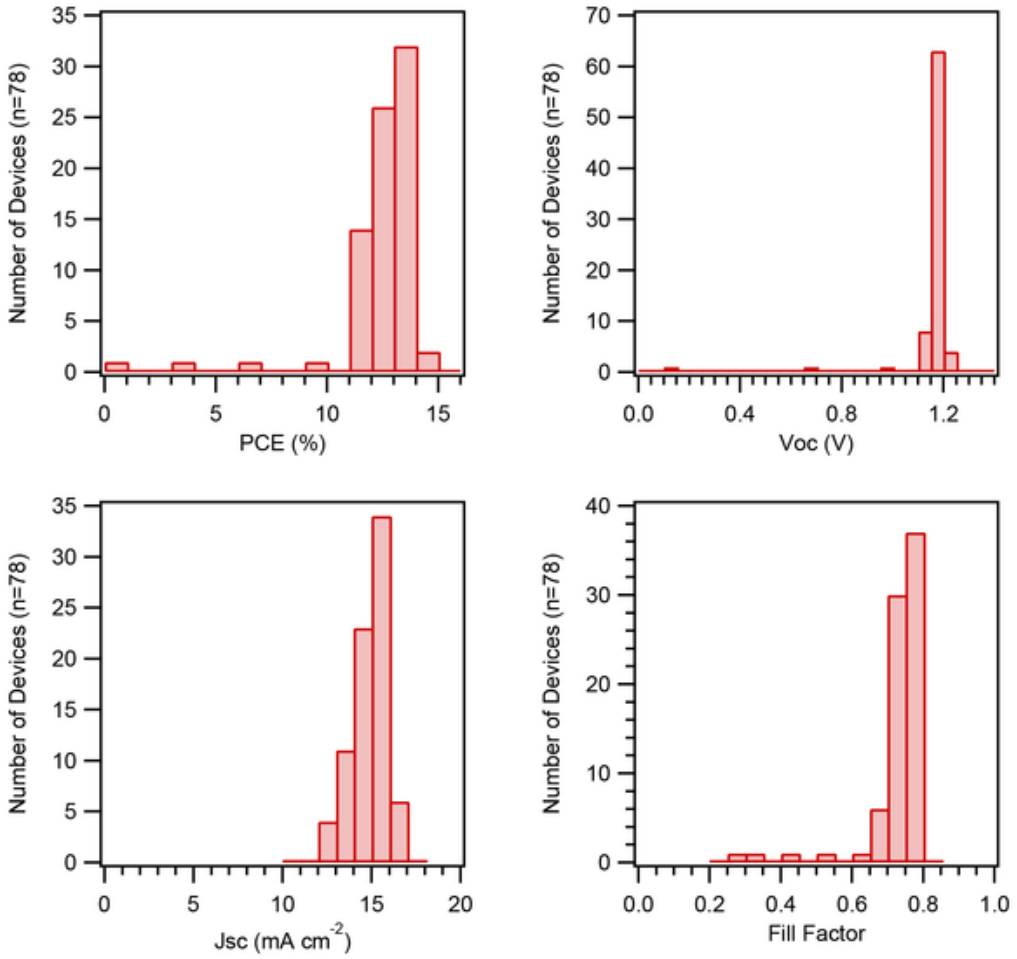

Figure A.16. Reproducibility of FAI-coated CsPbI3 QD device performance. Histograms of the PCE, V_{OC}, J_{SC} and FF of FAI-coated $CsPbI_3$ QD devices (n=78).

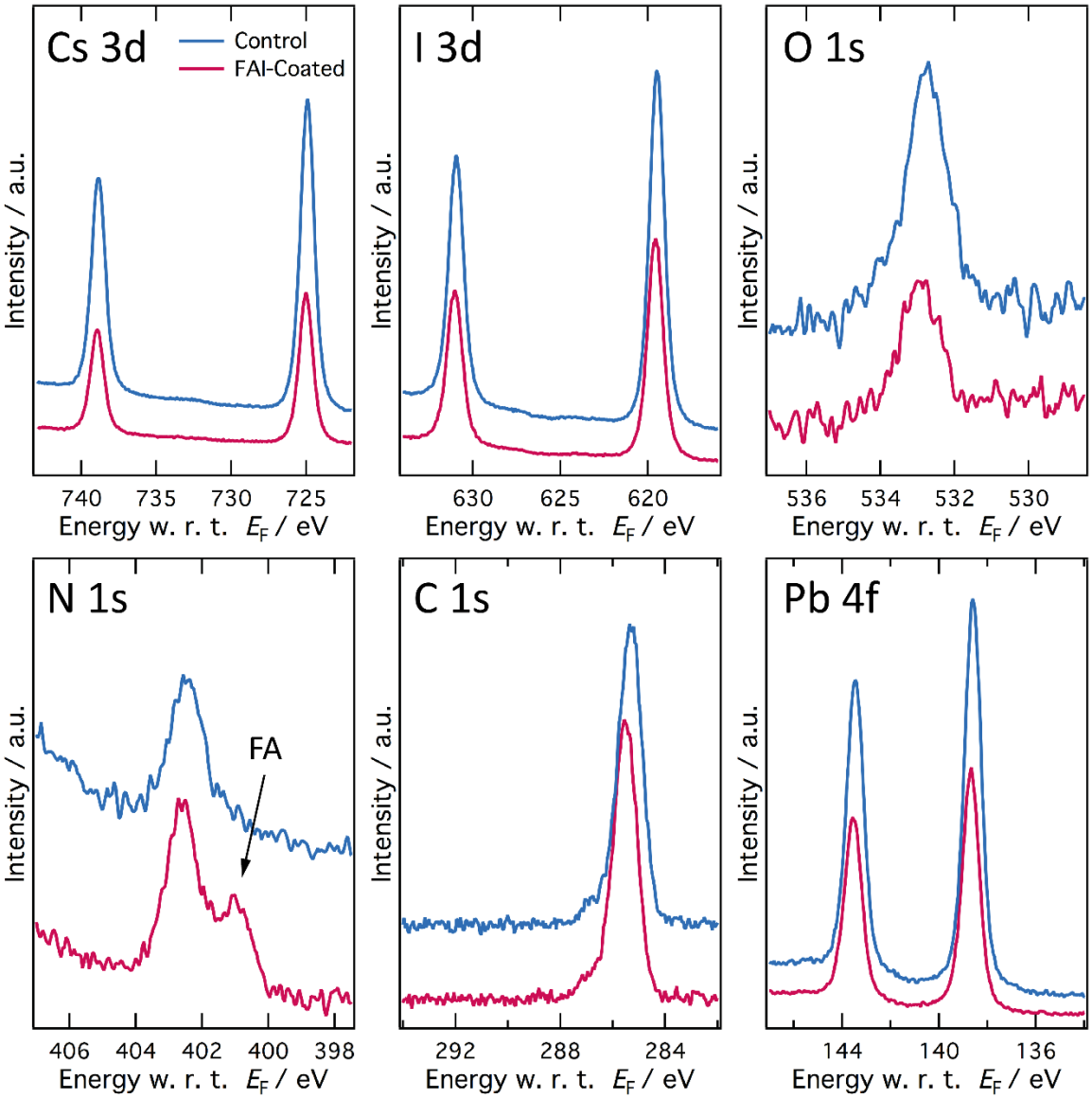

Figure A.17. X-ray photoemission spectroscopy of FAI-coated $CsPbI_3$ QD films. XPS core level spectra of $CsPbI_3$ films on TiO_2/FTO/glass. The presence of FA^+ species is observed by an additional peak centered at 401 eV binding energy in the N 1s core level region. Furthermore, the surface composition changes upon FAI treatment. The Cs^+:Pb^{2+} ratio drops from 0.91 to 0.74 indicating a decrease in Cs^+ content at the surface. At the same time, the I^-:Pb^{2+} ratio rises from 2.73 to 2.83 corroborating the results of the ToF-SIMS measurements. A decrease in the oxygen content upon FAI treatment indicates the further removal of residual oleate groups from the QD surface.

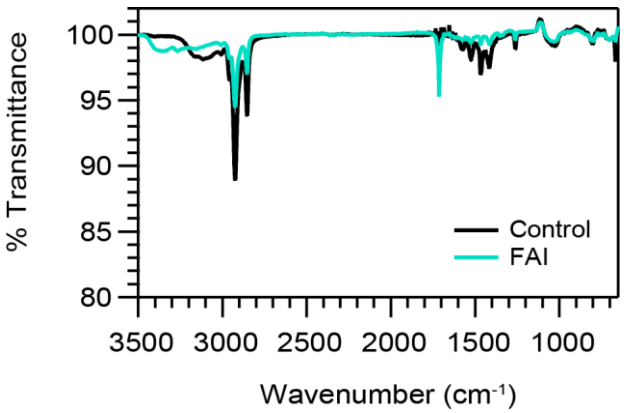

Figure A.18. FTIR spectra of $CsPbI_3$ QDs. Fourier-transformed infrared (FTIR) spectra of $CsPbI_3$ QD films with (green) and without (black) FAI post-treatment. The emergence of the peak at 1712 cm^{-1} is indicative of the presence of FA.

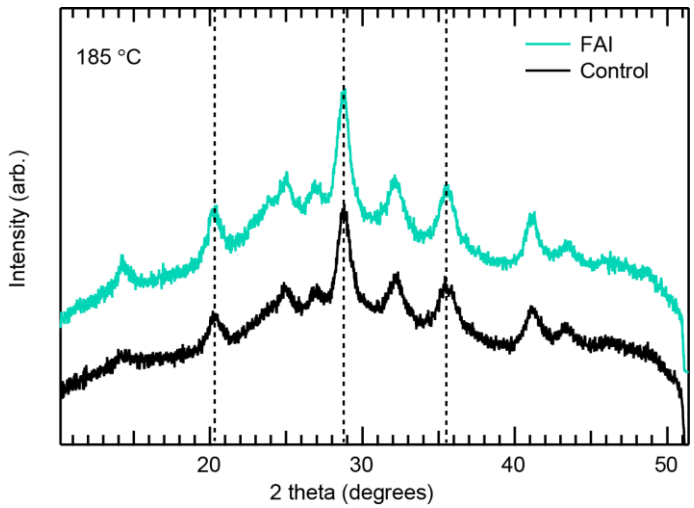

Figure A.19. Crystal structure of $CsPbI_3$ QDs. X-ray diffraction pattern for $CsPbI_3$ QD films with (green) and without (black) FAI post-treatment.

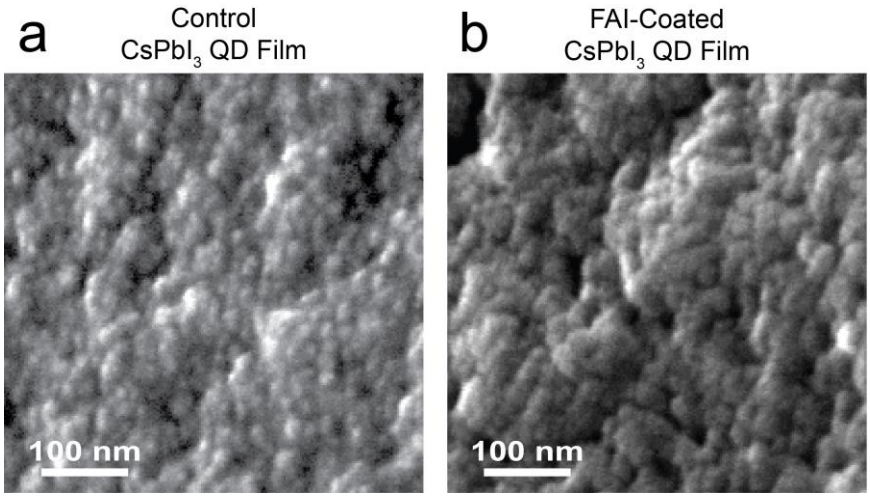

Figure A.20. $CsPbI_3$ QD film morphology. SEM micrographs of the surface of the control and FAI-coated QD films show closely-packed assemblies of discrete nanoparticles in both cases.

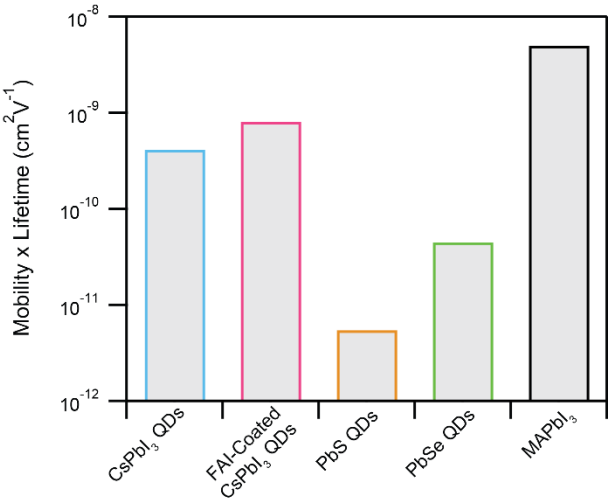

Figure A.21. Comparison of THz $\mu_s \times \tau$ product. Comparison of the $\mu_s \times \tau$ product calculated from THz spectroscopy for the control $CsPbI_3$ QD and FAI-coated $CsPbI_3$ QD films compared to a PbS QD film, a PbSe QD film, and a $MAPbI_3$ thin film.

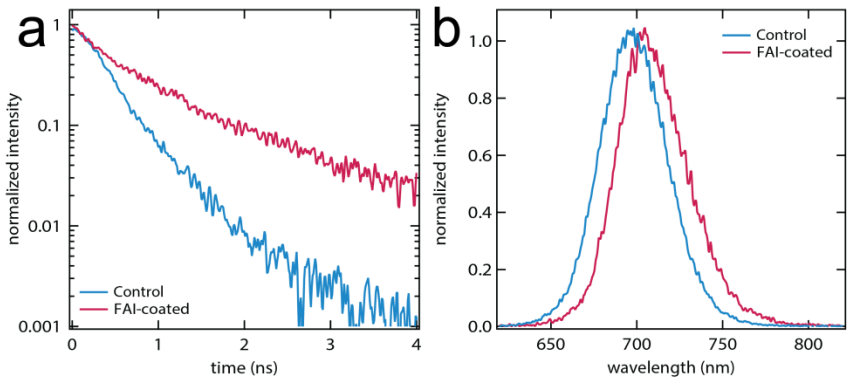

Figure A.22. Photoluminescence lifetime of $CsPbI_3$. Time resolved photoluminescence decay plots for $CsPbI_3$ QD films with (pink) and without (blue) FAI post-treatment.

Appendix B. EDIBLE REPRESENTATIONS OF DEVICE FABRICATION

Figure B.1. Patterned FTO substrates termed “race track pattern” is illustrated on this cake where the FTO and glass areas are represented by the frosting without and with sprinkles, respectively.

Figure B.2. FAI-coated $CsPbI_3$ QD film with the cubic QDs and FAI coating represented by red velvet cake cubes and pink buttercream frosting, respectively.

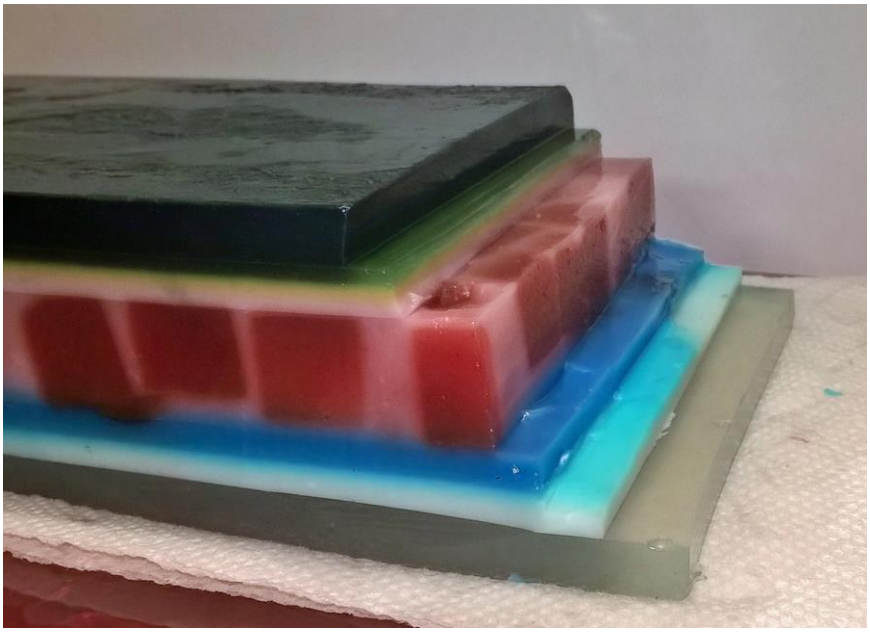

Figure B.3. Cross-section of FAI-coated $CsPbI_3$ QD solar cell depicted with agar agar (i.e. vegan jello) of a full device stack consisting of glass/FTO/TiO_2/FAI-coated $CsPbI_3$ QDs/Spiro-OMeTAD/MoO_x/Al (from the bottom to the top).

REFERENCES

[1] IPCC, "IPCC, 2013: Summary for Policymakers.," in *Climate Change 2013: The Physical Science Basis. Contribution of Working Group I to the Fifth Assessment Report of the Intergovernmental Panel on Climate Change*, 2013.

[2] REN21, "Renewable 2017 Global Status Report," 2017.

[3] J. Nelson, *The physics of solar cells*. World Scientific Publishing Co Inc, 2003.

[4] W. Shockley and H. J. Queisser, "Detailed Balance Limit of Efficiency of p-n Junction Solar Cells," *J. Appl. Phys.*, vol. 32, no. 3, pp. 510–519, Mar. 1961.

[5] S. Rühle, "Tabulated values of the Shockley–Queisser limit for single junction solar cells," *Sol. Energy*, vol. 130, pp. 139–147, Jun. 2016.

[6] A. Polman, M. Knight, E. C. Garnett, B. Ehrler, and W. C. Sinke, "Photovoltaic materials: Present efficiencies and future challenges," *Science*, vol. 352, no. 6283, p. aad4424-aad4424, Apr. 2016.

[7] A. De Vos, "Detailed balance limit of the efficiency of tandem solar cells," *J. Phys. D. Appl. Phys.*, vol. 13, no. 5, p. 839, 1980.

[8] A. Martí and G. L. Araújo, "Limiting efficiencies for photovoltaic energy conversion in multigap systems," *Sol. Energy Mater. Sol. Cells*, vol. 43, no. 2, pp. 203–222, Sep. 1996.

[9] A. J. Nozik, M. C. Beard, J. M. Luther, M. Law, R. J. Ellingson, and J. C. Johnson, "Semiconductor Quantum Dots and Quantum Dot Arrays and Applications of Multiple Exciton Generation to Third-Generation Photovoltaic Solar Cells," *Chem. Rev.*, vol. 110, no. 11, pp. 6873–6890, Nov. 2010.

[10] A. J. Nozik, "Quantum dot solar cells," *Phys. E Low-dimensional Syst. Nanostructures*, vol. 14, no. 1–2, pp. 115–120, Apr. 2002.

[11] K. Branker, M. J. M. Pathak, and J. M. Pearce, "A review of solar photovoltaic levelized cost of electricity," *Renew. Sustain. Energy Rev.*, vol. 15, no. 9, pp. 4470–4482, 2011.

[12] D. Chung, C. Davidson, R. Fu, K. Ardani, and R. Margolis, "US Photovoltaic Prices and Cost Breakdowns: Q1 2015 Benchmarks for Residential, Commercial, and Utility-Scale Systems," NREL (National Renewable Energy Laboratory (NREL), 2015.

[13] A. Kojima, K. Teshima, Y. Shirai, and T. Miyasaka, "Organometal Halide Perovskites as Visible-Light Sensitizers for Photovoltaic Cells," *J. Am. Chem. Soc.*, vol. 131, no. 17, pp. 6050–6051, May 2009.

[14] J.-H. Im, C.-R. Lee, J.-W. Lee, S.-W. Park, and N.-G. Park, "6.5% efficient perovskite quantum-dot-sensitized solar cell," *Nanoscale*, vol. 3, no. 10, pp. 4088–4093, 2011.

[15] H.-S. Kim, C.-R. Lee, J.-H. Im, K.-B. Lee, T. Moehl, A. Marchioro, S.-J. Moon, R. Humphry-Baker, J.-H. Yum, J. E. Moser, M. Gratzel, and N.-G. Park, "Lead Iodide Perovskite Sensitized All-Solid-State Submicron Thin Film Mesoscopic Solar Cell with Efficiency Exceeding 9%," *Sci. Rep.*, vol. 2, Aug. 2012.

[16] M. M. Lee, J. Teuscher, T. Miyasaka, T. N. Murakami, and H. J. Snaith, "Efficient hybrid solar cells based on meso-superstructured organometal halide perovskites.," *Science*, vol. 338, no. 6107, pp. 643–7, Nov. 2012.

[17] "NREL Best Research-Cell Photovoltaic Efficiency Chart," 2017. [Online]. Available: http://www.nrel.gov/ncpv/images/efficiency_chart.jpg. [Accessed: 05-Jul-2017].

[18] J. H. Noh, S. H. Im, J. H. Heo, T. N. Mandal, and S. Il Seok, "Chemical Management for Colorful, Efficient, and Stable Inorganic–Organic Hybrid Nanostructured Solar Cells," *Nano Lett.*, vol. 13, no. 4, pp. 1764–1769, Apr. 2013.

[19] J. Im, C. C. Stoumpos, H. Jin, A. J. Freeman, and M. G. Kanatzidis, "Antagonism between Spin–Orbit Coupling and Steric Effects Causes Anomalous Band Gap Evolution in the Perovskite Photovoltaic Materials CH 3 NH 3 Sn 1– x Pb x I 3," *J. Phys. Chem. Lett.*, vol. 6, no. 17, pp. 3503–3509, Sep. 2015.

[20] Z. Li, M. Yang, J.-S. Park, S.-H. Wei, J. J. Berry, and K. Zhu, "Stabilizing Perovskite Structures by Tuning Tolerance Factor: Formation of Formamidinium and Cesium Lead Iodide Solid-State Alloys," *Chem. Mater.*, vol. 28, no. 1, pp. 284–292, Jan. 2016.

[21] D. P. McMeekin, G. Sadoughi, W. Rehman, G. E. Eperon, M. Saliba, M. T. Horantner, A. Haghighirad, N. Sakai, L. Korte, B. Rech, M. B. Johnston, L. M. Herz, and H. J. Snaith, "A mixed-cation lead mixed-halide perovskite absorber for tandem solar cells," *Science*, vol. 351, no. 6269, pp. 151–155, Jan. 2016.

[22] G. E. Eperon, S. D. Stranks, C. Menelaou, M. B. Johnston, L. M. Herz, and H. J. Snaith, "Formamidinium lead trihalide: a broadly tunable perovskite for efficient planar heterojunction solar cells," *Energy Environ. Sci.*, vol. 7, no. 3, pp. 982–988, 2014.

[23] M. Saliba, T. Matsui, J.-Y. Seo, K. Domanski, J.-P. Correa-Baena, M. K. Nazeeruddin, S. M. Zakeeruddin, W. Tress, A. Abate, A. Hagfeldt, and M. Gratzel, "Cesium-containing triple cation perovskite solar cells: improved stability, reproducibility and high

efficiency," *Energy Environ. Sci.*, vol. 9, no. 6, pp. 1989–1997, 2016.

[24] T. Leijtens, G. E. Eperon, N. K. Noel, S. N. Habisreutinger, A. Petrozza, and H. J. Snaith, "Stability of Metal Halide Perovskite Solar Cells," *Adv. Energy Mater.*, vol. 5, no. 20, p. 1500963, Sep. 2015.

[25] H. S. Jung and N.-G. Park, "Perovskite Solar Cells: From Materials to Devices," *Small*, vol. 11, no. 1, pp. 10–25, Jan. 2015.

[26] S. De Wolf, J. Holovsky, S.-J. Moon, P. Löper, B. Niesen, M. Ledinsky, F.-J. Haug, J.-H. Yum, and C. Ballif, "Organometallic Halide Perovskites: Sharp Optical Absorption Edge and Its Relation to Photovoltaic Performance," *J. Phys. Chem. Lett.*, vol. 5, no. 6, pp. 1035–1039, Mar. 2014.

[27] W.-J. Yin, T. Shi, and Y. Yan, "Unusual defect physics in CH3NH3PbI3 perovskite solar cell absorber," *Appl. Phys. Lett.*, vol. 104, no. 6, p. 63903, Feb. 2014.

[28] H. Zhou, Q. Chen, G. Li, S. Luo, T. -b. Song, H.-S. Duan, Z. Hong, J. You, Y. Liu, and Y. Yang, "Interface engineering of highly efficient perovskite solar cells," *Science*, vol. 345, no. 6196, pp. 542–546, Aug. 2014.

[29] G. Niu, W. Li, F. Meng, L. Wang, H. Dong, and Y. Qiu, "Study on the stability of CH 3 NH 3 PbI 3 films and the effect of post-modification by aluminum oxide in all-solid-state hybrid solar cells," *J. Mater. Chem. A*, vol. 2, no. 3, pp. 705–710, 2014.

[30] J. Yang, B. D. Siempelkamp, D. Liu, and T. L. Kelly, "Investigation of CH3NH3PbI3 Degradation Rates and Mechanisms in Controlled Humidity Environments Using in Situ Techniques," *ACS Nano*, vol. 9, no. 2, pp. 1955–1963, Feb. 2015.

[31] B. Conings, J. Drijkoningen, N. Gauquelin, A. Babayigit, J. D'Haen, L. D'Olieslaeger, A. Ethirajan, J. Verbeeck, J. Manca, E. Mosconi, F. De Angelis, and H.-G. Boyen, "Intrinsic Thermal Instability of Methylammonium Lead Trihalide Perovskite," *Adv. Energy Mater.*, vol. 5, no. 15, p. 1500477, Aug. 2015.

[32] R. K. Misra, S. Aharon, B. Li, D. Mogilyanski, I. Visoly-fisher, D. Mogilyansky, I. Visoly-fisher, L. Etgar, and E. a. Katz, "Temperature- and Component-Dependent Degradation of Perovskite Photovoltaic Materials under Concentrated Sunlight," *J. Phys. Chem. Lett.*, vol. 6, no. 3, pp. 326–330, 2015.

[33] J. H. Kim, S. T. Williams, N. Cho, C.-C. Chueh, and A. K.-Y. Jen, "Enhanced Environmental Stability of Planar Heterojunction Perovskite Solar Cells Based on Blade-

Coating," *Adv. Energy Mater.*, vol. 5, no. 4, p. 1401229, Feb. 2015.

[34] J. A. Christians, P. A. Miranda Herrera, P. V Kamat, P. A. M. Herrera, and P. V Kamat, "Transformation of the Excited State and Photovoltaic Efficiency of CH3NH3PbI3 Perovskite upon Controlled Exposure to Humidified Air," *J. Am. Chem. Soc.*, vol. 137, no. 4, pp. 1530–1538, Feb. 2015.

[35] N. Aristidou, I. Sanchez-Molina, T. Chotchuangchutchaval, M. Brown, L. Martinez, T. Rath, and S. A. Haque, "The Role of Oxygen in the Degradation of Methylammonium Lead Trihalide Perovskite Photoactive Layers," *Angew. Chemie Int. Ed.*, vol. 54, no. 28, pp. 8208–8212, 2015.

[36] D. Wang, M. Wright, N. K. Elumalai, and A. Uddin, "Stability of perovskite solar cells," *Sol. Energy Mater. Sol. Cells*, vol. 147, pp. 255–275, Apr. 2016.

[37] G. Niu, X. Guo, and L. Wang, "Review of recent progress in chemical stability of perovskite solar cells," *J. Mater. Chem. A*, vol. 3, no. 17, pp. 8970–8980, 2015.

[38] Y. Zhao and K. Zhu, "Optical bleaching of perovskite (CH3NH3)PbI3 through room-temperature phase transformation induced by ammonia," *Chem. Commun.*, vol. 50, no. 13, pp. 1605–1607, 2014.

[39] B. R. Vincent, K. N. Robertson, T. S. Cameron, and O. Knop, "Alkylammonium lead halides. Part 1. Isolated PbI64− ions in (CH3NH3)4PbI6•2H2O," *Can. J. Chem.*, vol. 65, no. 5, pp. 1042–1046, May 1987.

[40] Y. Han, S. Meyer, Y. Dkhissi, K. Weber, J. M. Pringle, U. Bach, L. Spiccia, and Y.-B. Cheng, "Degradation observations of encapsulated planar CH3NH3PbI3 perovskite solar cells at high temperatures and humidity," *J. Mater. Chem. A*, vol. 3, no. 15, pp. 8139–8147, 2015.

[41] S. N. Habisreutinger, T. Leijtens, G. E. Eperon, S. D. Stranks, R. J. Nicholas, and H. J. Snaith, "Carbon Nanotube/Polymer Composites as a Highly Stable Hole Collection Layer in Perovskite Solar Cells," *Nano Lett.*, vol. 14, no. 10, pp. 5561–5568, Oct. 2014.

[42] S. Guarnera, A. Abate, W. Zhang, J. M. Foster, G. Richardson, A. Petrozza, and H. J. Snaith, "Improving the Long-term Stability of Perovskite Solar Cells with a Porous Al2O3 Buffer-layer," *J. Phys. Chem. Lett.*, vol. 6, no. 3, pp. 432–437, Feb. 2015.

[43] X. Dong, X. Fang, M. Lv, B. Lin, S. Zhang, J. Ding, and N. Yuan, "Improvement of the humidity stability of organic-inorganic perovskite solar cells using ultrathin Al2O3 layers

prepared by atomic layer deposition," *J. Mater. Chem. A*, vol. 3, no. 10, pp. 5360–5367, 2015.

[44] L. Zheng, Y.-H. Chung, Y. Ma, L. Zhang, L. Xiao, Z. Chen, S. Wang, B. Qu, and Q. Gong, "A hydrophobic hole transporting oligothiophene for planar perovskite solar cells with improved stability," *Chem. Commun.*, vol. 50, no. 76, pp. 11196–11199, 2014.

[45] Y. Kato, L. K. Ono, M. V Lee, S. Wang, S. R. Raga, and Y. Qi, "Silver Iodide Formation in Methyl Ammonium Lead Iodide Perovskite Solar Cells with Silver Top Electrodes," *Adv. Mater. Interfaces*, vol. 2, no. 13, p. 1500195, 2015.

[46] A. Mei, X. Li, L. Liu, Z. Ku, T. Liu, Y. Rong, M. Xu, M. Hu, J. Chen, Y. Yang, M. Gratzel, and H. Han, "A hole-conductor-free, fully printable mesoscopic perovskite solar cell with high stability," *Science*, vol. 345, no. 6194, pp. 295–298, Jul. 2014.

[47] J.-W. Lee, D.-H. Kim, H.-S. Kim, S.-W. Seo, S. M. Cho, and N.-G. Park, "Formamidinium and Cesium Hybridization for Photo- and Moisture-Stable Perovskite Solar Cell," *Adv. Energy Mater.*, vol. 5, no. 20, p. 1501310, Sep. 2015.

[48] X. Li, I. DarM., C. Yi, J. Luo, M. Tschumi, S. M. Zakeeruddin, M. K. Nazeeruddin, H. Han, and M. Grätzel, "Improved performance and stability of perovskite solar cells by crystal crosslinking with alkylphosphonic acid ω-ammonium chlorides," *Nat Chem*, vol. 7, no. 9, pp. 703–711, Sep. 2015.

[49] D. Bryant, N. Aristidou, S. Pont, I. Sanchez-Molina, T. Chotchunangatchaval, S. Wheeler, J. R. Durrant, and S. A. Haque, "Light and oxygen induced degradation limits the operational stability of methylammonium lead triiodide perovskite solar cells," *Energy Environ. Sci.*, vol. 9, no. 5, pp. 1655–1660, 2016.

[50] T. Leijtens, G. E. Eperon, S. Pathak, A. Abate, M. M. Lee, and H. J. Snaith, "Overcoming ultraviolet light instability of sensitized TiO2 with meso-superstructured organometal tri-halide perovskite solar cells," *Nat Commun*, vol. 4, p. 2885, Dec. 2013.

[51] W. Li, W. Zhang, S. Van Reenen, R. J. Sutton, J. Fan, A. Haghighirad, M. Johnston, L. Wang, and H. Snaith, "Enhanced UV-light Stability of Planar Heterojunction Perovskite Solar Cells with Caesium Bromide Interface Modification," *Energy Environ. Sci.*, vol. 9, pp. 490–498, 2016.

[52] U. B. Cappel, T. Daeneke, and U. Bach, "Oxygen-Induced Doping of Spiro-MeOTAD in Solid-State Dye-Sensitized Solar Cells and Its Impact on Device Performance," *Nano*

Lett., vol. 12, no. 9, pp. 4925–4931, 2012.

[53] L. K. Ono, S. R. Raga, M. Remeika, A. J. Winchester, A. Gabe, and Y. Qi, "Pinhole-free hole transport layers significantly improve the stability of MAPbI 3 -based perovskite solar cells under operating conditions," *J. Mater. Chem. A*, vol. 3, no. 30, pp. 15451–15456, 2015.

[54] V. M. Goldschmidt, "Die Gesetze der Krystallochemie," *Naturwissenschaften*, vol. 14, no. 21, pp. 477–485, 1926.

[55] S. Sharma, N. Weiden, and A. Weiss, "Phase Diagrams of Quasibinary Systems of the Type: ABX_3—$A'BX_3$; ABX_3—$AB'X_3$, and ABX_3—ABX'_3; X = Halogen," *Zeitschrift für Phys. Chemie*, vol. 175, no. 1, pp. 63–80, Jan. 1992.

[56] Q. Ma, S. Huang, X. Wen, M. A. Green, and A. W. Y. Ho-Baillie, "Hole Transport Layer Free Inorganic CsPbIBr 2 Perovskite Solar Cell by Dual Source Thermal Evaporation," *Adv. Energy Mater.*, vol. 6, no. 7, Apr. 2016.

[57] R. E. Beal, D. J. Slotcavage, T. Leijtens, A. R. Bowring, R. A. Belisle, W. H. Nguyen, G. F. Burkhard, E. T. Hoke, and M. D. McGehee, "Cesium Lead Halide Perovskites with Improved Stability for Tandem Solar Cells," *J. Phys. Chem. Lett.*, vol. 7, no. 5, pp. 746–751, Feb. 2016.

[58] R. J. Sutton, G. E. Eperon, L. Miranda, E. S. Parrott, B. A. Kamino, J. B. Patel, M. T. Hörantner, M. B. Johnston, A. A. Haghighirad, D. T. Moore, and H. J. Snaith, "Bandgap-Tunable Cesium Lead Halide Perovskites with High Thermal Stability for Efficient Solar Cells," *Adv. Energy Mater.*, vol. 6, no. 8, p. n/a-n/a, Jan. 2016.

[59] G. E. Eperon, G. M. Paternò, R. J. Sutton, A. Zampetti, A. A. Haghighirad, F. Cacialli, and H. J. Snaith, "Inorganic caesium lead iodide perovskite solar cells," *J. Mater. Chem. A*, vol. 3, no. 39, pp. 19688–19695, Sep. 2015.

[60] L. Protesescu, S. Yakunin, M. I. Bodnarchuk, F. Krieg, R. Caputo, C. H. Hendon, R. X. Yang, A. Walsh, and M. V Kovalenko, "Nanocrystals of Cesium Lead Halide Perovskites ($CsPbX_3$, X = Cl, Br, and I): Novel Optoelectronic Materials Showing Bright Emission with Wide Color Gamut.," *Nano Lett.*, vol. 15, no. 6, pp. 3692–6, Jun. 2015.

[61] V. I. Klimov, *Nanocrystal quantum dots*. CRC Press, 2010.

[62] L. Brus, "Electronic wave functions in semiconductor clusters: experiment and theory," *J. Phys. Chem.*, vol. 90, no. 12, pp. 2555–2560, Jun. 1986.

[63] O. E. Semonin, J. M. Luther, S. Choi, H.-Y. Chen, J. Gao, A. J. Nozik, and M. C. Beard, "Peak External Photocurrent Quantum Efficiency Exceeding 100% via MEG in a Quantum Dot Solar Cell," *Science*, vol. 334, no. 6062, pp. 1530–1533, Dec. 2011.

[64] Y. Yan, R. W. Crisp, J. Gu, B. D. Chernomordik, G. F. Pach, A. R. Marshall, J. A. Turner, and M. C. Beard, "Multiple exciton generation for photoelectrochemical hydrogen evolution reactions with quantum yields exceeding 100%," *Nat. Energy*, vol. 2, no. April, p. 17052, 2017.

[65] P. R. Brown, D. Kim, R. R. Lunt, N. Zhao, M. G. Bawendi, J. C. Grossman, and V. Bulović, "Energy Level Modification in Lead Sulfide Quantum Dot Thin Films through Ligand Exchange," *ACS Nano*, vol. 8, no. 6, pp. 5863–5872, Jun. 2014.

[66] D. M. Kroupa, M. Vörös, N. P. Brawand, B. W. McNichols, E. M. Miller, J. Gu, A. J. Nozik, A. Sellinger, G. Galli, and M. C. Beard, "Tuning colloidal quantum dot band edge positions through solution-phase surface chemistry modification," vol. 8, p. 15257, May 2017.

[67] C.-H. M. Chuang, P. R. Brown, V. Bulović, and M. G. Bawendi, "Improved performance and stability in quantum dot solar cells through band alignment engineering.," *Nat. Mater.*, vol. 13, no. 8, pp. 796–801, Aug. 2014.

[68] R. W. Crisp, D. M. Kroupa, A. R. Marshall, E. M. Miller, J. Zhang, M. C. Beard, and J. M. Luther, "Metal halide solid-state surface treatment for high efficiency PbS and PbSe QD solar cells.," *Sci. Rep.*, vol. 5, p. 9945, Jan. 2015.

[69] B. A. Koscher, J. K. Swabeck, N. D. Bronstein, and A. P. Alivisatos, "Essentially Trap-Free $CsPbBr_3$ Colloidal Nanocrystals by Postsynthetic Thiocyanate Surface Treatment," *J. Am. Chem. Soc.*, p. jacs.7b02817, May 2017.

[70] J. Zhang, J. Gao, E. M. Miller, J. M. Luther, and M. C. Beard, "Diffusion-controlled synthesis of PbS and PbSe quantum dots with in situ halide passivation for quantum dot solar cells," *ACS Nano*, vol. 8, no. 1, pp. 614–622, Jan. 2014.

[71] A. R. Marshall, M. R. Young, A. J. Nozik, M. C. Beard, and J. M. Luther, "Exploration of Metal Chloride Uptake for Improved Performance Characteristics of PbSe Quantum Dot Solar Cells," *J. Phys. Chem. Lett.*, vol. 6, no. 15, pp. 2892–2899, Aug. 2015.

[72] J. van Embden, A. S. R. Chesman, and J. J. Jasieniak, "The Heat-Up Synthesis of Colloidal Nanocrystals," *Chem. Mater.*, vol. 27, no. 7, pp. 2246–2285, Apr. 2015.

[73] X. Li, Y. Wu, S. Zhang, B. Cai, Y. Gu, J. Song, and H. Zeng, “CsPbX 3 Quantum Dots for Lighting and Displays: Room-Temperature Synthesis, Photoluminescence Superiorities, Underlying Origins and White Light-Emitting Diodes,” *Adv. Funct. Mater.*, vol. 26, no. 15, pp. 2435–2445, Apr. 2016.

[74] J. Tang, K. W. Kemp, S. Hoogland, K. S. Jeong, H. Liu, L. Levina, M. Furukawa, X. Wang, R. Debnath, D. Cha, K. W. Chou, A. Fischer, A. Amassian, J. B. Asbury, and E. H. Sargent, “Colloidal-quantum-dot photovoltaics using atomic-ligand passivation,” *Nat. Mater.*, vol. 10, no. 10, pp. 765–771, Sep. 2011.

[75] A. H. Ip, S. M. Thon, S. Hoogland, O. Voznyy, D. Zhitomirsky, R. Debnath, L. Levina, L. R. Rollny, G. H. Carey, A. Fischer, K. W. Kemp, I. J. Kramer, Z. Ning, A. J. Labelle, K. W. Chou, A. Amassian, and E. H. Sargent, “Hybrid passivated colloidal quantum dot solids,” *Nat. Nanotechnol.*, vol. 7, no. 9, pp. 577–582, Jul. 2012.

[76] X. Lan, O. Voznyy, A. Kiani, F. P. García de Arquer, A. S. Abbas, G.-H. Kim, M. Liu, Z. Yang, G. Walters, J. Xu, M. Yuan, Z. Ning, F. Fan, P. Kanjanaboos, I. Kramer, D. Zhitomirsky, P. Lee, A. Perelgut, S. Hoogland, and E. H. Sargent, “Passivation Using Molecular Halides Increases Quantum Dot Solar Cell Performance,” *Adv. Mater.*, vol. 28, no. 2, pp. 299–304, Jan. 2016.

[77] B. D. Chernomordik, A. R. Marshall, G. F. Pach, J. M. Luther, and M. C. Beard, “Quantum Dot Solar Cell Fabrication Protocols,” *Chem. Mater.*, vol. 29, no. 1, pp. 189–198, Jan. 2017.

[78] M. A. Green, Y. Hishikawa, W. Warta, E. D. Dunlop, D. H. Levi, J. Hohl-Ebinger, and A. W. H. Ho-Baillie, “Solar cell efficiency tables (version 50),” *Prog. Photovoltaics Res. Appl.*, vol. 25, no. 7, pp. 668–676, Jul. 2017.

[79] C. S. Ponseca, T. J. Savenije, M. Abdellah, K. Zheng, A. Yartsev, T. Pascher, T. Harlang, P. Chabera, T. Pullerits, A. Stepanov, J.-P. Wolf, and V. Sundström, “Organometal Halide Perovskite Solar Cell Materials Rationalized: Ultrafast Charge Generation, High and Microsecond-Long Balanced Mobilities, and Slow Recombination,” *J. Am. Chem. Soc.*, vol. 136, no. 14, pp. 5189–5192, Apr. 2014.

[80] J. Kim, S.-H. Lee, J. H. Lee, and K.-H. Hong, “The Role of Intrinsic Defects in Methylammonium Lead Iodide Perovskite,” *J. Phys. Chem. Lett.*, vol. 5, no. 8, pp. 1312–1317, Apr. 2014.

[81] J. Burschka, N. Pellet, S.-J. Moon, R. Humphry-Baker, P. Gao, M. K. Nazeeruddin, M. Grätzel, and M. Gratzel, "Sequential deposition as a route to high-performance perovskite-sensitized solar cells," *Nature*, vol. 499, no. 7458, pp. 316–319, Jul. 2013.

[82] W. Zhang, M. Saliba, D. T. Moore, S. K. Pathak, M. T. Hörantner, T. Stergiopoulos, S. D. Stranks, G. E. Eperon, J. A. Alexander-Webber, A. Abate, A. Sadhanala, S. Yao, Y. Chen, R. H. Friend, L. A. Estroff, U. Wiesner, and H. J. Snaith, "Ultrasmooth organic–inorganic perovskite thin-film formation and crystallization for efficient planar heterojunction solar cells," *Nat. Commun.*, vol. 6, p. 6142, Jan. 2015.

[83] N. Ahn, D.-Y. Son, I.-H. Jang, S. M. Kang, M. Choi, and N.-G. Park, "Highly Reproducible Perovskite Solar Cells with Average Efficiency of 18.3% and Best Efficiency of 19.7% Fabricated via Lewis Base Adduct of Lead(II) Iodide," *J. Am. Chem. Soc.*, vol. 137, no. 27, pp. 8696–8699, Jul. 2015.

[84] W. S. Yang, J. H. Noh, N. J. Jeon, Y. C. Kim, S. Ryu, J. Seo, and S. Il Seok, "High-performance photovoltaic perovskite layers fabricated through intramolecular exchange," *Science*, vol. 348, no. 6240, pp. 1234–1237, Jun. 2015.

[85] A. Abate, M. Saliba, D. J. Hollman, S. D. Stranks, K. Wojciechowski, R. Avolio, G. Grancini, A. Petrozza, and H. J. Snaith, "Supramolecular halogen bond passivation of organic-inorganic halide perovskite solar cells.," *Nano Lett.*, vol. 14, no. 6, pp. 3247–54, Jun. 2014.

[86] Y. Shao, Z. Xiao, C. Bi, Y. Yuan, and J. Huang, "Origin and elimination of photocurrent hysteresis by fullerene passivation in CH3NH3PbI3 planar heterojunction solar cells," *Nat. Commun.*, vol. 5, p. 5784, Dec. 2014.

[87] N. K. Noel, A. Abate, S. D. Stranks, E. S. Parrott, V. M. Burlakov, A. Goriely, and H. J. Snaith, "Enhanced Photoluminescence and Solar Cell Performance via Lewis Base Passivation of Organic–Inorganic Lead Halide Perovskites," *ACS Nano*, vol. 8, no. 10, pp. 9815–9821, Oct. 2014.

[88] Y. Rong, L. Liu, A. Mei, X. Li, and H. Han, "Beyond Efficiency: the Challenge of Stability in Mesoscopic Perovskite Solar Cells," *Adv. Energy Mater.*, vol. 5, no. 20, p. 1501066, Oct. 2015.

[89] B. Hailegnaw, S. Kirmayer, E. Edri, G. Hodes, and D. Cahen, "Rain on Methylammonium Lead Iodide Based Perovskites: Possible Environmental Effects of Perovskite Solar

Cells," *J. Phys. Chem. Lett.*, vol. 6, no. 9, pp. 1543–1547, May 2015.

[90] H. L. Clever and F. J. Johnston, "The solubility of some sparingly soluble lead salts: An evaluation of the solubility in water and aqueous electrolyte solution," *J. Phys. Chem. Ref. Data*, vol. 9, no. 3, p. 751, 1980.

[91] M. D. Kempe, A. A. Dameron, and M. O. Reese, "Evaluation of moisture ingress from the perimeter of photovoltaic modules," *Prog. Photovoltaics Res. Appl.*, vol. 22, no. 11, pp. 1159–1171, 2014.

[92] X. Li, M. Tschumi, H. Han, S. S. Babkair, R. A. Alzubaydi, A. A. Ansari, S. S. Habib, M. K. Nazeeruddin, S. M. Zakeeruddin, and M. Grätzel, "Outdoor Performance and Stability under Elevated Temperatures and Long-Term Light Soaking of Triple-Layer Mesoporous Perovskite Photovoltaics," *Energy Technol.*, vol. 3, no. 6, pp. 551–555, 2015.

[93] Y. Zhao, A. M. Nardes, and K. Zhu, "Effective hole extraction using MoOx-Al contact in perovskite CH3NH3PbI3 solar cells," *Appl. Phys. Lett.*, vol. 104, no. 21, p. 213906, May 2014.

[94] J. Meyer, S. Hamwi, M. Kröger, W. Kowalsky, T. Riedl, and A. Kahn, "Transition metal oxides for organic electronics: energetics, device physics and applications.," *Adv. Mater.*, vol. 24, no. 40, pp. 5408–27, Oct. 2012.

[95] T. Matsushima, Y. Kinoshita, and H. Murata, "Formation of Ohmic hole injection by inserting an ultrathin layer of molybdenum trioxide between indium tin oxide and organic hole-transporting layers," *Appl. Phys. Lett.*, vol. 91, no. 25, p. 253504, 2007.

[96] H. You, Y. Dai, Z. Zhang, and D. Ma, "Improved performances of organic light-emitting diodes with metal oxide as anode buffer," *J. Appl. Phys.*, vol. 101, no. 2, p. 26105, 2007.

[97] V. Shrotriya, G. Li, Y. Yao, C.-W. Chu, and Y. Yang, "Transition metal oxides as the buffer layer for polymer photovoltaic cells," *Appl. Phys. Lett.*, vol. 88, no. 7, p. 73508, 2006.

[98] B. Dasgupta, W. P. Goh, Z. E. Ooi, L. M. Wong, C. Y. Jiang, Y. Ren, E. S. Tok, J. Pan, J. Zhang, and S. Y. Chiam, "Enhanced Extraction Rates through Gap States of Molybdenum Oxide Anode Buffer," *J. Phys. Chem. C*, vol. 117, no. 18, pp. 9206–9211, May 2013.

[99] H. Pan, L. Zuo, W. Fu, C. Fan, B. Andreasen, X. Jiang, K. Norrman, F. C. Krebs, and H. Chen, "MoO3–Au composite interfacial layer for high efficiency and air-stable organic solar cells," *Org. Electron.*, vol. 14, no. 3, pp. 797–803, Mar. 2013.

[100] J. Gao, C. L. Perkins, J. M. Luther, M. C. Hanna, H.-Y. Chen, O. E. Semonin, A. J. Nozik, R. J. Ellingson, and M. C. Beard, "n-Type Transition Metal Oxide as a Hole Extraction Layer in PbS Quantum Dot Solar Cells," *Nano Lett.*, vol. 11, no. 8, pp. 3263–3266, Aug. 2011.

[101] P. R. Brown, R. R. Lunt, N. Zhao, T. P. Osedach, D. D. Wanger, L.-Y. Chang, M. G. Bawendi, and V. Bulović, "Improved Current Extraction from ZnO/PbS Quantum Dot Heterojunction Photovoltaics Using a MoO3 Interfacial Layer," *Nano Lett.*, vol. 11, no. 7, pp. 2955–2961, Jul. 2011.

[102] O. Malinkiewicz, C. Roldán-Carmona, A. Soriano, E. Bandiello, L. Camacho, M. K. Nazeeruddin, and H. J. Bolink, "Metal-Oxide-Free Methylammonium Lead Iodide Perovskite-Based Solar Cells: the Influence of Organic Charge Transport Layers," *Adv. Energy Mater.*, vol. 4, no. 15, p. n/a-n/a, 2014.

[103] N. J. Jeon, J. H. Noh, Y. C. Kim, W. S. Yang, S. Ryu, and S. Il Seok, "Solvent engineering for high-performance inorganic-organic hybrid perovskite solar cells.," *Nat. Mater.*, vol. 13, no. July, pp. 1–7, Sep. 2014.

[104] N. R. Neale and A. J. Frank, "Size and shape control of nanocrystallites in mesoporous TiO2 films," *J. Mater. Chem.*, vol. 17, no. 30, pp. 3216–3221, 2007.

[105] H. J. Snaith, A. Abate, J. M. Ball, G. E. Eperon, T. Leijtens, N. K. Noel, S. D. Stranks, J. T.-W. Wang, K. Wojciechowski, and W. Zhang, "Anomalous hysteresis in perovskite solar cells," *J. Phys. Chem. Lett.*, vol. 5, no. 9, pp. 1511–1515, 2014.

[106] M. O. Reese, S. A. Gevorgyan, M. Jørgensen, E. Bundgaard, S. R. Kurtz, D. S. Ginley, D. C. Olson, M. T. Lloyd, P. Morvillo, E. A. Katz, A. Elschner, O. Haillant, T. R. Currier, V. Shrotriya, M. Hermenau, M. Riede, K. R. Kirov, G. Trimmel, T. Rath, O. Inganäs, F. Zhang, M. Andersson, K. Tvingstedt, M. Lira-Cantu, D. Laird, C. McGuiness, S. (Jimmy) Gowrisanker, M. Pannone, M. Xiao, J. Hauch, R. Steim, D. M. DeLongchamp, R. Rösch, H. Hoppe, N. Espinosa, A. Urbina, G. Yaman-Uzunoglu, J.-B. Bonekamp, A. J. J. M. van Breemen, C. Girotto, E. Voroshazi, and F. C. Krebs, "Consensus stability testing protocols for organic photovoltaic materials and devices," *Sol. Energy Mater. Sol. Cells*, vol. 95, no. 5, pp. 1253–1267, May 2011.

[107] M. Vasilopoulou, A. M. Douvas, D. G. Georgiadou, L. C. Palilis, S. Kennou, L. Sygellou, A. Soultati, I. Kostis, G. Papadimitropoulos, D. Davazoglou, and P. Argitis, "The

Influence of Hydrogenation and Oxygen Vacancies on Molybdenum Oxides Work Function and Gap States for Application in Organic Optoelectronics," *J. Am. Chem. Soc.*, vol. 134, no. 39, pp. 16178–16187, Oct. 2012.

[108] V. Bhosle, A. Tiwari, and J. Narayan, "Epitaxial growth and properties of MoO[sub x](2<x<2.75) films," *J. Appl. Phys.*, vol. 97, no. 8, p. 83539, 2005.

[109] J. J. Jasieniak, J. Seifter, J. Jo, T. Mates, and A. J. Heeger, "A Solution-Processed MoOx Anode Interlayer for Use within Organic Photovoltaic Devices," *Adv. Funct. Mater.*, vol. 22, no. 12, pp. 2594–2605, Jun. 2012.

[110] M. Chase, "NIST-JANAF Thermochemical Tables, 4th Edition," *J. Phys. Chem. Ref. Data, Monogr. 9*, p. 1952, 1998.

[111] D. P. Nenon, J. A. Christians, L. M. Wheeler, J. L. Blackburn, E. M. Sanehira, B. Dou, M. L. Olsen, K. Zhu, J. J. Berry, and J. M. Luther, "Structural and chemical evolution of methylammonium lead halide perovskites during thermal processing from solution," *Energy Environ. Sci.*, vol. 9, no. 6, pp. 2072–2082, 2016.

[112] S. Sharma, N. Weiden, and A. Weiss, "Phase Diagrams of Quasibinary Systems of the Type: ABX 3 — A'BX 3 ; ABX 3 — AB'X 3 , and ABX 3 — ABX' 3 ; X = Halogen," *Zeitschrift für Phys. Chemier Phys. Chemie*, vol. 175, no. Part_1, pp. 63–80, Jan. 1992.

[113] A. P. Alivisatos, "Semiconductor Clusters, Nanocrystals, and Quantum Dots," *Science*, vol. 271, no. 5251, pp. 933–937, Feb. 1996.

[114] S. H. Tolbert and A. P. Alivisatos, "Size Dependence of a First Order Solid-Solid Phase Transition: The Wurtzite to Rock Salt Transformation in CdSe Nanocrystals," *Science*, vol. 265, no. 5170, pp. 373–376, Jul. 1994.

[115] F. Wang, Y. Han, C. S. Lim, Y. Lu, J. Wang, J. Xu, H. Chen, C. Zhang, M. Hong, and X. Liu, "Simultaneous phase and size control of upconversion nanocrystals through lanthanide doping," *Nature*, vol. 463, no. 7284, pp. 1061–1065, Feb. 2010.

[116] C. C. Yang and S. Li, "Size-Dependent Phase Stability of Silver Nanocrystals," *J. Phys. Chem. C*, vol. 112, no. 42, pp. 16400–16404, Oct. 2008.

[117] S. Schlag, H.-F. Eicke, and W. B. Stern, "Size driven phase transition and thermodynamic properties of nanocrystalline batio3," *Ferroelectrics*, vol. 173, no. 1, pp. 351–369, Jan. 1995.

[118] L. C. Schmidt, A. Pertegás, S. González-Carrero, O. Malinkiewicz, S. Agouram, G.

Mínguez Espallargas, H. J. Bolink, R. E. Galian, and J. Pérez-Prieto, "Nontemplate synthesis of CH3NH3PbBr3 perovskite nanoparticles.," *J. Am. Chem. Soc.*, vol. 136, no. 3, pp. 850–3, Jan. 2014.

[119] F. Zhang, H. Zhong, C. Chen, X. Wu, X. Hu, H. Huang, J. Han, B. Zou, and Y. Dong, "Brightly Luminescent and Color-Tunable Colloidal CH 3 NH 3 PbX 3 (X = Br, I, Cl) Quantum Dots: Potential Alternatives for Display Technology," *ACS Nano*, vol. 9, no. 4, pp. 4533–4542, Apr. 2015.

[120] D. Zhang, S. W. Eaton, Y. Yu, L. Dou, and P. Yang, "Solution-Phase Synthesis of Cesium Lead Halide Perovskite Nanowires.," *J. Am. Chem. Soc.*, vol. 137, no. 29, pp. 9230–3, Jul. 2015.

[121] H. Huang, F. Zhao, L. Liu, F. Zhang, X. G. Wu, L. Shi, B. Zou, Q. Pei, and H. Zhong, "Emulsion Synthesis of Size-Tunable CH3NH3PbBr3 Quantum Dots: An Alternative Route toward Efficient Light-Emitting Diodes," *ACS Appl. Mater. Interfaces*, vol. 7, no. 51, pp. 28128–28133, Dec. 2015.

[122] Y. Hassan, Y. Song, R. D. Pensack, A. I. Abdelrahman, Y. Kobayashi, M. A. Winnik, and G. D. Scholes, "Structure-Tuned Lead Halide Perovskite Nanocrystals," *Adv. Mater.*, vol. 28, no. 3, pp. 566–573, Jan. 2016.

[123] S. Sun, D. Yuan, Y. Xu, A. Wang, and Z. Deng, "Ligand-Mediated Synthesis of Shape-Controlled Cesium Lead Halide Perovskite Nanocrystals via Reprecipitation Process at Room Temperature," *ACS Nano*, vol. 10, no. 3, pp. 3648–3657, Mar. 2016.

[124] T. C. Jellicoe, J. M. Richter, H. F. J. Glass, M. Tabachnyk, R. Brady, S. E. Dutton, A. Rao, R. H. Friend, D. Credgington, N. C. Greenham, and M. L. Böhm, "Synthesis and Optical Properties of Lead-Free Cesium Tin Halide Perovskite Nanocrystals," *J. Am. Chem. Soc.*, vol. 138, no. 9, pp. 2941–2944, Mar. 2016.

[125] Y. Wang, X. Li, J. Song, L. Xiao, H. Zeng, and H. Sun, "All-Inorganic Colloidal Perovskite Quantum Dots: A New Class of Lasing Materials with Favorable Characteristics," *Adv. Mater.*, vol. 27, no. 44, pp. 7101–7108, Nov. 2015.

[126] S. Yakunin, L. Protesescu, F. Krieg, M. I. Bodnarchuk, G. Nedelcu, M. Humer, G. De Luca, M. Fiebig, W. Heiss, and M. V. Kovalenko, "Low-threshold amplified spontaneous emission and lasing from colloidal nanocrystals of caesium lead halide perovskites," *Nat. Commun.*, vol. 6, p. 8056, Aug. 2015.

[127] Y. Xu, Q. Chen, C. Zhang, R. Wang, H. Wu, X. Zhang, G. Xing, W. W. Yu, X. Wang, Y. Zhang, and M. Xiao, “Two-Photon-Pumped Perovskite Semiconductor Nanocrystal Lasers,” *J. Am. Chem. Soc.*, vol. 138, no. 11, pp. 3761–3768, Mar. 2016.

[128] A. Swarnkar, R. Chulliyil, V. K. Ravi, M. Irfanullah, A. Chowdhury, and A. Nag, “Colloidal CsPbBr3 Perovskite Nanocrystals: Luminescence beyond Traditional Quantum Dots,” *Angew. Chemie*, vol. 127, no. 51, pp. 15644–15648, Dec. 2015.

[129] F. Hu, H. Zhang, C. Sun, C. Yin, B. Lv, C. Zhang, W. W. Yu, X. Wang, Y. Zhang, and M. Xiao, “Superior Optical Properties of Perovskite Nanocrystals as Single Photon Emitters,” *ACS Nano*, vol. 9, no. 12, pp. 12410–12416, Dec. 2015.

[130] Q. A. Akkerman, S. G. Motti, A. R. Srimath Kandada, E. Mosconi, V. D’Innocenzo, G. Bertoni, S. Marras, B. A. Kamino, L. Miranda, F. De Angelis, A. Petrozza, M. Prato, and L. Manna, “Solution Synthesis Approach to Colloidal Cesium Lead Halide Perovskite Nanoplatelets with Monolayer-Level Thickness Control,” *J. Am. Chem. Soc.*, vol. 138, no. 3, pp. 1010–1016, Jan. 2016.

[131] N. S. Makarov, S. Guo, O. Isaienko, W. Liu, I. Robel, and V. I. Klimov, “Spectral and dynamical properties of single excitons, biexcitons, and trions in cesium-lead-halide perovskite quantum dots,” *Nano Lett.*, p. acs.nanolett.5b05077, Feb. 2016.

[132] Y. Bekenstein, B. A. Koscher, S. W. Eaton, P. Yang, and A. P. Alivisatos, “Highly Luminescent Colloidal Nanoplates of Perovskite Cesium Lead Halide and Their Oriented Assemblies,” *J. Am. Chem. Soc.*, vol. 137, no. 51, pp. 16008–16011, Dec. 2015.

[133] J. De Roo, M. Ibáñez, P. Geiregat, G. Nedelcu, W. Walravens, J. Maes, J. C. Martins, I. Van Driessche, M. V Kovalenko, and Z. Hens, “Highly Dynamic Ligand Binding and Light Absorption Coefficient of Cesium Lead Bromide Perovskite Nanocrystals,” *ACS Nano*, vol. 10, no. 2, pp. 2071–2081, Feb. 2016.

[134] Y.-S. Park, S. Guo, N. S. Makarov, and V. I. Klimov, “Room Temperature Single-Photon Emission from Individual Perovskite Quantum Dots,” *ACS Nano*, vol. 9, no. 10, pp. 10386–10393, Oct. 2015.

[135] L. Lutterotti, “MAUD, version 2.55 released April 30, 2015.” .

[136] L. Lutterotti, P. Scardi, and P. Maistrelli, “LS1 - a computer program for simultaneous refinement of material structure and microstructure,” *J. Appl. Crystallogr.*, vol. 25, no. pt 3, pp. 459–462, Jun. 1992.

[137] D. M. Trots and S. V. Myagkota, “High-temperature structural evolution of caesium and rubidium triiodoplumbates,” *J. Phys. Chem. Solids*, vol. 69, no. 10, pp. 2520–2526, Oct. 2008.

[138] R. G. Pearson, “Hard and Soft Acids and Bases,” *J. Am. Chem. Soc.*, vol. 85, no. 22, pp. 3533–3539, Nov. 1963.

[139] Q. A. Akkerman, V. D’Innocenzo, S. Accornero, A. Scarpellini, A. Petrozza, M. Prato, and L. Manna, “Tuning the Optical Properties of Cesium Lead Halide Perovskite Nanocrystals by Anion Exchange Reactions.,” *J. Am. Chem. Soc.*, vol. 137, no. 32, pp. 10276–81, Aug. 2015.

[140] C. C. Lin, A. Meijerink, and R. S. Liu, “Critical Red Components for Next-Generation White LEDs,” *Journal of Physical Chemistry Letters*, vol. 7, no. 3. American Chemical Society, pp. 495–503, 04-Feb-2016.

[141] S. Tsunekawa, K. Ishikawa, Z. Q. Li, Y. Kawazoe, and A. Kasuya, “Origin of anomalous lattice expansion in oxide nanoparticles,” *Phys. Rev. Lett.*, vol. 85, no. 16, pp. 3440–3443, Oct. 2000.

[142] Y. Liu, M. Gibbs, C. L. Perkins, J. Tolentino, M. H. Zarghami, J. Bustamante, and M. Law, “Robust, Functional Nanocrystal Solids by Infilling with Atomic Layer Deposition,” *Nano Lett.*, vol. 11, no. 12, pp. 5349–5355, Dec. 2011.

[143] T. Leijtens, T. Giovenzana, S. N. Habisreutinger, J. S. Tinkham, N. K. Noel, B. A. Kamino, G. Sadoughi, A. Sellinger, and H. J. Snaith, “Hydrophobic Organic Hole Transporters for Improved Moisture Resistance in Metal Halide Perovskite Solar Cells,” *ACS Appl. Mater. Interfaces*, vol. 8, no. 9, pp. 5981–5989, Mar. 2016.

[144] M. V. Kovalenko, L. Manna, A. Cabot, Z. Hens, D. V. Talapin, C. R. Kagan, V. I. Klimov, A. L. Rogach, P. Reiss, D. J. Milliron, P. Guyot-Sionnnest, G. Konstantatos, W. J. Parak, T. Hyeon, B. A. Korgel, C. B. Murray, and W. Heiss, “Prospects of Nanoscience with Nanocrystals,” *ACS Nano*, vol. 9, no. 2, pp. 1012–1057, Feb. 2015.

[145] X. Lan, S. Masala, and E. H. Sargent, “Charge-extraction strategies for colloidal quantum dot photovoltaics,” *Nat. Mater.*, vol. 13, no. 3, pp. 233–240, Feb. 2014.

[146] Y. Shirasaki, G. J. Supran, M. G. Bawendi, and V. Bulović, “Emergence of colloidal quantum-dot light-emitting technologies,” *Nat. Photonics*, vol. 7, no. 1, pp. 13–23, Dec. 2012.

[147] A. Swarnkar, A. R. Marshall, E. M. Sanehira, B. D. Chernomordik, D. T. Moore, J. A. Christians, T. Chakrabarti, and J. M. Luther, "Quantum dot–induced phase stabilization of a-$CsPbI_3$ perovskite for high-efficiency photovoltaics," *Science*, vol. 354, no. 6308, pp. 92–95, 2016.

[148] Y. Yan, R. W. Crisp, J. Gu, B. D. Chernomordik, G. F. Pach, A. R. Marshall, J. A. Turner, and M. C. Beard, "Multiple exciton generation for photoelectrochemical hydrogen evolution reactions with quantum yields exceeding 100%," *Nat. Energy*, vol. 2, no. 5, p. 17052, Apr. 2017.

[149] S. Sharma, N. Weiden, and A. Weiss, "Phase Diagrams of Quasibinary Systems of the Type: ABX3—A′BX3; ABX3—AB′X3, and ABX3—ABX′3; X = Halogen," *Zeitschrift für Phys. Chemie*, vol. 175, no. 1, pp. 63–80, Jan. 1992.

[150] F. A. Stevie, *Secondary ion mass spectrometry: Applications for depth profiling and surface characterization*. Momentum Press, 2015.

[151] R. A. De Souza and M. Martin, "Probing Diffusion Kinetics with Secondary Ion Mass Spectrometry," *MRS Bull.*, vol. 34, no. 12, pp. 907–914, Dec. 2009.

[152] R. G. Wilson, F. A. Stevie, and C. W. Magee, *Secondary ion mass spectrometry: a practical handbook for depth profiling and bulk impurity analysis*. Wiley, 1989.

[153] M. R. Bergren, B. J. Simonds, B. Yan, G. Yue, R. Ahrenkiel, T. E. Furtak, R. T. Collins, P. C. Taylor, and M. C. Beard, "Electron transfer in hydrogenated nanocrystalline silicon observed by time-resolved terahertz spectroscopy," *Phys. Rev. B*, vol. 87, no. 8, p. 81301, Feb. 2013.

[154] R. L. Z. Hoye, P. Schulz, L. T. Schelhas, A. M. Holder, K. H. Stone, J. D. Perkins, D. Vigil-Fowler, S. Siol, D. O. Scanlon, A. Zakutayev, A. Walsh, I. C. Smith, B. C. Melot, R. C. Kurchin, Y. Wang, J. Shi, F. C. Marques, J. J. Berry, W. Tumas, S. Lany, V. Stevanović, M. F. Toney, and T. Buonassisi, "Perovskite-inspired photovoltaic materials: Toward best practices in materials characterization and calculations," *Chem. Mater.*, vol. 29, no. 5, pp. 1964–1988, Mar. 2017.

[155] J. A. Christians, J. S. Manser, and P. V. Kamat, "Best practices in perovskite solar cell efficiency measurements. Avoiding the error of making bad cells look good," *J. Phys. Chem. Lett.*, vol. 6, pp. 852–857, 2015.

[156] J. Tang, K. W. Kemp, S. Hoogland, K. S. Jeong, H. Liu, L. Levina, M. Furukawa, X.

Wang, R. Debnath, D. Cha, K. W. Chou, A. Fischer, A. Amassian, J. B. Asbury, and E. H. Sargent, “Colloidal-quantum-dot photovoltaics using atomic-ligand passivation.,” *Nat. Mater.*, vol. 10, no. 10, pp. 765–71, Oct. 2011.

[157] X. Lan, O. Voznyy, A. Kiani, F. P. Garc??a De Arquer, A. S. Abbas, G. H. Kim, M. Liu, Z. Yang, G. Walters, J. Xu, M. Yuan, Z. Ning, F. Fan, P. Kanjanaboos, I. Kramer, D. Zhitomirsky, P. Lee, A. Perelgut, S. Hoogland, and E. H. Sargent, “Passivation Using Molecular Halides Increases Quantum Dot Solar Cell Performance,” *Adv. Mater.*, vol. 28, no. 2, pp. 299–304, Jan. 2016.

[158] A. Stavrinadis, S. Pradhan, P. Papagiorgis, G. Itskos, and G. Konstantatos, “Suppressing Deep Traps in PbS Colloidal Quantum Dots via Facile Iodide Substitutional Doping for Solar Cells with Efficiency >10%,” *ACS Energy Lett.*, vol. 2, no. 4, pp. 739–744, Apr. 2017.

[159] NREL, “Research Cell Record Efficiency Chart.” .

[160] M. Yang, T. Zhang, P. Schulz, Z. Li, G. Li, D. H. Kim, N. Guo, J. J. Berry, K. Zhu, and Y. Zhao, “Facile fabrication of large-grain CH3NH3PbI3−xBrx films for high-efficiency solar cells via CH3NH3Br-selective Ostwald ripening,” *Nat. Commun.*, vol. 7, no. May, p. 12305, Aug. 2016.

[161] D. V. Talapin, “PbSe Nanocrystal Solids for n- and p-Channel Thin Film Field-Effect Transistors,” *Science*, vol. 310, no. 5745, pp. 86–89, Oct. 2005.

[162] J. Zhang, J. Tolentino, E. R. Smith, J. Zhang, M. C. Beard, A. J. Nozik, M. Law, and J. C. Johnson, “Carrier Transport in PbS and PbSe QD Films Measured by Photoluminescence Quenching,” *J. Phys. Chem. C*, vol. 118, no. 29, pp. 16228–16235, Jul. 2014.

[163] Y. Liu, M. Gibbs, J. Puthussery, S. Gaik, R. Ihly, H. W. Hillhouse, and M. Law, “Dependence of Carrier Mobility on Nanocrystal Size and Ligand Length in PbSe Nanocrystal Solids,” *Nano Lett.*, vol. 10, no. 5, pp. 1960–1969, May 2010.

[164] D. M. Balazs, D. N. Dirin, H.-H. Fang, L. Protesescu, G. H. ten Brink, B. J. Kooi, M. V. Kovalenko, and M. A. Loi, “Counterion-Mediated Ligand Exchange for PbS Colloidal Quantum Dot Superlattices,” *ACS Nano*, vol. 9, no. 12, pp. 11951–11959, Dec. 2015.

[165] L. M. Herz, “Charge-Carrier Mobilities in Metal Halide Perovskites: Fundamental Mechanisms and Limits,” *ACS Energy Lett.*, vol. 2, pp. 1539–1548, Jun. 2017.

[166] M. J. Smith, S. T. Malak, J. Jung, Y. J. Yoon, C. H. Lin, S. Kim, K. M. Lee, R. Ma, T. J.

White, T. J. Bunning, Z. Lin, and V. V. Tsukruk, “Robust, Uniform, and Highly Emissive Quantum Dot–Polymer Films and Patterns Using Thiol–Ene Chemistry,” *ACS Appl. Mater. Interfaces*, vol. 9, no. 20, pp. 17435–17448, May 2017.

VITA

Erin Sanehira was born in Honolulu, HI and is a proud graduate of Mililani High School in Mililani, HI. Growing up in a tropical climate where solar water heaters were prevalent, Erin was inspired to pursue research in solar energy. As an undergraduate at the University of Rochester, she was first introduced to photovoltaic research by Professor Philippe Fauchet who focused on plasmonic-enhanced thin film silicon solar cells. She also co-founded Solar Splash, an extracurricular club that competed in a collegiate solar-powered boat competition. After graduating from the University of Rochester with a B.S. in Electrical and Computer Engineering in 2011, Erin pursued a Ph.D. in Electrical Engineering at the University of Washington with a focus on nanoparticle-based photodetectors and photovoltaics under the direction of Professor Lih Lin and Professor Christine Luscombe. She was awarded the NASA Space Technology Research Fellowship, which afforded her the opportunity to conduct research in external, non-profit laboratories. She researched the stability of conventional thin film perovskite solar cells and explored novel quantum dot perovskite solar cells at the National Renewable Energy Laboratory under the direction of Dr. Joseph Luther, which served as the basis of her dissertation research. After receiving her Ph.D., Erin will be continuing to pursue her interest in solar energy as an engineer working to commercialize perovskite photovoltaic technology.